

AD _____

Award Number: DAMD17-01-1-0513

TITLE: Signal Detection Theory-Based Information Processing for
the Detection of Breast Cancer at Microwave Frequencies

PRINCIPAL INVESTIGATOR: Loren W. Nolte, Ph.D.

CONTRACTING ORGANIZATION: Duke University
Durham, North Carolina 27708-0077

REPORT DATE: August 2003

TYPE OF REPORT: Final

PREPARED FOR: U.S. Army Medical Research and Materiel Command
Fort Detrick, Maryland 21702-5012

DISTRIBUTION STATEMENT: Approved for Public Release;
Distribution Unlimited

The views, opinions and/or findings contained in this report are those of the author(s) and should not be construed as an official Department of the Army position, policy or decision unless so designated by other documentation.

20040112 131

REPORT DOCUMENTATION PAGEForm Approved
OMB No. 074-0188

Public reporting burden for this collection of information is estimated to average 1 hour per response, including the time for reviewing instructions, searching existing data sources, gathering and maintaining the data needed, and completing and reviewing this collection of information. Send comments regarding this burden estimate or any other aspect of this collection of information, including suggestions for reducing this burden to Washington Headquarters Services, Directorate for Information Operations and Reports, 1215 Jefferson Davis Highway, Suite 1204, Arlington, VA 22202-4302, and to the Office of Management and Budget, Paperwork Reduction Project (0704-0188), Washington, DC 20503

1. AGENCY USE ONLY (Leave blank)		2. REPORT DATE August 2003	3. REPORT TYPE AND DATES COVERED Final (1 Aug 2001 - 31 Jul 2003)
4. TITLE AND SUBTITLE Signal Detection Theory-Based Information Processing for the Detection of Breast Cancer at Microwave Frequencies			5. FUNDING NUMBERS DAMD17-01-1-0513
6. AUTHOR(S) Loren W. Nolte, Ph.D.			
7. PERFORMING ORGANIZATION NAME(S) AND ADDRESS(ES) Duke University Durham, North Carolina 27708-0077 E-Mail: lwn@ee.duke.edu			8. PERFORMING ORGANIZATION REPORT NUMBER
9. SPONSORING / MONITORING AGENCY NAME(S) AND ADDRESS(ES) U.S. Army Medical Research and Materiel Command Fort Detrick, Maryland 21702-5012			10. SPONSORING / MONITORING AGENCY REPORT NUMBER
11. SUPPLEMENTARY NOTES			
12a. DISTRIBUTION / AVAILABILITY STATEMENT Approved for Public Release; Distribution Unlimited			12b. DISTRIBUTION CODE
13. ABSTRACT (Maximum 200 Words) This research addressed directly the decision-theoretic task of detection and localization of breast tumor, using microwave diffraction measurements. Microwave energy has the advantages that at low power levels there are no radiation dangers, no contrast agents, and the examinations are comfortable. Although there is considerable scattering of a microwave signal in tissue, the presence, location, and nature of tumors is "coded" in the combination of amplitude and phases in the signals received at multiple sensors. Bayesian detection theory was used in this research to improve the probability of correct detection and localization. This improvement in performance is possible because conventional imaging techniques, by themselves, usually emphasize resolution and contrast, and leave the incorporation of uncertainties and decisions primarily to algorithms or human observers that post process the reconstructed image. This approach augments conventional medical image processing and provides additional processing of the scattered microwave field to aid the radiologist in dealing with uncertainties that are an inherent part of the decisions. Using the receiver operating characteristic (ROC) and other performance measures, and simulation, bounds on the performance attainable for various uncertainties in malignant tissue properties (permittivity), sizes, location, and signal-to-noise ratios were obtained.			
14. SUBJECT TERMS Breast cancer, signal detection, microwave imaging			15. NUMBER OF PAGES 49
			16. PRICE CODE
17. SECURITY CLASSIFICATION OF REPORT Unclassified	18. SECURITY CLASSIFICATION OF THIS PAGE Unclassified	19. SECURITY CLASSIFICATION OF ABSTRACT Unclassified	20. LIMITATION OF ABSTRACT Unlimited

Table of Contents

Cover.....	1
SF 298.....	2
Table of Contents.....	3
Introduction.....	4
Body.....	4
Key Research Accomplishments.....	5
Reportable Outcomes.....	6
Conclusions.....	6
References.....	7
Bibliography of Publications.....	8
List of Personnel Receiving Pay from Research Effort.....	8
Appendices.....	9

Introduction

Microwave energy has the advantages that at low power levels there are no radiation dangers, no contrast agents, and the examinations are comfortable. This research addresses directly the decision-theoretic task of detection and localization of breast tumor, using microwave diffraction measurements. Bayesian detection theory is used to improve the probability of correct detection and localization. This improvement in performance is possible because conventional imaging techniques, by themselves, usually emphasize resolution and contrast, and leave the incorporation of uncertainties and decisions primarily to algorithms or human observers that post process the reconstructed image. This approach augments conventional medical image processing and provides additional processing of the scattered microwave field to aid the radiologist in dealing with uncertainties that are an inherent part of the decisions.

Sha et al have compiled results from experiments in the literature that show that the microwave dielectric properties of malignant tissue are different from those of normal breast tissue. Signal detection theory, in its most fundamental form, provides a framework for incorporating this knowledge of breast tissue characteristics directly into the design of optimal task oriented information processing algorithms to aid in the detection of breast cancer. In addition, signal detection theory enables one to obtain upper limits of detection and localization performance as a function of uncertainties in the microwave properties of breast tissues, using quantitative measures such as the ROC (probability of detection vs. false alarm) and PCL (probability of correct localization). The proposed algorithm uses the direct microwave diffraction measurements and incorporates the fact that spatially adjacent tissues are similar in their permittivity values, but normal and malignant breast tissues have high contrast in the mean. These research results demonstrate the advantages of incorporating the microwave diffraction measurements directly into the computer-aided algorithm design.

Body

Detailed descriptions of the research done on this project during this reporting period are summarized below in References [1-4]. Copies of the conference papers and posters cited [1-4] are included in the appendix of this report.

Background -- Most of the past research in this field has focused on the study of the dielectric properties, the design of the microwave imaging prototypes, and the improvement of the EM forward and inverse algorithms. However, none of this research has incorporated signal detection theory directly into the microwave imaging at the measurement level. Markov Random Fields (MRF) and detection theory have been applied in mammography for diagnosis. However these only assumed a simple deterministic disk object model or did not utilize the *a priori* knowledge of the projections. This research presents Bayesian algorithms for Scattered Electromagnetic fields through an Uncertain Permittivity Image which incorporates the knowledge of the *a priori* permittivity image modeled by the MRF, the measurement noise, as well as the physical model of the forward scattered electric field. The Bayesian algorithms for the Uncertain Permittivity Image and the Threshold Image Processors are also presented for

comparisons. Our approach exploits the propagation of the scattered microwave fields to develop better diagnostic decision aids. Additional references to this background information are contained in Ref. 3

On this concept research award, Sha, the graduate student on this project, with the help of two other students, has compiled results from experiments in the literature that show that the microwave dielectric properties of malignant tissue is different from that of normal breast tissue [2]. Hence microwave imaging has the potential of providing a tool for improving the diagnosis of breast cancer with no known radiation dangers [2].

Although the experimental literature has provided promising evidence that the dielectric properties of malignant and benign tissue are different, this project investigated the impact of this on the ability to detect and localize tumors. Since tissue properties change spatially, statistical models were developed on this project that model simple uncertainties in the tissue permittivity within the framework of microwave imaging [3, 4]. The Markov Random Field was used to model the breast permittivity cross section as a propagating medium, and this was incorporated into the forward Electromagnetic (EM) propagation model [1], to predict the random field of the EM measurements at a received array of sensors. These statistical models of tissue permittivity were then incorporated into an optimal signal detection theory framework in which task-oriented goals such as detection and localization of a tumor drive the information processing [3, 4]. Using Bayesian signal detection theory, the likelihood ratio for tumor detection and the *a posteriori* probability of tumor location were computed and displayed. The ROC (receiver operating characteristics) was used as a quantitative performance measure. These results provide an upper bound on the task-driven goal, namely the detection of the presence or absence of a tumor as a function of tumor permittivity contrast, size, noise, and local spatial permittivity uncertainties that characterize the tissue in microwave imaging [3, 4]. In addition, the probability of correct localization (PCL) was obtained as a quantitative measure of how well one can determine the location of a tumor, as a function of tumor contrast, size, and spatial tissue properties [3,4].

Details of this research supported by this project are presented in the conference papers and poster sessions, references [1-3], with copies of drafts of these references [1-3] included in the appendix.

Key Research Accomplishments

- Experimental results were compiled from the literature. Those results show that the dielectric properties of malignant and normal breast tissue at microwave frequencies are different. This compilation was led by Liewei Sha, a graduate student on this project, and the results are published in Reference [2], Liewei Sha, Erika Ward, and Brandon Story, "A review of dielectric properties of normal and malignant breast tissue," Proceedings of the IEEE SoutheastCon 2002, pp. 457 -462, Columbia, South Carolina, April 5 - 7, 2002.

- Developed Markov Random field statistical models that characterize the uncertainties in the spatial properties of tissue permittivity at microwave frequencies. Incorporated this information into the forward Electromagnetic (EM) propagation to predict the random field of the EM measurements at a received array of sensors [3,4].
- Used an optimal signal detection theory framework in which task-oriented goals such as detection and localization of a tumor drive the information processing. Bayesian approaches were developed to compute the likelihood ratio for tumor detection and the *a posteriori* probability display of tumor location. [3,4]
- Although the permittivity between malignant and benign tissue has been reported in the experimental literature to be different, the question is how does this translate to ones ability to detect malignant tissue. Using the optimum signal detection and localization information processing algorithms derived above, ROC's were obtained to provide an upper bound on the detection of the presence or absence of a tumor. Results were obtained as a function of tumor permittivity contrast between malignant and normal tissue, size, noise, and local spatial permittivity uncertainties that characterize the tissue at microwave frequencies. [3,4]
- The probability of correct localization, PCL, was also obtained as a quantitative measure of how well one can determine the location of a tumor, as a function of tumor contrast, size, tissue spatial permittivity characteristics, and noise. [3,4]

Reportable Outcomes

Liewei Sha, Erika Ward , and Brandon Story , "A review of dielectric properties of normal and malignant breast tissue," Proceedings of the IEEE SoutheastCon 2002, pp. 457 -462, Columbia, South Carolina, April 5 - 7, 2002.

Liewei Sha, Loren W. Nolte, Zhong Qing Zhang and Qing H. Liu, "Performance analysis for Bayesian microwave imaging in decision aided breast tumor diagnosis," Proceedings of the 2002 IEEE International Symposium on Biomedical Imaging Washington D.C., pp. 1039-1042, Washington, DC, July7-10, 2002.

Liewei Sha, Loren W. Nolte, Zhong Qing Zhang and Qing Huo Liu, "Decision Aided Algorithms for Breast Tumor Diagnosis Using Microwave Diffraction Measurements," Poster, Era of Hope 2002 Department of Defense Breast Cancer Research Meeting, Orlando, Florida, September 25-28, 2002.

Conclusions

Decision-aided breast tumor diagnostic algorithms based on signal detection theory and microwave energy, which has no radiation danger at low power levels, have the potential of providing additional information for radiologist so as to improve the probability of

early detection of breast tumors as well as their correct locations. This Bayesian microwave imaging approach is driven by the ultimate decision tasks of whether or not a tumor is present, and if so where is it. It benefits from incorporating the *a priori* knowledge, although uncertain, of the permittivity properties of normal and malignant breast tissue. This approach also gains a decision performance advantage by processing the measurements directly using signal detection theory, rather than post processing a reconstructed image where some of the information needed for the decision has been lost.

References

1. Qing Huo Liu, Zhong Qing Zhang, Tonghui T. Wang, J. A. Bryan, Gary A. Ybarra, Loren W. Nolte, William T. Joines, "Active Microwave Imaging I – 2-D Forward and Inverse Scattering Methods," IEEE Transactions on Microwave Theory and Techniques, Vol. 50, No. 1, pp. 123-133, January 2002.
2. Liewei Sha, Erika Ward, and Brandon Story, "A review of dielectric properties of normal and malignant breast tissue," Proceedings of the IEEE SoutheastCon 2002, pp. 457 -462, Columbia, South Carolina, April 5 - 7, 2002.
3. Liewei Sha, Loren W. Nolte, Zhong Qing Zhang and Qing H. Liu, "Performance analysis for Bayesian microwave imaging in decision aided breast tumor diagnosis," Proceedings of the 2002 IEEE International Symposium on Biomedical Imaging Washington D.C., pp. 1039-1042, Washington, DC, July 7-10, 2002.
4. Liewei Sha, Loren W. Nolte, Zhong Qing Zhang and Qing Huo Liu, "Decision Aided Algorithms for Breast Tumor Diagnosis Using Microwave Diffraction Measurements," Poster, Era of Hope 2002 Department of Defense Breast Cancer Research Meeting, Orlando, Florida, September 25-28, 2002.

Bibliography of all publications

Qing Huo Liu, Zhong Qing Zhang, Tonghui T. Wang, J. A. Bryan, Gary A. Ybarra, Loren W. Nolte, William T. Joines, "Active Microwave Imaging I – 2-D Forward and Inverse Scattering Methods," IEEE Transactions on Microwave Theory and Techniques, Vol. 50, No. 1, pp. 123-133, January 2002.

Liewei Sha, Erika Ward , and Brandon Story , "A review of dielectric properties of normal and malignant breast tissue," Proceedings of the IEEE SoutheastCon 2002, pp. 457 -462, Columbia, South Carolina, April 5 - 7, 2002.

Liewei Sha, Loren W. Nolte, Zhong Qing Zhang and Qing H. Liu, "Performance analysis for Bayesian microwave imaging in decision aided breast tumor diagnosis," Proceedings of the 2002 IEEE International Symposium on Biomedical Imaging Washington D.C., pp. 1039-1042, Washington, DC, July7-10, 2002.

Liewei Sha and Loren W. Nolte, " Computer-aided algorithms for breast tumor diagnosis using microwave diffraction measurements", Poster Session, Era of Hope 2002 Department of Defense Breast Cancer Research Meeting, Orlando, Florida, September 25-28, 2002.

List of personnel receiving pay from research effort

Loren W. Nolte, PhD and PI, Duke University
Liewei Sha, PhD student, Duke University
Ying Song, M.S. student, Duke University

Appendices

Author and titles of copies of papers or posters resulting from this research that provide details for body of the report.

1. Copy of the paper by Qing Huo Liu, Ahong Qing Zhang, Tonghui T. Wang, J. A. Bryan, Gary A. Ybarra, Loren W. Nolte, William T. Joines, "Active Microwave Imaging I – 2-D Forward and Inverse Scattering Methods, " IEEE Transactions on Microwave Theory and Techniques, Vol. 50, No. 1, pp. 123-133, January 2002.
- 2.. Copy of the paper by Liewei Sha, Erika Ward , and Brandon Story , "A review of dielectric properties of normal and malignant breast tissue," Proceedings of the IEEE SoutheastCon 2002, pp. 457 -462, Columbia, South Carolina, April 5 - 7, 2002.
3. Copy of the paper by Liewei Sha, Loren W. Nolte, Zhong Qing Zhang and Qing H. Liu, "Performance analysis for Bayesian microwave imaging in decision aided breast tumor diagnosis," Proceedings of the 2002 IEEE International Symposium on Biomedical Imaging Washington D.C., pp. 1039-1042, Washington, DC, July7-10, 2002.
4. Copy of poster by Liewei Sha, Loren W. Nolte, Zhong Qing Zhang and Qing Huo Liu, "Decision Aided Algorithms for Breast Tumor Diagnosis Using Microwave Diffraction Measurements," Poster, Era of Hope 2002 Department of Defense Breast Cancer Research Meeting, Orlando, Florida, September 25-28, 2002.
5. Copy of paper by Liewei Sha, Loren W. Nolte, Zhong Qing Zhang, and Qing Huo Liu, "Incorporating statistical models of tissue permittivity into an optimal signal detection theory framework for the detection of breast cancer at microwave frequencies," submitted to the IEEE Transactions on Medical Imaging, December 2003.
6. Addendum to report

Active Microwave Imaging I—2-D Forward and Inverse Scattering Methods

Qing Huo Liu, *Senior Member, IEEE*, Zhong Qing Zhang, *Senior Member, IEEE*, Tonghui T. Wang, J. A. Bryan, Gary A. Ybarra, *Member, IEEE*, Loren W. Nolte, *Life Senior Member, IEEE*, and William T. Joines, *Life Senior Member, IEEE*

Abstract—Active microwave imaging (MWI) for the detection of breast tumors is an emerging technique to complement existing X-ray mammography. The potential advantages of MWI arise mainly from the high contrast of electrical properties between tumors and normal breast tissue. However, this high contrast also increases the difficulty of forming an accurate image because of increased multiple scattering. To address this issue, we develop fast forward methods based on the combination of the extended Born approximation, conjugate- and biconjugate-gradient methods, and the fast Fourier transform. We propose two nonlinear MWI algorithms to improve the resolution for the high-contrast media encountered in microwave breast-tumor detection. Numerical results show that our algorithms can accurately model and invert for the high-contrast media in breast tissue. The outcome of the inversion algorithms is a high-resolution digital image containing the physical properties of the tissue and potential tumors.

Index Terms—Biomedical applications, fast algorithms, imaging, inverse scattering, microwave techniques.

I. INTRODUCTION

EARLY treatment of breast cancer can be highly effective and can significantly increase long-term survival [1]. Among current clinical and experimental breast-cancer imaging technologies (see, e.g., [2]), the most popular method for breast cancer screening and diagnosis is based on X-ray mammography. In spite of its high resolution, however, X-ray mammography has the following shortcomings [3], [4].

- 1) It has difficulties detecting breast tumors at their earlier stages.
- 2) It has a decreased effectiveness in cases of women with dense breasts and has difficulties detecting tumors located near the chest wall or underarm.
- 3) It has a limited specificity between benign and malignant tissue resulting in high false-alarm rates at clinically accepted detection rates.
- 4) It uses ionizing radiation.
- 5) There is a discomfort to patients because of breast compression.

Manuscript received December 30, 2000; revised February 28, 2001. This work was supported in part by the U.S. Environmental Protection Agency under Grant CR-825-225-010, by the National Science Foundation under CAREER Grant ECS-9702195, and by the National Institutes of Health/National Institute of Cancer under Grant 5P01 CA42745-13.

The authors are with the Department of Electrical and Computer Engineering, Duke University, Durham, NC 27708-0291 USA (e-mail: qhliu@ee.duke.edu).
Publisher Item Identifier S 0018-9480(02)00020-0.

As an alternative and complementary modality for breast imaging, microwave (MW) techniques have been proposed over the last few years [5]–[8] because of its potentially high specificity for breast cancer diagnosis due to the high contrast in electrical properties between normal and malignant human breast tissues.

Due to significantly different sodium concentrations, fluid contents, and electrochemical properties, a significant contrast exists in electrical properties at MW frequencies between the normal and malignant human breast tissues [9]–[13]. For example, at 800 MHz, the relative permittivity (ϵ_r) and electrical conductivity (σ) for normal mammary tissues are around $\epsilon_r \approx 16$ and $\sigma \approx 0.16$ S/m, respectively, while they are $\epsilon_r \approx 57.2$ and $\sigma \approx 1.08$ S/m, respectively, for a malignant breast tumor. The contrast is 3.75 for the relative permittivity and 6.75 for the electrical conductivity. This high contrast gives rise to a large electromagnetic scattering signal when electromagnetic waves are applied to a malignant tumor embedded in a normal tissue.

Compared to X-ray mammography, MW mammography has the following potential advantages.

- 1) The high contrast in electrical properties can potentially provide a high specificity to distinguish between normal and malignant breast tissues. MW mammography may be able to detect, at an earlier stage, small tumors otherwise undetectable by X-ray mammography.
- 2) Microwave imaging (MWI) utilizes nonionizing radiation for breast cancer imaging. The MW radiation levels required are well within accepted safety standards, and there are no contrast agents involved.
- 3) The examinations using MWs are well tolerated since no breast compression is required for the patient. The MWI method provides a useful alternative and complement to the diagnostic information provided by X-ray mammography.

During the last decade, there has been significant progress in the development of experimental prototypes of two-dimensional (2-D) and three-dimensional (3-D) MWI systems based on various ideas [5]–[7], [14], [15]. These systems image 2-D (and more recently, 3-D) small- and medium-size objects, and sometimes even the full body [16]–[18]. Substantial research has also been carried out specifically for breast cancer diagnosis with narrow-band [14] and wide-band [5], [6] signals. A recent report, apparently the first clinical experiments, shows very promising results for MW breast imaging [7].

From the practical viewpoint, one of the most significant problems for current MWI systems is their lower spatial

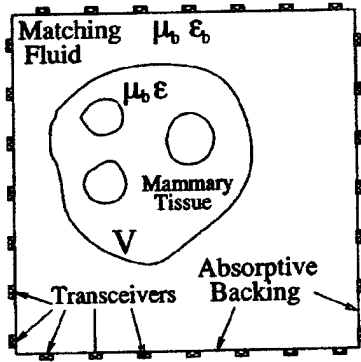


Fig. 1. Typical geometry for forward and inverse problems in MW breast imaging. Transmitting and receiving antennas are mounted on the rim of a fluid-holding box with an absorptive backing.

resolution. There has been great interest in inverse problems for biomedical applications of MWs to improve the resolution [19], [22], [23], [20], [21]. Unlike X-ray imaging techniques, which only need to consider the attenuation of the X-ray, for MWI technology, we need to consider multiple scattering (i.e., diffraction) of MWs within the tissues. This is a significant effect and cannot be neglected [18]. From this viewpoint, the very advantage of high contrast in electrical properties between normal and malignant tissues can also pose a major limitation if not treated correctly. This is because the high contrast introduces large multiple scattering effects, leading to a low resolution if linear or quasi-linear methods are used to invert for the object properties.

In this paper, we develop fast-forward and inverse-scattering algorithms to fully unravel multiple scattering effects. These algorithms are applied to form high-resolution images for an experimental prototype of a MW breast-imaging system recently developed at Duke University, Durham, NC. Our imaging technique uses the fast Fourier transform (FFT), the extended Born approximation (EBA), conjugate and biconjugate gradients, and contrast source-inversion (CSI) methods.

This paper is organized as follows. We briefly present the integral equation for the 2-D TM problem in Section II. The forward and inverse solution methods are presented in Sections III and IV. Numerical results are shown in Section V to demonstrate the efficacy of the technique. Conclusions are presented in Section VI.

II. INTEGRAL EQUATION

In this paper, we focus on 2-D MWI problems. We assume a TM_z wave from a finite source impinging on an inhomogeneous medium with a high contrast in both dielectric constant and conductivity with respect to a homogeneous background medium. In MW breast imaging, a matching material with a nonreflective backing is usually used to eliminate the reflections at the tissue/air interface, as illustrated in Fig. 1. In that case, the background medium is the matching fluid with properties similar to a normal breast tissue.

Fig. 1 illustrates the general scenario of the problem, where an inhomogeneous object with dielectric constant $\epsilon_r(\mathbf{r})$, conductivity $\sigma(\mathbf{r})$, and a constant magnetic permeability μ_b is im-

mersed in a background medium with the corresponding parameters ϵ_{rb} , σ_b , and μ_b . With an implied time dependence of $\exp(j\omega t)$, the complex permittivity for the object and background can be written as $\epsilon = \epsilon_0\epsilon_r - j\sigma/\omega$ and $\epsilon_b = \epsilon_0\epsilon_{rb} - j\sigma_b/\omega$. In the 2-D TM_z case, all field and source variables are only functions of $\mathbf{r} = (x, y)$. For an electric current source $\mathbf{J} = \hat{z}J_z(\mathbf{r})$ in such an inhomogeneous medium, the electric field $\mathbf{E} = \hat{z}E_z(\mathbf{r})$ satisfies the integral equation

$$E_z(\mathbf{r}) = E_z^{\text{inc}}(\mathbf{r}) + \int_D d\mathbf{r}' g(\mathbf{r}-\mathbf{r}') [k^2(\mathbf{r}') - k_b^2] E_z(\mathbf{r}') \quad (1)$$

where the complex wavenumbers k and k_b are defined by $k^2 = \omega^2\mu_b\epsilon$ and $k_b^2 = \omega^2\mu_b\epsilon_b$, respectively, and $g(\mathbf{r}-\mathbf{r}') = (1/4j)H_0^{(2)}(k_b|\mathbf{r}-\mathbf{r}'|)$ is the Green's function for a homogeneous background medium. The incident field E_z^{inc} in (1) is the field in the background medium, i.e., in the absence of the scatterer (or $k = k_b$).

Equation (1) is the central equation we use in this paper for both the forward and inverse solutions. In the forward problem, both the medium properties and the domain of inhomogeneity D are known; our aim is to solve (1) to obtain the electric field. In the inverse problem, the electromagnetic fields are measured at some discrete points, usually outside the domain of inhomogeneity; the medium properties (including the domain of inhomogeneity) are unknowns to be determined. However, we assume that the scatterer is finite and, thus, can always be enclosed in a large rectangular region D .

A. Historical Note

There is a large body of literatures dealing with both the forward and inverse solutions for integral equations similar to (1). It is not our purpose to present a thorough review of these works. Here, we will briefly summarize the developments leading to the methods used in this study.

In the context of low-frequency electromagnetic induction applications, the forward and inverse problems were solved with the EBA in [25]–[27]. An FFT accelerated EBA method was developed as fast-forward and inverse solvers in [28], and has been used as a preconditioner for the conjugate-gradient fast Fourier transform (CG-FFT) method in [29], [30], and [45]. However, the application in MWI involves significantly different physics than in our previous low-frequency problems where the wave fields are diffusive because of the dominant conduction current. The dominant wave phenomenon in the MWI application makes both the forward and inverse problems more challenging. The biconjugate-gradient fast Fourier transform (BCG-FFT) method used in this paper is an application of our recent method presented in [49].

III. FORWARD-SOLUTION METHODS

There are two purposes for the forward solution. First, it will be used to simulate and calibrate the imaging system. Secondly, it will be used to test the inverse algorithms by providing the simulated “measured” data. Furthermore, other inverse algorithms (unlike those in this paper) may require repeated forward solutions.

In the forward problem, the unknown electric field E_z appears both on the left-hand side and inside the integrand of (1). The conventional way of solving (1) is the method of moments (MOM), which discretizes the integral equation with N electric field unknowns in terms of basis functions inside D , and solves the resulting matrix equation by direct matrix inversion. Unfortunately, this direct method is prohibitively expensive, costing $O(N^3)$ CPU time and $O(N^2)$ computer memory.

A. EBA

An efficient way to solve (1) is to use the Born approximation [24], i.e., to assume that the electric field inside the integrand in (1) can be approximated by the incident field E_z^{inc} . The total field can then be easily calculated by performing the integral of the Green's function operating on the Born approximated current density.

The Born approximation has a very limited range of validity when the contrast and/or the size of the scatterer is small [25]–[27]. To increase the range of validity, one can use the EBA put forward in [25]. In essence, the EBA makes use of the fact that the Green's function $g(\mathbf{r} - \mathbf{r}')$ is highly peaked (in fact, singular) when $\mathbf{r} \rightarrow \mathbf{r}'$, and becomes relatively small for larger $|\mathbf{r} - \mathbf{r}'|$. Hence, one can replace $E_z(\mathbf{r}')$ inside the integrand in (1) with $E_z(\mathbf{r})$ and approximate (1) by

$$E_z^p(\mathbf{r}) \approx E_z^{\text{inc}}(\mathbf{r}) + E_z^p(\mathbf{r}) k_b^2 \int_D d\mathbf{r}' g(\mathbf{r} - \mathbf{r}') \chi(\mathbf{r}'), \quad \mathbf{r} \in D \quad (2)$$

where $\chi = (k^2/k_b^2 - 1)$ is the contrast function. Consequently, the electric field in the integrand of (1) can be more accurately approximated by the solution of (2) when this approximated field E_z^p from (2) is substituted into the integrand of (1) to yield

$$E_z^{(\text{EB})}(\mathbf{r}) = E_z^{\text{inc}}(\mathbf{r}) + k_b^2 \int_D d\mathbf{r}' g(\mathbf{r} - \mathbf{r}') \chi(\mathbf{r}') M^{-1}(\mathbf{r}') E_z^{\text{inc}}(\mathbf{r}') \quad (3)$$

where

$$M(\mathbf{r}) = 1 - k_b^2 \int_D d\mathbf{r}' g(\mathbf{r} - \mathbf{r}') \chi(\mathbf{r}'), \quad \mathbf{r} \in D. \quad (4)$$

It has been shown that the EBA has a significantly larger range of applicability than the Born approximation [25], [26], [28], [29], [30]. Furthermore, the computational cost for (3) remains essentially the same as the Born approximation, i.e., $O(M_f N)$ arithmetic operations, where M_f is the number of field points. However, (4) requires $O(N^2)$ arithmetic operations since $M(\mathbf{r})$ is needed for all N points within the object. Thus, the total cost of the EBA is $O(C_1 M_f N + C_2 N^2)$, where C_1 and C_2 are constants. This is still much more efficient than the direct MOM with $O(N^3)$ arithmetic operations.

B. Using FFT to Speed up the EBA: FFT-EBA Method

We adopt an efficient method for the electromagnetic induction problem [28]–[30] to speed up the EBA computation of the electric field at N points within the scatterer. This method is

based on the observation that the integrals in (3) and (4) are convolutional. Hence, by using the convolution theorem, one can solve for the electric field within the EBA approach as

$$\begin{aligned} E_z^{(\text{EB})}(\mathbf{r}) &= E_z^{\text{inc}}(\mathbf{r}) + k_b^2 \mathcal{F}^{-1} \left\{ \mathcal{F}[g(\mathbf{r})] \mathcal{F}[\chi(\mathbf{r}) M^{-1}(\mathbf{r}) E_z^{\text{inc}}(\mathbf{r})] \right\} \\ &\equiv \mathcal{L}_{\text{EB}}^{-1} [E_z^{\text{inc}}] \end{aligned} \quad (5)$$

where \mathcal{F} and \mathcal{F}^{-1} stand for the 2-D forward and inverse Fourier transforms, respectively, which, in their discrete forms with zero-padded arrays, can be achieved efficiently through the FFT algorithms with $O(N \log_2 N)$ arithmetic operations. Equation (5) also defines the operator \mathcal{L}_{EB} .

This improvement reduces the computational cost of the EBA from $O(N^2)$ to $O(N \log_2 N)$. Furthermore, it makes possible the following hybridization of the EBA with the CG-FFT and BCG-FFT methods without increasing the overall cost to $O(N^2)$. For the convenience of the following discussions, we refer to this improved approach as the FFT-EBA method.

C. EBA as a Preconditioner for CG-FFT and BCG-FFT Methods

Although the EBA is more accurate than the Born approximation, its error increases when the object becomes very large in size or in contrast against the background. An efficient full-wave method that, in principle, does not suffer from this limitation is the CG-FFT method [33]–[36]. This iterative method is more efficient than the MOM, as it requires only $O(K N \log_2 N)$ arithmetic operations, where K is the number of CG iterations. In our previous studies of the electromagnetic induction problem [29], [30], we propose to incorporate the EBA to further improve the efficiency of the CG-FFT or BCG-FFT methods [49].

Our aim here is to solve (1) for the unknown electric field E_z within the inhomogeneous region. Noting that the integral in (1) is a 2-D convolution between the Green's function $g(\mathbf{r})$ and induced current source $\chi(\mathbf{r}) E_z(\mathbf{r})$, we can invoke the convolution theorem to rewrite (1) in an operator form

$$\mathcal{L}[E_z] \equiv E_z - k_b^2 \mathcal{F}^{-1} \left\{ \mathcal{F}[g(\mathbf{r})] \mathcal{F}[\chi(\mathbf{r}) E_z] \right\} = E_z^{\text{inc}}. \quad (6)$$

This equation can then be solved iteratively by the CG-FFT method [33], [34], [36].

We apply the EBA as the preconditioner. Hence, instead of solving (6) directly, we solve an equivalent problem

$$\mathcal{L}_{\text{EB}}^{-1} \mathcal{L} E_z = E_z^{(\text{EB})} \quad (7)$$

where the preconditioner is the EBA operator defined in (5). Since the preconditioner $\mathcal{L}_{\text{EB}}^{-1}$ is achieved by the FFT algorithm in (5), this new (7) can again be solved efficiently by the CG-FFT method. With this preconditioning, this scheme converges much faster than the regular CG-FFT method [28], [29]. In reality, we found that even using the EBA preconditioner in only the first step of the conjugate-gradient (CG) method can significantly improve the convergence speed for typical electromagnetic problems. This partial preconditioning avoids the additional cost of the preconditioning in the majority of the

CG steps. The following numerical results are obtained by this preconditioning scheme.

Equation (7) can also be solved by using the biconjugate-gradient (BCG) method [31], [32], [49] with the FFT algorithm. The resulting EBA preconditioned BCG-FFT method is more efficient than the CG-FFT method described above. For procedures of the BCG iterations, see, for example, [31] and [49].

Note that there is no approximation in the above EBA preconditioned CG-FFT and BCG-FFT methods aside from the discretization procedure. The combination of the EBA and CG-FFT and BCG-FFT methods provides a seamless method, which is both efficient and accurate for low- and high-contrast scatterers. In practice, we define an acceptable error criterion e_{\min} based on the L_2 -norm residual error

$$e_2 = \frac{\|\mathcal{L}E_z - E^{\text{inc}}\|}{\|E^{\text{inc}}\|} \leq e_{\min}$$

to terminate the iteration process. For lower contrast problems, if the initial step of the EBA solution suffices, no further CG or BCG procedures are needed; for higher contrast problems, the CG or BCG iterations will continue until the residual error is smaller than e_{\min} . Note that e_2 can always be calculated even though the exact solution is not known. Compared with the regular CG-FFT and BCG-FFT methods, these EBA preconditioned methods are more efficient [29].

IV. NONLINEAR INVERSE-SCATTERING ALGORITHMS

In the inverse problem, the unknown material properties $\epsilon_r(\mathbf{r})$ and $\sigma(\mathbf{r})$ are inferred from the scattered electric field measured at some discrete locations. This inverse problem is nonlinear, as the material properties appear both in the contrast function χ and in E_z in (1). Furthermore, this inverse problem is ill posed because of the sparsity of measured data contaminated by noise [38].

Methods for solving the electromagnetic inverse-scattering problem include linear [37] and nonlinear [26], [28], [38], [40], [42], [43], [47], [48] inverse methods. (See [44] for more complete references.) In this study, we apply two methods for nonlinear inverse problems. The first is an improved two-step inversion method based on the EBA [25]–[28], [45]. This is a compromise between the linear and full nonlinear inversion methods. The second nonlinear method is based on the CSI method [46]–[48] with an improved initial solution through the two-step nonlinear inversion.

A. Two-Step Inverse Method Based on EBA

1) *FFT Enhanced Two-Step Inversion Method*: The EBA in (3) can be rewritten for the scattered field as

$$E_z^{\text{scat}}(\mathbf{r}_R, \mathbf{r}_T) = k_b^2 \int_D d\mathbf{r}' g(\mathbf{r}_R - \mathbf{r}') w(\mathbf{r}') E_z^{\text{inc}}(\mathbf{r}', \mathbf{r}_T) \quad (8)$$

where, for clarity, we have explicitly included the transmitter and receiver locations \mathbf{r}_T and \mathbf{r}_R in the electric field. In the above, $w(\mathbf{r})$ is defined as

$$w(\mathbf{r}) = \chi(\mathbf{r}) M^{-1}(\mathbf{r}) \quad (9)$$

where M is given in (4).

The two-step linear inverse method has been applied in [27] and enhanced by the FFT algorithm [28]. Here, we summarize

this FFT enhanced version adapted to the current problem in Cartesian coordinates [30] as follows.

Step 1) The induced source: The first step of this scheme is to invert for the induced source function $w(\mathbf{r})$ from (8). With the trapezoidal rule, (8) can be discretized into a linear system of equations

$$\mathbf{A} \cdot \mathbf{w} = \mathbf{d} \quad (10)$$

where \mathbf{A} is an $M \times N$ matrix, \mathbf{d} is the data vector containing the measured scattered field, N is the number of unknowns in domain D , and $M = M_R M_T$ is the number of measured data points determined by the number of source locations M_T and the number of receiver locations M_R . Note that this equation for the unknown \mathbf{w} is a classical linear ill-posed problem. A minimum-norm solution to (10) can be obtained by an optimization procedure. That is, we find a solution \mathbf{w} that will minimize the L_2 norm functional

$$I = \|\mathbf{d} - \mathbf{A} \cdot \mathbf{w}\|^2 + \gamma \|\mathbf{w}\|^2 \quad (11)$$

where γ is a regularization parameter. Minimizing I yields a linear equation as follows:

$$(\mathbf{A}^\dagger \cdot \mathbf{A} + \gamma \mathbf{I}) \mathbf{w} = \mathbf{A}^\dagger \cdot \mathbf{d}. \quad (12)$$

Equation (12) can be solved iteratively by the CG procedure with the cost of $O(MN)$ per iteration.

Step 2) The contrast function: Once $w(\mathbf{r})$ is obtained, our second linear inversion step is to invert for $\chi(\mathbf{r})$ (and, thus, $\epsilon_r(\mathbf{r})$ and $\sigma(\mathbf{r})$) using (9) and (4). That is to solve the following equation:

$$\chi(\mathbf{r}) + k_b^2 w(\mathbf{r}) \cdot \mathcal{F}^{-1} \left\{ \mathcal{F}[g] \mathcal{F}[\chi(\mathbf{r})] \right\} = w(\mathbf{r}). \quad (13)$$

Equation (13) is a linear equation for the unknown contrast function $\chi(\mathbf{r})$, a function representing the difference between the anomaly and background. Equation (13) is a well-posed linear problem. It can be solved iteratively by using the CG method to find unknown complex permittivity $\epsilon = \epsilon_0 \epsilon_r - j\sigma/\omega$. In the CG procedure, the Green's function operations are accelerated by the FFT algorithm. This represents an acceleration over the earlier versions of the two-step inversion scheme [26], [27], and reduces the number of arithmetic operations to $O(N \log_2 N)$ in each CG iteration [28], [30].

With these procedures, the original nonlinear inverse problem has been converted into two linear inverse problems based on the EBA. This scheme uses the FFT algorithm to accelerate the second linear inversion step to greatly reduce the computational cost from $O(N^3)$ to $O(N \log_2 N)$, where N is the number of unknown pixels in the inverse model. Next, we will improve the memory efficiency in the first linear inversion step.

2) *Improved Two-Step Inversion Scheme*: The above two-step inversion scheme is a significantly enhanced version of earlier work since the total CPU time is reduced to $O(C_1 K_1 M N + C_2 K_2 N \log_2 N)$, where C_1 and C_2 are constants, and K_1 and K_2 are the numbers of the CG iterations in the two steps, respectively [28]. However, the memory requirement is still large for the first step as \mathbf{A} requires $O(MN)$ storage. We can further improve the memory requirement in a way similar to the CSI method [47], [48]. Defining S and D as the domain of measured data and the imaged domain, respectively, and Green's operator G_S and G_D as

$$G_{S,D}[\cdot] = k_b^2 \int_D d\mathbf{r}' g(\mathbf{r} - \mathbf{r}') [\cdot], \quad \mathbf{r} \in S \text{ or } D \quad (14)$$

we can rewrite (8) as

$$E_z^{\text{scat}}(\mathbf{r}_R, \mathbf{r}_T) = \left\{ G_S \left[E_z^{\text{inc}}(\mathbf{r}', \mathbf{r}_T) w(\mathbf{r}') \right] \right\}(\mathbf{r}_R). \quad (15)$$

The first step of the EBA inversion for $w(\mathbf{r})$ can then be stated as the minimization of the functional

$$F = \|E_z^{\text{scat}} - G_S[E_z^{\text{inc}} w]\|_S^2 + \gamma \|w\|_D^2 \quad (16)$$

where S is the measured data domain. This functional is basically the same as that in (11), except that it is in an undiscretized form.

Since (16) is a quadratic functional of w , it can be minimized by the conjugate gradient procedure. Defining the data error

$$\rho_j = E_z^{\text{scat}} - G_S[E_z^{\text{inc}} w]$$

we can update w_n by the following CG procedure:

$$w_n = w_{n-1} + \alpha_n v_n \quad (17)$$

where the update directions $\{v_n\}$ are chosen by the Polak–Ribière CG directions

$$v_0 = 0 \quad (18)$$

$$v_n = d_n + \frac{\langle d_n, d_n - d_{n-1} \rangle_D}{\langle d_{n-1}, d_{n-1} \rangle_D} v_{n-1}, \quad n \geq 1. \quad (19)$$

The gradient (Frechet derivative) of the cost functional with respect to w is given by

$$d_n = -k_b^2 \sum_{j=1}^{M_T} \left[E_z^{\text{inc}}(\mathbf{r}, \mathbf{r}_{T,j}) \right]^* \int_S g^*(\mathbf{r} - \mathbf{r}') \rho_{j,n-1}(\mathbf{r}') d\mathbf{r}' + \gamma w_{n-1}, \quad \mathbf{r} \in D. \quad (20)$$

where the asterisk denotes the complex conjugate. By minimizing F in (16), the constant α_n is determined as

$$\alpha_n = - \frac{\langle d_n, v_n \rangle_D}{\|G_S[E_z^{\text{inc}} v_n]\|_S^2 + \gamma \|v_n\|_D^2}. \quad (21)$$

Note that an important difference between this procedure and that in the CSI (see [47]) is that w in (16), unlike the contrast source in CSI, is not a function of source location. Therefore,

the inversion is much faster than the CSI because the system of equations for w is much smaller.

Note that even though the CPU time for this modified first step remains $O(K_1 M N)$, the computer memory cost is reduced from $O(MN)$ to $O(M_T N)$, where $M = M_T M_R$ is the number of measured data. After w is obtained, we solve (13) to determine the complex permittivity profile with the computational complexity $O(N \log_2 N)$.

B. EBA Preconditioned CSI

For many problems, the two-step inversion scheme provides satisfactory results. However, since the EBA is an approximate method, the inverse procedure based on the EBA to reconstruct the complex permittivity profile may not always be adequate, especially for very high contrasts. Under those circumstances, some nonlinear inversion methods can be employed to achieve better results. The recently developed CSI method has an important feature in that it does not require a forward solution in the inverse iterations [47], [48]. We adopt this CSI method for MW breast imaging by defining an object functional

$$F = \eta_S \sum_j \|E_z^{\text{scat}} - G_S[w_j]\|_S^2 + \eta_D \sum_j \|\chi E_z^{\text{inc}} - w_j + \chi G_D[w_j]\|_D^2 \quad (22)$$

where $w_j = \chi(\mathbf{r}) E_z(\mathbf{r}, \mathbf{r}_{T,j})$ for $\mathbf{r} \in D$ is the contrast source, and the normalization constants η_S and η_D are chosen so that both terms in (22) are equal to one if $w_j = 0$. The procedures to minimize F in (22) for the solution of χ can be found in [48]. It is worth noting that even though (22) is similar to (16), the minimization of (22) is more time consuming since, here, w_j is a function of the source location.

Given the measured scattered electric field, we can invert for the permittivity profile by the CSI method. However, in contrast to the earlier CSI implementations, we use the above two-step inversion result rather than the back-propagation as the initial solution to speed up the convergence. Preliminary results show that this improved CSI procedure accelerates the convergence of the inversion as the two-step EBA inversion already achieves a reasonable approximation. For our typical examples, the EBA preconditioned CSI method requires less than half of the iterations and CPU time of the original CSI method.

V. NUMERICAL RESULTS AND DISCUSSIONS

Our numerical models will aim to simulate a prototype MWI system for breast cancer imaging developed at Duke University. Fig. 1 schematically shows the basic geometry modeled in this study. The rectangular cylinder is filled with a matching fluid whose electrical properties are close to those of the normal breast tissue. The outer rim of the cylinder is an absorptive material to attenuate outgoing waves. This configuration is aimed to eliminate reflections from the tissue/ambience interface and the cylinder/air interface in order to enhance the image resolution. An array of transmitting and receiving MW antennas are mounted on the outer surface of the cylinder. The operating frequency for the following examples is 800 MHz (except as oth-

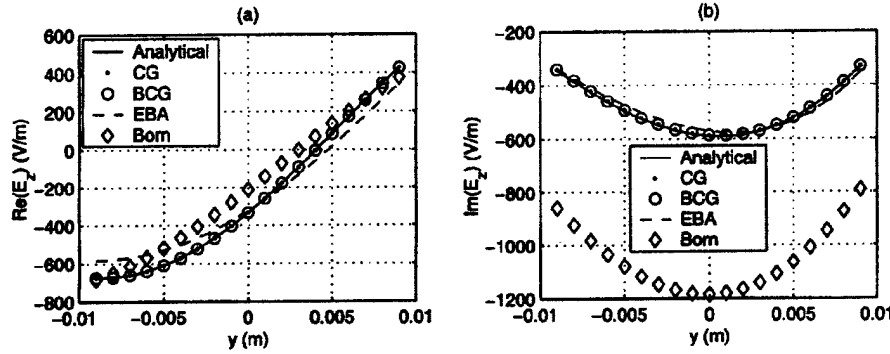


Fig. 2. Comparison of the EBA, Born, CG-FFT, and BCG-FFT methods and analytical solution for a circular cylinder ($\epsilon_r = 64$, $\sigma = 0.64$ S/m) with the center at the origin. The line source is at $(0, 0.03)$ m, while the receivers are at $(0, y)$ m, $y \in (-0.01, 0.01)$ m.

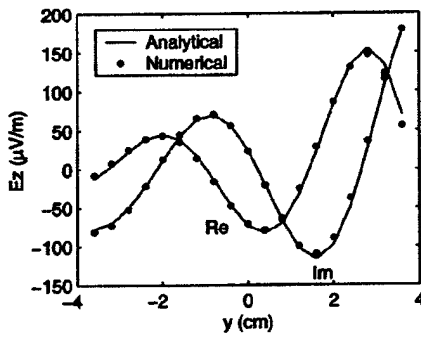


Fig. 3. Lossy cylinder with $\epsilon_r = 57.2$, $\sigma = 1.08$ S/m, and diameter 0.08 m. The line source is at $(0, 0.08)$ m, while the receivers are at $(0, y)$ m, $y \in (-0.04, 0.04)$.

erwise indicated), although both the apparatus and numerical models are designed for wide-band signals.

A. Forward-Modeling Results

In our 2-D forward model, we simulate an electric current source $\mathbf{J} = \hat{z}J_z(x, y)$ in an inhomogeneous conductive medium with dielectric constant $\epsilon_r(x, y)$, conductivity $\sigma(x, y)$, and constant permeability μ_0 . The background medium is homogeneous and has the properties $\epsilon_{rb} = 16$, $\sigma_b = 0.16$ S/m, and $\mu_b = \mu_0$ to simulate the normal tissue and the matching fluid inside the cylinder.

We first study the accuracy of the EBA method against the Born approximation, CG-FFT, BCG-FFT, and analytical solution for a circular tumor with $\epsilon_r = 64$, $\sigma = 0.64$ S/m and a diameter of 0.01 m. The line source is 0.03 m away from the cylinder center. Fig. 2 shows that the EBA result has a much greater accuracy than the Born approximation for this high contrast medium. Both CG-FFT and BCG-FFT results have the same accuracy, and take four and three iterations to reach a relative residual error of 0.01% with the EBA preconditioner. The CPU time for the Born approximation, EBA, CG-FFT, and BCG-FFT methods are 1.2, 1.2, 3.5, and 2.2 s, respectively, on a SUN Ultra 60 Workstation.

For larger contrasts and higher frequencies, as expected, the accuracy of the EBA will decrease, and full-wave CG- and BCG-FFT methods have to be used. In the second example,

we simulate a large-contrast circular cylinder with $\epsilon_r = 57.2$, $\sigma = 1.08$ S/m, and a diameter of 0.08 m. The line source is 0.12 m away from the center of the cylinder. We compute the electric field inside the cylinder by the CG-FFT and analytical solution. Fig. 3 is the comparison of the numerical result and analytical solution. We observe that both real and imaginary parts of the numerical result agree well with the analytical solution.

Fig. 4 compares the CG-FFT and BCG-FFT results for a tissue with multiple tumors. The results again show excellent agreement between these two methods. The BCG-FFT method converges in only two iterations, while the CG-FFT method converges in eight iterations to a residual error of 0.01%. The CPU time for this case is 4.5 s, and 2.2 s for the CG-FFT and BCG-FFT methods, respectively.

B. Inverse-Scattering Results

For the image formation, we have developed the two-step inverse method that is based on the EBA and CSI method. The EBA inversion aims to produce a fast, albeit quantitatively less accurate, image while the CSI method aims to produce an excellent accuracy at the expense of more computational cost. The two-step inversion result is used as the preconditioner for the CSI result. In the following examples, the measured data is obtained by the CG-FFT method with a much finer grid than that used in the inversion. Neither the EBA, nor the CSI method requires a forward solution during the inversion iterations, thus, the so-called "inverse crime" is not committed here. The background is the normal tissue with properties given for Fig. 2. We use 60 transmitters and 60 receivers uniformly distributed on the four edges of a square of size 16×16 cm², giving a total of 3600 measured data points. The region to be inverted is divided into 29×29 unknown pixels with a cell size 0.0052×0.0052 m².

In the first example, there are two anomalous objects within the homogeneous medium. The first anomaly has a dielectric constant of $\epsilon_r = 40$ and conductivity $\sigma = 1.08$ S/m. The other object has $\epsilon_r = 57.2$, $\sigma = 1.08$ S/m. These two anomalies simulate two tumors; the first one perhaps in the process of becoming malignant, while the second one is malignant. There is a significant difference in the electrical properties of these two tumors. The reconstructed results are shown in Fig. 5. Both the permittivity and conductivity anomalies are well resolved. In

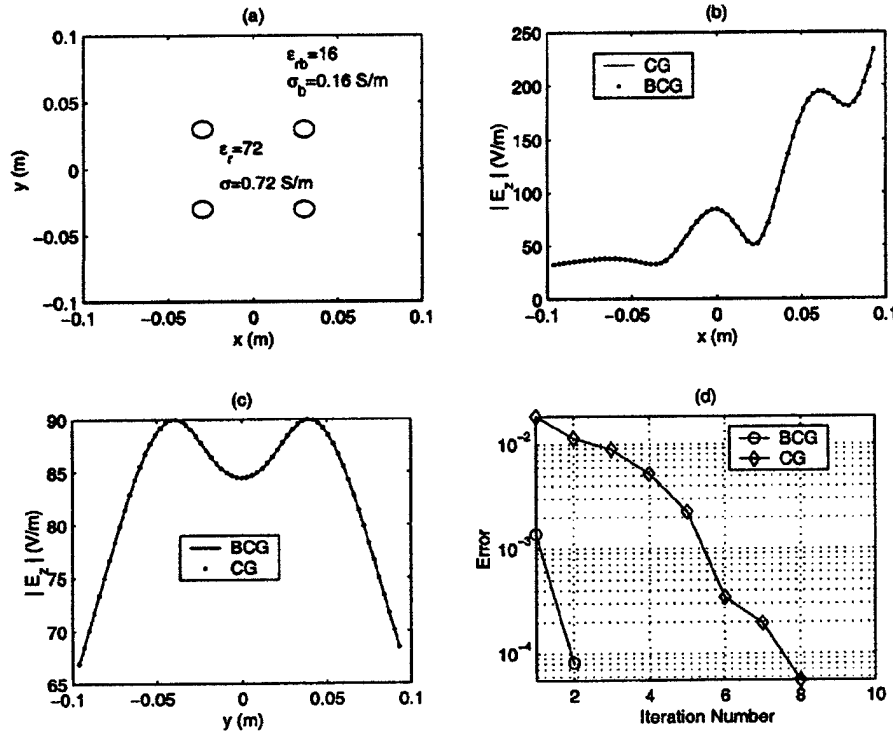


Fig. 4. CG-FFT and BCG-FFT results for a tissue with multiple tumors. The line source is located at $(0, -0.189)$. (a) Geometry of four tumors ($\epsilon_r = 72$, $\sigma = 0.72$ S/m) in a background medium ($\epsilon_b = 16$, $\sigma_b = 0.16$ S/m). (b) Magnitude of electric field along $(x, 0)$, $x \in (-0.1, 0.1)$ and (c) along $(0, y)$, $y \in (-0.1, 0.1)$. (d) Convergence curves for the CG-FFT and BCG-FFT methods.

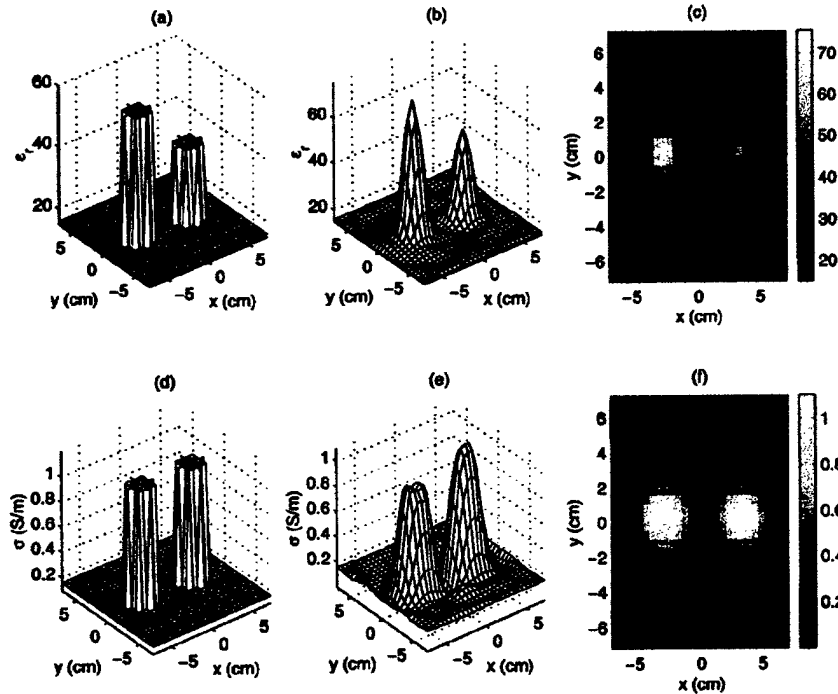


Fig. 5. Simultaneous inversion of dielectric constant and conductivity profiles at 800 MHz. The ground truth of: (a) ϵ_r and (d) σ profiles. Inverted dielectric: (b), (c) constant and (e), (f) conductivity.

this case, the preconditioned CSI method takes 70 iterations, and 8 min and 7 s CPU time to converge to a relative residual error of 0.97%.

We then demonstrate the super resolution [38], [39] of the nonlinear inverse-scattering CSI algorithm. The same measurement geometry as in Fig. 5 is used. We use an EBA preconditioning

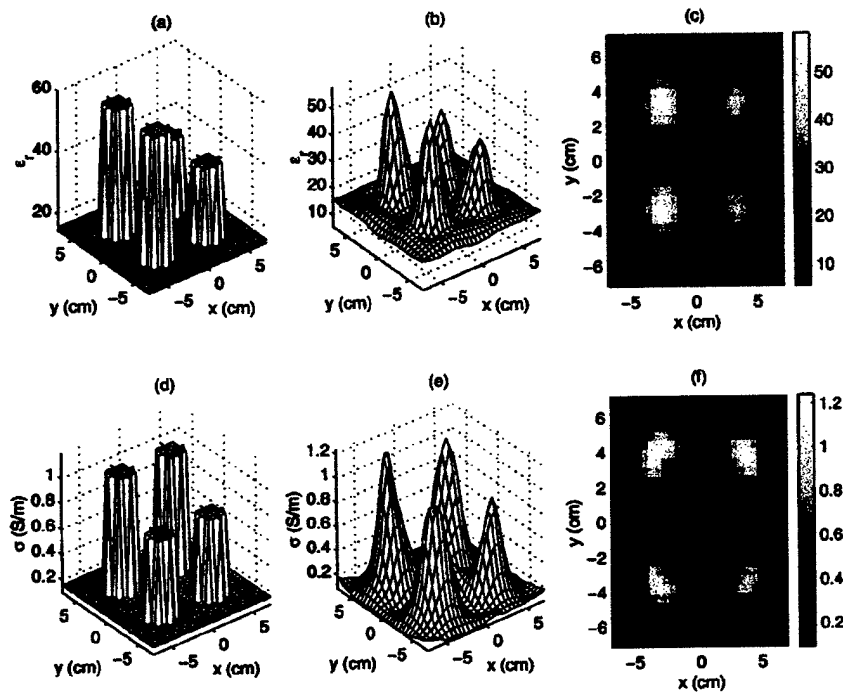


Fig. 6. Super resolution of dielectric constant and conductivity anomalies separated by only 0.22 wavelengths at 800 MHz. The ground truth of: (a) ϵ_r and (d) σ profiles. The inverted dielectric: (b), (c) constant and (e), (f) conductivity. The measured data E_{scat}^{meas} has a 10% Gaussian noise (SNR = 20 dB).

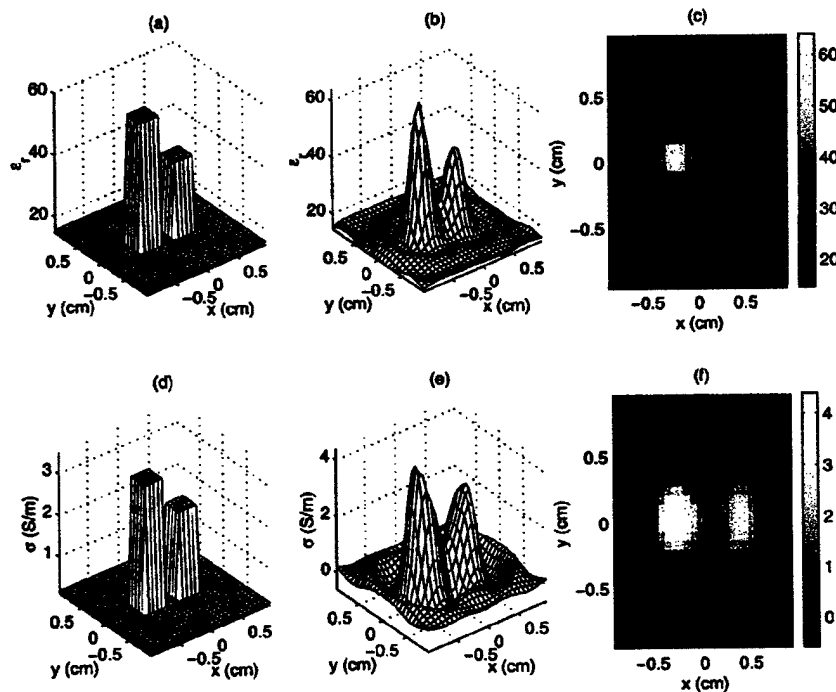


Fig. 7. Inversion of dielectric constant and conductivity anomalies separated by only 0.22 wavelengths at 6 GHz with properties as in Fig. 5. The ground truth of: (a) ϵ_r and (d) σ profiles. The inverted dielectric: (b), (c) constant and (e), (f) conductivity.

tioned CG-FFT to simulate the electric field outside the inversion area. Within the region being inverted, there are four anomalies separated only by 0.22 wavelengths (2.06 cm) at 800 MHz. We add 10% Gaussian noise to the scattered field data (i.e., signal-to-noise ratio SNR = 20 dB). Fig. 6 shows the ground

truth and reconstructed profiles. This example clearly demonstrates that the so-called super resolution [38] can be achieved for the high-contrast medium in MW breast imaging. This super resolution is possible because the nonlinear multiple scattering has been fully accounted for and because of the near-field mea-

surement. For more in-depth discussions on this topic, the reader is referred to [38] and [39].

Finally, we study the potential resolution at a higher frequency of 6 GHz. In this case, we invert for two very small anomalies only 0.28 cm apart and complex permittivity the same as in Fig. 5. The image area is about $2 \times 2 \text{ cm}^2$ with 29×29 pixels, giving a comparable computational cost as Figs. 5 and 6. RMS noise of 10% for the scattered field data has been added. Fig. 7 shows that our inverse algorithm can resolve these small objects when operated at a high frequency.

C. Discussions

This study represents a new application of some of our recent fast algorithms developed for low-frequency electromagnetic subsurface sensing problems [28]–[30], [35], [41], [45], [49]. However, for low-frequency induction problems, the conduction current is dominant and only the conductivity profile can be inverted. For MWI, both dielectric constant and conductivity profiles must be inverted simultaneously. This represents a much more difficult problem, and an increasingly important application in biomedical imaging.

The above numerical results show the efficacy of our 2-D forward- and inverse-scattering methods. In spite of this, there are many outstanding issues that require further research. Firstly, it would have been ideal if there is experimental verification. However, at present, we are unable to present this verification because our experimental setup has 3-D waveguide aperture transmitting antennas, which cannot be adequately modeled by our 2-D methods. Secondly, 3-D effects in breast tumor detection are expected to be very strong. Therefore, we are currently pursuing a better experimental verification in the following two directions: we are modifying our experimental setup so that it can be better modeled by our 2-D models with some 3-D compensation techniques, and we are developing full 3-D forward- and inverse-scattering methods to include all 3-D effects in MWI measurements. Thirdly, the breast tissue is not homogeneous because of the presence of fat, glandular tissue, etc. This inhomogeneity will definitely degrade the images. These important issues will be addressed in our future research.

VI. CONCLUSIONS

We have applied fast-forward and inverse methods to simulate 2-D MWI for breast tumor detection. The forward methods are based on the EBA, FFT, and CG and BCG methods. The FFT algorithm is used to expedite the EBA calculation, while the EBA is used to precondition the CG-FFT and BCG-FFT methods. The combination of these basic ingredients results in algorithms with a complexity of $O(N \log_2 N)$. The inverse methods are based on a two-step nonlinear inversion and the CSI methods, which do not require forward solutions during the iterations of the inverse solution. Numerical results demonstrate the efficiency of the forward and inverse methods, and the high resolution of the image-formation algorithm for the breast-imaging applications. Future work includes experimental validation and 3-D algorithms.

REFERENCES

- [1] J. R. Harris, M. E. Lippman, U. Veronesi, and W. Willett, "Medical progress: Breast cancer," *New Eng. J. Med.*, vol. 327, no. 5, pp. 319–328, 1992.
- [2] M. Douek, T. Davidson, and I. Taylor, "Breast cancer imaging—What are the optimal modalities?," *Eur. J. Surg. Oncol.*, vol. 24, no. 6, pp. 573–582, 1998.
- [3] F. M. Hall, J. M. Storella, D. Z. Silverstone, and G. Wyshak, "Non-palpable breast-lesions: Recommendation for biopsy based on suspicion of carcinoma at mammography," *Radiology*, vol. 167, no. 2, pp. 353–358, 1988.
- [4] C. Boetes, R. D. M. Mus, R. Holland, J. O. Barents, S. P. Strijk, T. Wobbes, J. H. C. Hendriks, and S. H. J. Ruys, "Breast tumors: Comparative accuracy of MR imaging relative to mammography and US for demonstrating extent," *Radiology*, vol. 197, no. 3, pp. 743–747, 1995.
- [5] S. C. Hagness, A. Taflov, and J. E. Bridges, "Two-dimensional FDTD analysis of a pulsed microwave confocal system for breast cancer detection: Fixed-focus and antenna-array sensors," *IEEE Trans. Biomed. Eng.*, vol. 45, pp. 1470–1479, Dec. 1998.
- [6] —, "Three-dimensional FDTD analysis of a pulsed microwave confocal system for breast cancer detection: Design of an antenna-array element," *IEEE Trans. Antennas Propagat.*, vol. 47, pp. 783–791, May 1999.
- [7] P. M. Meaney, M. W. Fanning, D. Li, P. Poplack, and K. D. Paulsen, "A clinical prototype for active microwave imaging of the breast," *IEEE Trans. Microwave Theory Tech.*, vol. 48, pp. 1841–1853, Nov. 2000.
- [8] E. C. Fear and M. A. Stuchly, "Microwave detection of breast cancer," *IEEE Trans. Microwave Theory Tech.*, vol. 48, pp. 1854–1863, Nov. 2000.
- [9] R. Pethig, "Dielectric properties of biological materials," *IEEE Trans. Elect. Insulation*, vol. EI-19, pp. 17–20, Jan. 1984.
- [10] S. S. Chaudhary, R. K. Mishra, A. Swarup, and J. M. Thomas, "Dielectric properties of normal and malignant human breast tissues at radio-wave and microwave frequencies," *Indian J. Biochem. Biophys.*, vol. 21, pp. 76–79, 1984.
- [11] W. T. Joines, "Frequency dependent absorption of electromagnetic energy in biological tissue," *IEEE Trans. Biomed. Eng.*, vol. BME-31, pp. 215–222, MONTH 1984.
- [12] W. T. Joines, Y. Zhang, C. Li, and R. L. Jirtle, "The measured electrical properties of normal and malignant human tissues from 50 to 900 MHz," *Med. Phys. J.*, vol. 21, no. 4, pp. 547–550, 1994.
- [13] A. M. Campbell and D. V. Land, "Dielectric properties of female human breast tissue measured at 3.2 GHz," *Phys. Med. Biol.*, vol. 37, no. 1, pp. 193–210, 1992.
- [14] P. M. Meaney, K. D. Paulsen, A. Hartov, and R. K. Crane, "An active microwave imaging system for reconstruction of 2-D electrical property distributions," *IEEE Trans. Biomed. Eng.*, vol. 42, pp. 1017–1025, Oct. 1995.
- [15] L. Jofre, M. S. Hawley, A. Broquetas, E. d. l. Reyes, M. Ferrando, and A. R. Elias-Fuste, "Medical imaging with a microwave tomographic scanner," *IEEE Trans. Biomed. Eng.*, vol. 37, pp. 303–312, Mar. 1990.
- [16] S. Caorsi, A. Frattoni, G. L. Gragnani, E. Nortino, and M. Pastorino, "Numerical algorithm for dielectric-permittivity microwave imaging of inhomogeneous biological bodies," *Med. Biol. Eng. Comput.*, vol. 29, no. 6, pp. 37–44, 1991.
- [17] S. Caorsi, G. L. Gragnani, and M. Pastorino, "An electromagnetic imaging approach using a multi-illumination technique," *IEEE Trans. Biomed. Eng.*, vol. 41, pp. 406–409, Apr. 1994.
- [18] S. Y. Semenov, R. H. Svenson, and A. E. Boulyshev *et al.*, "Three-dimensional microwave tomography: Experimental prototype of the system and vector Born reconstruction method," *IEEE Trans. Biomed. Eng.*, vol. 46, pp. 937–946, Aug. 1999.
- [19] K. Belkebir, R. E. Kleinman, and C. Pichot, "Microwave imaging-location and shape reconstruction from multifrequency scattering data," *IEEE Trans. Microwave Theory Tech.*, vol. 45, pp. 469–476, Apr. 1997.
- [20] O. M. Bucci and T. Isernia, "Electromagnetic inverse scattering: Retrieval information and measurement strategies," *Radio Sci.*, vol. 32, no. 6, pp. 2123–2137, 1997.
- [21] S. Caorsi and G. L. Gragnani, "Inverse scattering method for dielectric objects based on the reconstruction of the nonmeasurable equivalent current density," *Radio Sci.*, vol. 34, no. 1, pp. 1–8, 1999.
- [22] M. Pastorino, "Short-range microwave inverse scattering techniques for image reconstruction and applications," *IEEE Trans. Instrum. Meas.*, vol. 47, pp. 1419–1427, Dec. 1998.
- [23] S. Y. Semenov, A. E. Boulyshev, and A. E. Souvorov *et al.*, "Three-dimensional microwave tomography: Experimental imaging of phantoms and biological objects," *IEEE Trans. Microwave Theory Tech.*, vol. 48, pp. 1071–1074, June 2000.

- [24] M. Born and E. Wolf, *Principles of Optics*. New York: Pergamon, 1980.
- [25] T. M. Habashy, R. W. Groom, and B. R. Spies, "Beyond the Born and Rytov Approximations. A Nonlinear Approach to Electromagnetic Scattering," *J. Geophys. Res.*, vol. 98, pp. 1759–1775, 1993.
- [26] C. Torres-Verdin and T. M. Habashy, "Rapid 2.5-D forward modeling and inversion via a new nonlinear scattering approximation," *Radio Sci.*, vol. 29, pp. 1051–1079, 1994.
- [27] —, "A two-step linear inversion of two-dimensional electrical conductivity," *IEEE Trans. Antennas Propagat.*, vol. 43, pp. 405–415, Apr. 1995.
- [28] Z. Q. Zhang and Q. H. Liu, "Reconstruction of axisymmetric media with an FFHT enhanced extended Born approximation," *Inverse Problems*, vol. 16, no. 5, pp. 1281–1296, 2000.
- [29] —, "The hybrid extended Born approximation and CG-FFHT method for axisymmetric media," in *IEEE AP-S Int. Symp. Dig.*, vol. 2, 2000, pp. 602–605.
- [30] —, "Two nonlinear inverse methods for electromagnetic induction measurements," *IEEE Trans. Geosci. Remote Sensing*, vol. 39, pp. 1331–1339, June 2001.
- [31] C. F. Smith, A. F. Peterson, and R. Mittra, "The biconjugate gradient method for electromagnetic scattering," *IEEE Trans. Antennas Propagat.*, vol. 38, pp. 938–940, June 1990.
- [32] H. Gan and W. C. Chew, "A discrete BCG-FFT algorithm for solving 3D inhomogeneous scatterer problems," *J. Electromag. Waves Applicat.*, vol. 9, pp. 1339–1357, 1995.
- [33] D. T. Borup and O. P. Gandhi, "Fast-Fourier-transform method for calculation of SAR distributions in finely discretized inhomogeneous models of biological bodies," *IEEE Trans. Microwave Theory Tech.*, vol. MTT-32, pp. 355–360, Apr. 1984.
- [34] A. P. M. Zwamborn and P. M. v. d. Berg, "A weak form of the conjugate gradient FFT method for two-dimensional TE scattering problems," *IEEE Trans. Antennas Propagat.*, vol. 39, pp. 953–960, June 1991.
- [35] Q. H. Liu and W. C. Chew, "Applications of the CG-FFHT method with an improved FHT algorithm," *Radio Sci.*, vol. 29, no. 4, pp. 1009–1022, 1994.
- [36] M. F. Catedra, R. P. Torres, J. Basterrechea, and E. Gago, *The CG-FFT Method: Application of Signal Processing Techniques to Electromagnetics*. Norwell, MA: Artech House, 1995.
- [37] A. J. Devaney, "A filtered backpropagation algorithm for diffraction tomography," *Ultrason. Imaging*, vol. 4, pp. 336–350, 1982.
- [38] W. C. Chew and Y. M. Wang, "Reconstruction of the two-dimensional permittivity using the distorted Born iterative method," *IEEE Trans. Med. Imag.*, vol. 9, pp. 218–255, June 1990.
- [39] F.-C. Chen, F. C. Chen, and W. C. Chew, "Experimental verification of super-resolution in nonlinear inverse scattering," *Appl. Phys. Lett.*, vol. 72, pp. 3080–3082, 1998.
- [40] N. Joachimowicz, C. Pichot, and J. Hugonin, "Inverse scattering: An iterative numerical method for electromagnetic imaging," *IEEE Trans. Antennas Propagat.*, vol. 39, pp. 1742–1752, Dec. 1991.
- [41] W. C. Chew and Q. H. Liu, "Inversion of induction tool measurements using the distorted Born iterative method and CG-FFHT," *IEEE Trans. Geosci. Remote Sensing*, vol. 32, pp. 878–884, July 1994.
- [42] Q. H. Liu, "Reconstruction of two-dimensional axisymmetric inhomogeneous media," *IEEE Trans. Geosci. Remote Sensing*, vol. 31, pp. 587–594, May 1993.
- [43] —, "Nonlinear inversion of electrode-type resistivity measurements," *IEEE Trans. Geosci. Remote Sensing*, vol. 32, pp. 499–507, May 1994.
- [44] T. A. Maniatis, K. S. Nikita, and N. K. Uzunoglu, "Two-dimensional dielectric profile reconstruction based on spectral-domain moment method and nonlinear optimization," *IEEE Trans. Microwave Theory Tech.*, vol. 48, pp. 1831–1840, Nov. 2000.
- [45] Q. H. Liu, Z. Q. Zhang, and X. M. Xu, "The hybrid extended Born approximation and CG-FFT method for electromagnetic induction problems," *IEEE Trans. Geosci. Remote Sensing*, vol. 39, pp. 347–355, Mar. 2001.
- [46] P. M. v. d. Berg and R. E. Kleinman, "A total variation enhanced modified gradient algorithm for profile reconstruction," *Inverse Problems*, vol. 11, pp. L5–L10, 1995.
- [47] —, "A contrast source inversion method," *Inverse Problems*, vol. 13, pp. 1607–1620, 1997.
- [48] —, "Extended contrast source inversion," *Inverse Problems*, vol. 15, pp. 1325–1344, 1999.
- [49] Z. Q. Zhang and Q. H. Liu, "Three-dimensional weak-form conjugate and biconjugate-gradient FFT methods for volume integral equations," *Microwave Opt. Technol. Lett.*, vol. 29, pp. 350–356, June 2001.

Qing Huo Liu (S'88–M'89–SM'94) received the Ph.D. degree in electrical engineering from the University of Illinois at Urbana-Champaign, in 1989.

From September 1986 to December 1988, he was a Research Assistant with the Electromagnetics Laboratory, University of Illinois at Urbana-Champaign, and from January 1989 to February 1990, he was a Post-Doctoral Research Associate. From 1990 to 1995, he was a Research Scientist and Program Leader with Schlumberger-Doll Research, Ridgefield, CT. From 1996 to May 1999, he was with New Mexico State University. Since June 1999, he has been an Associate Professor of Electrical Engineering, Duke University, Durham, NC. He has authored or co-authored over 170 papers in refereed journals and conference proceedings. His research interests include computational electromagnetics and acoustics, biomedical imaging, geophysical subsurface sensing, and inverse problems.

Dr. Liu is a member of Phi Kappa Phi, Tau Beta Pi, and the Society of Exploration Geophysicists (SEG). He is a full member of the U.S. National Committee of URSI Commissions B and F. He currently serves as an associate editor for the IEEE TRANSACTIONS ON GEOSCIENCE AND REMOTE SENSING, for which he also served as a guest editor for the Special Issue on Computational Methods. He was the recipient of the 1996 Presidential Early Career Award for Scientists and Engineers (PECASE) presented by the National Science and Technology Council, the 1996 Early Career Research Award presented by the Environmental Protection Agency, and the 1997 CAREER Award presented by the National Science Foundation.



Zhong Qing Zhang (M'01–SM'01) was born in Henan, China, on October 3, 1966. He received the B.S., M.S., and the Ph.D. degrees from the University of Petroleum, Shandong, China, in 1988, 1991, and 1997, respectively, all in geophysics.

From April 1991 to August 1994, he was a Research Engineer with the Zhongyuan Well Logging Company, Puyang, China. From July 1997 to December 1998, he was with the University of Petroleum, Dongying, China, where he taught advanced graduate electromagnetics and performed research. From January 1999 to May 1999, he was a Post-Doctoral Research Associate at the New Mexico State University. Since June 1999, he has been with the Department of Electrical and Computer Engineering, Duke University, Durham, NC, first as a Post-Doctoral Research Associate and then as a Research Scientist. His current research interests are in fast algorithms for electromagnetic modeling, inverse problems, borehole geophysics, cross-well problems, simulation of integrated circuits, and MWI for biomedical applications.

Tonghui T. Wang received the B.Sc. degree in mathematics from University of Northwestern, Xi'an, China, in 1982, and the M.Sc. degree and Ph.D. degrees in statistics from the University of Windsor, Windsor, ON, Canada, in 1988 and 1992, respectively.

He is currently an Associate Professor in the Department of Electrical and Computer Engineering, New Mexico State University, Las Cruces.

J. A. Bryan, photograph and biography not available at time of publication.

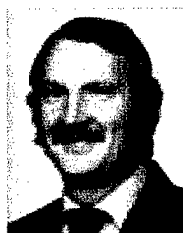
Gary A. Ybarra (S'86–M'86) was born in Hampton, VA, on May 13, 1960. He received the B.S., M.S., and Ph.D. degrees from North Carolina State University, Raleigh, in 1983, 1986, and 1992 respectively, all in electrical and computer engineering.

He is currently an Associate Professor of the Practice and Director of Undergraduate Studies in the Department of Electrical and Computer Engineering, Duke University, Durham, NC. His research interests include radar signal processing and MWI.

Loren W. Nolte (S'56-M'57-IM'99-LSM'01) was born in Napoleon, OH. He received the B.S.E.E. degree from Northwestern University, Evanston, IL, and the M.S.E. and Ph.D. degrees in electrical engineering from The University of Michigan at Ann Arbor, respectively.

Following a year of post-doctoral research in signal detection theory at The University of Michigan at Ann Arbor, he joined the faculty at Duke University, Durham, NC, in 1966, as an Assistant Professor of electrical engineering and became a Professor of electrical and biomedical engineering in 1972. He has held Visiting Professorships at the University of Colorado, Boulder, Colorado State University, Fort Collins, the University of Washington, Seattle, and the Scripps Institution of Oceanography, La Jolla, CA. He is currently Chairman of the Department of Electrical and Computer Engineering, Duke University. His research interests have included optimal Bayesian approaches to adaptive detection, classification, tracking and localization of underwater signals, including recurrent transients under various noise conditions, as well as signal and environmental uncertainties. He was also an early contributor to optimal (likelihood-ratio-based) decision fusion. His recent contributions include the development of physics-based array signal processing algorithms, which incorporate the physics, as well as the uncertainty of ocean acoustic environmental parameters. His current research interests also include the application of signal-detection theory to medical imaging in cancer research in collaboration with the Duke University Medical Center.

Dr. Nolte has served as an associate editor of underwater acoustics for the IEEE TRANSACTIONS ON ACOUSTICS, SPEECH, AND SIGNAL PROCESSING, and has served on its Technical Committee on Underwater Acoustics.



William T. Joines (M'61-SM'94-LSM'97) was born in Granite Falls, NC. He received the B.S.E.E. degree (with high honors) from North Carolina State University, Raleigh, in 1959, and the M.S. and Ph.D. degrees in electrical engineering from Duke University, Durham, NC, in 1961 and 1964, respectively.

From 1959 to 1966, he was a Member of the Technical Staff at Bell Telephone Laboratories, Winston-Salem, NC, where he was engaged in research and development on MW components and systems for military applications. In 1966, he joined the faculty of Duke University, where he is currently a Professor of electrical and computer engineering. His research and teaching interests are in the area of electromagnetic-wave interactions with structures and materials, mainly at MW and optical frequencies. He has authored or co-authored over 100 technical papers on electromagnetic-wave theory and applications and holds seven U.S. patents.

Dr. Joines was the recipient of the Scientific and Technical Achievement Award presented by the Environmental Protection Agency in 1982, 1985, and 1990.

A Review of Dielectric Properties of Normal and Malignant Breast Tissue

Liewei Sha, Duke University, Durham, NC
Erika Renee Ward, Duke University, Durham,
Brandon Stroy, Duke University, Durham, NC

Keywords: dielectric properties, breast tissue, normal, malignant

ABSTRACT

This paper presents a review of the dielectric properties of normal and malignant breast tissues for radio through microwave frequencies, as well as a brief summary of the experiment methods and the mechanisms that explain the difference in the dielectric properties of normal and malignant breast tissue. This information provides a basis for the development of diagnostic techniques for breast cancer and also highlights the areas that are in need of more experiments.

1. INTRODUCTION

The contrast in the dielectric properties between normal and malignant tissues is a basis for diagnostic applications using microwave devices. The study of normal tissues has been widely reviewed. This paper, in addition, collects together dielectric property data on benign and malignant breast tissues from a number of researchers, and presents them in graphical form so that this information is convenient for general reference. It should be emphasized that the data shown has been interpolated, extrapolated or computed from the graphs and tables, so it is not necessarily precise. This paper also reviews the mechanisms behind the differences in dielectric properties of normal and malignant breast tissues.

Most data are represented in terms of conductivity σ and relative permittivity ϵ' , since σ and ϵ' of biological materials are practically independent of frequency up to the microwave range [1]. For the two low frequency cases with no σ and ϵ' available, the data are represented in terms of a parallel combination of a conductance G and a capacitance C . The two pairs of terms are equivalent in that,

$$Y^* = G + j\omega C = (A/d)(\sigma + j\omega\epsilon\epsilon') \quad (1)$$

Where, Y^* is the complex admittance of the equivalent circuit of an idealized parallel plate capacitor filled with the tissue of σ and ϵ' . A/d is the geometry factor. We assume (ϵ', σ) follow a bi-variate normal distribution. Therefore, the modeling of the data can be represented by the specific cross section of the distribution function, which satisfies,

$$((x-m_x)^2/\sigma_x^2 + (y-m_y)^2/\sigma_y^2 - 2\rho(x-m_x)(y-m_y)/\sigma_x\sigma_y)/(1-\rho^2) = 1 \quad (2)$$

where, x is the relative permittivity, y is the conductivity, and m_x , m_y and σ_x , σ_y are the marginal mean and variance. ρ is the correlation coefficient of ϵ' and σ . If only the mean and variance values are available but not the original data pairs, we

assume an independent distribution of (ϵ', σ) and $\rho=0$.

All data are from human breast tissue, except for one case from rats. The category of breast tissues in the literature is ambiguous. In this paper, we define the following major categories of breast tissue.

- fat
- normal, includes glands tissue (lobules that produce milk), and connective tissue (fibrous tissue that surrounds the lobules and ducts)
- benign, includes fibroadenoma and mastitis
- malignant, i.e. breast carcinomas

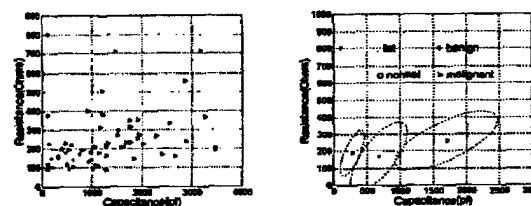
We first display the data in the low and high frequency regions, in the order of their publication date. Then we discuss the consistency and inconsistency in the data as well as the diagnostic value of the dielectric properties from the data. Finally the mechanisms are reviewed.

2. REVIEW OF EXPERIMENT DATA

2.1. List of data at low frequency

1. Fricke et.al. ([2], 1926, 20kHz, 24°C), measured the parallel capacitance and resistance ($R=1/G$) of excised samples from 55 patients, using a wheatstone bridge. Several types of tissue were studied: fat, gland, mastitis, fibroadenoma and carcinoma. Data is displayed in Fig.1. Only one sample of fat is measured, no variance is available for this type.

Figure 1: Capacitor versus Resistor



Left: original data; right: modeling of the data

2. Morimoto et.al. ([3,4], 1990, 10kHz, 37°C) obtained in vivo measurements of breast cancer, fibroadenoma, normal breast tissue and fatty tissue using a three-electrode method. The proposed equivalent circuit is composed of R_p parallel with the series of R_i and C_m . We transformed it to parallel R and C , using $R=R_iR_p/(R_i+R_p)$, $C=C_m$. With no original data and correlation coefficient available, Fig.2 displays the modeling of the data, assuming $\rho=0$.

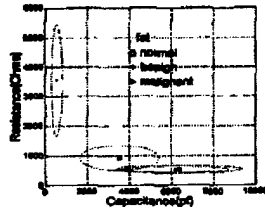


Figure 2: Capacitor versus Resistor

3. Jossinet et al. ([5,6], 1996, 488Hz-1MHz, 21°C) measured 120 samples from 64 patients, using impedance probe sensors connected with a microcomputer system. In Fig.3, data of six types of tissue is displayed, gland (o), connective (*), fat (*), mastopathy (square), fibroadenoma (+), carcinoma (V). We calculated the relative permittivity and conductivity from the original complex impedance data ρ^* (not the characteristic impedance) using,

$$\epsilon' = \text{Im}(1/\rho^*)/(\omega\epsilon_0), \sigma = \text{Re}(1/\rho^*), \rho^* = 1/(\sigma + j\omega\epsilon_0\epsilon') \quad (3)$$

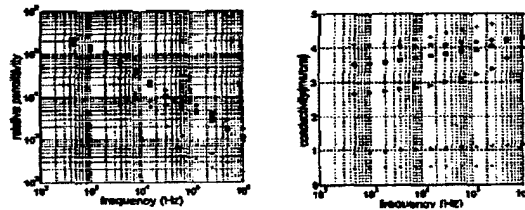


Figure 3 Permittivity and conductivity versus frequency

2.2. List of data at high frequency

4. T.S. England et al. ([7,8], 1949-50, 3-24GHz, 37°C) measured the attenuation α nepers/cm, and phase constant β radians/cm of the standing wave pattern of the excised human breast fat and carcinoma tissue samples in the wave-guide. We computed the relative permittivity ϵ' and conductivity σ using [23, Eqn4.28],

$$\epsilon' = (\alpha^2 - \beta^2)/\omega^2\mu_0\epsilon_0, \sigma = 2\alpha\beta/\omega\mu_0 \quad (4)$$

The variance due to these measurements were computed and presented with the light marker in Fig. 4. Our extrapolations are shown with dashed lines.

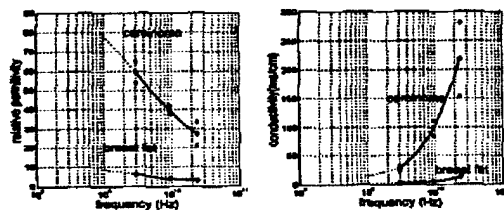


Figure 4 permittivity and conductivity versus frequency

5. W.T. Joines et al. ([9,10,11], 1980, 30MHz-2GHz, 37°C), obtained in vivo measurements of SMT-2A tumor and mammary gland tissue samples from 22 rats. The nondestructive method uses an open-ended coaxial probe to produce a fringing field in the termination tissue and a

directional coupler and an oscilloscope to detect the fringing pattern. The dielectric properties are then computed. The data is shown in Fig. 5, in which skin effect is not corrected, and the data can not be compared with in vitro data directly.

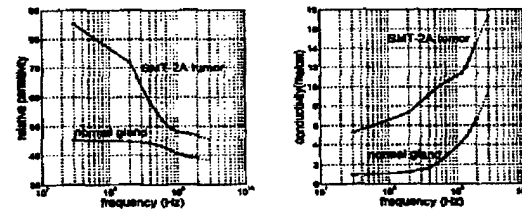


Figure 5: Permittivity and conductivity versus frequency [9]

6. S.S. Chaudhary et al. ([12], 1984, 3MHz-3GHz, 24°C), measured excised normal and malignant breast tissues from 15 patients, using the time domain spectroscopy system of HP. We use the total spread over the mean value (0.8%) to compute the variance of the data, which is shown in Fig. 6.

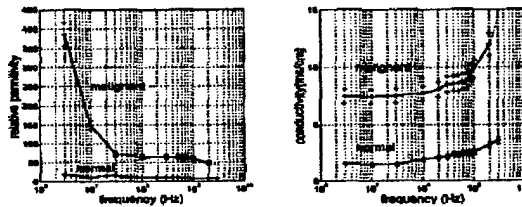


Figure 6: Permittivity and conductivity versus frequency [12]

7. A.J. Surowiec et al. ([13], 1988, 0.02MHz-100MHz, 37°C) measured the input reflection coefficient of 28 samples from 7 patients, using a coaxial line sensor connected to an HP3577 network analyzer. Tissue types include ductal carcinoma, lobular carcinoma, and surrounding tissues. The measured dielectric values are available only at 100kHz and 100MHz, and we use square symbols to represent the mean and meanstd values of those data in Fig. 7. The authors provided the parameters $\epsilon_\infty, \epsilon_s, \tau, \sigma$, and α , by fitting the data with the Cole-Cole equations [1],

$$\epsilon^* = \epsilon_\infty + (\epsilon_s - \epsilon_\infty)/(1 + (j\omega\tau)^{1-\alpha}) - j\sigma/\omega\epsilon_0 \quad (5)$$

where $\tau = 1/2\pi\tau$, τ is the relaxation time, f_c is the relaxation frequency, α is the distribution parameter that reflects the range of τ . s represents the low frequencies $f \ll f_c$, ω represents the high frequencies $f \gg f_c$. When $\alpha = 0$, Eqn.5 is the same as Debye equation.

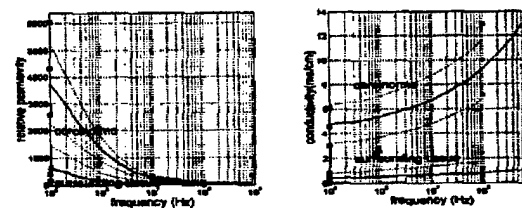


Figure 7 Permittivity and conductivity versus frequency

The curves in Fig. 7 are computed from the fitted Cole-Cole model in [13]. The dark lines are the mean values, the light

lines are the mean \pm std values. Extrapolations are shown in light color. Comparing the mean from the measurements and the model, the conductivity values agree well, but the relative permittivity values show some inconsistency.

8. A.M. Campbell et al. ([14], 1992, 3.2GHz, 24°C) measured 39 samples of normal breast fat, 18 samples of benign tumors, 22 samples of glandular connective tissue and 20 samples of cancer from 37 patients, using a resonant cavity perturbation method. Dielectric properties were measured using the observation of the changes in resonant frequency. In Fig. 8, the left plot displays the original data. The right plot illustrates the modeling of the data with Eqn.2.

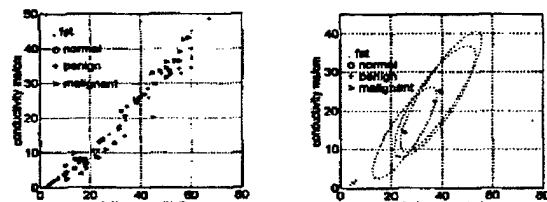


Figure 8 conductivity versus permittivity
Left: original data; Right: modeling of the data

9. W.T. Joines et al. ([15], 1994, 50MHz-900MHz, 24°C), measured admittance of 12 normal mammary samples and 12 malignant mammary samples from 12 patients, using a flat-ended coaxial probe connected to a network analyzer HP 8754A. ϵ' and σ are then computed from the admittance with the knowledge of the geometry factor. In Fig. 9, the mean values are presented with the solid lines, the standard error on the mean is presented with the dashed lines. Extrapolations are represented with light lines.

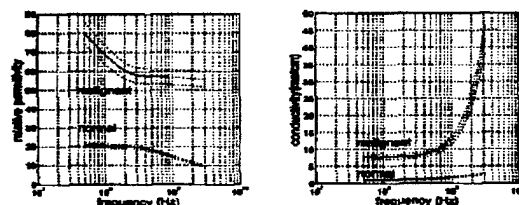


Figure 9 Permittivity and conductivity versus frequencies [15]

10. P.M. Meaney et al. ([16], 2000 900MHz, 37°C) obtained the in vivo breast microwave imaging of 5 patients, all non-malignant, at 900MHz.

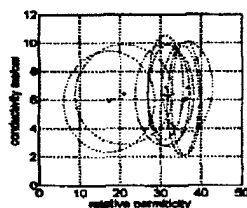


Figure 10 conductivity versus permittivity

We display the modeling of the data of individuals in Fig. 10 to represent the heterogeneity within and across patients. The correlation coefficient is not available and assumed to be 0.

2.3. Data consistency and inconsistency

Low frequencies. At low frequency ranges, the dielectric values of the four types of tissue are all available for the first three cases, as shown in Figures 1, 2 and 3. We cannot compare them directly, because of the unknown geometry factors in cases 1 and 2. Yet we can still make comparisons according to the relative distribution of the data for the same tissue types. The consistencies noted are listed below,

- The conductivity of the malignant tissue falls between the fat (plus connective tissue) and the normal gland tissue (plus the benign fibroadenoma and mastitis tissues).
- The benign and normal tissues can be grouped together relative to the malignant tissues on the ϵ' - σ plane.
- The relative position of the fat tissue on the ϵ' - σ plane compared to the other types is the same.

This information of data consistency provides a basis for identifying breast cancer, benign tumor and normal breast tissue using the tissue conductivity at 1kHz-1MHz.

The inconsistency in the first three cases is that the malignant tissue has lower capacitance (or permittivity) than that of the normal and benign tissues in case 2 and the lower frequency region of case 3, but it has the largest capacitance values in cases 1 and the higher frequency region of case 3. One of the possible reasons for the inconsistency is the frequency difference. It is 10kHz in case 2, 20kHz in case 1 and 488Hz-1MHz in case 3. Therefore, the inconsistency can be related with a turning frequency point in tens of kHz, above which the capacitance value of cancerous tissues became larger than that of normal and benign tissues. Other reasons for the inconsistency are the intrinsic heterogeneity and the temperature difference of tissue samples.

This information of inconsistency suggests that in the range 1kHz to 1MHz, the capacitance of breast tissues is not a good quantity to diagnose breast cancer. More experiments and analyses on the capacitance properties of normal and malignant breast tissues are needed in this frequency range.

High frequencies. In the high frequency range, we can compare the dielectric data directly.

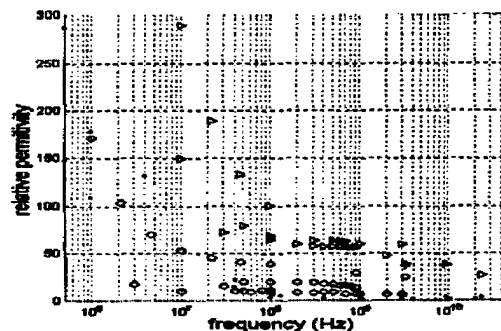


Figure 11 Permittivity versus frequency

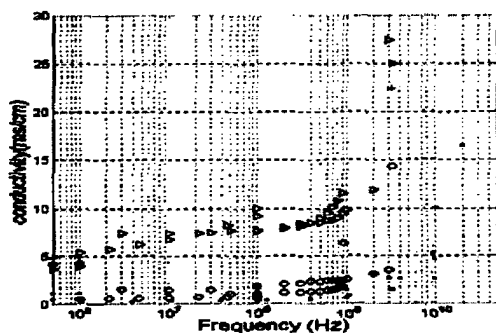


Figure 12 Conductivity versus frequency

Fig. 11 and 12 illustrate the dielectric data together in the range 500KHz to 20GHz. One more case of breast fat [21] is included. Four types of breast tissue: fat (•), normal (○), benign (+), malignant (▽) are displayed.

For a clearer view, Fig. 13 and 14 illustrate the modeling of the data for multiple cases on the ϵ'' - σ plane at 900MHz and 3.2GHz. Again, four types of breast tissue: fat (•), normal (○), benign (+), malignant (▽) are displayed.

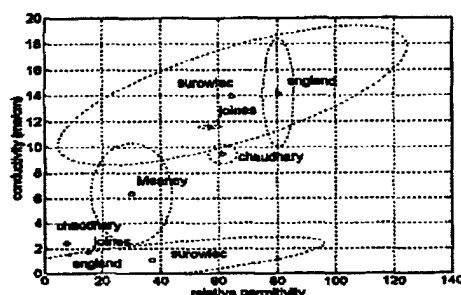


Figure 13 Conductivity versus Permittivity, at 900MHz

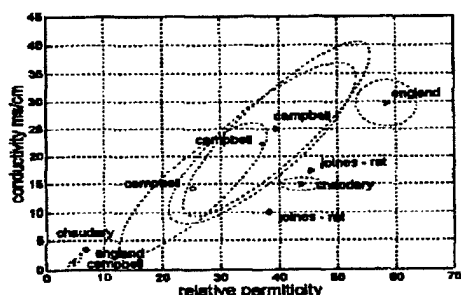


Figure 14 Conductivity versus Permittivity, at 3.2GHz

From Fig. 11-14, we observe the data inconsistency,

- The mean dielectric values of normal and malignant breast tissues have obvious variability.
- The mean conductivity values of normal breast tissues in Joines' rat data, Campbell's data, and Meaney's data are more than twice that of other normal breast tissue cases at the corresponding frequencies. The mean permittivity

values of normal breast tissue in Joines' rat data and Campbell's data are more than twice that in England's data and Chaudhary's data at 3.2GHz frequency.

The possible two reasons for the inconsistency are listed below, which may help explain the results and improve the future experiment designs.

• Experiment method

1. Limitations in experiments. Chaudhary's samples were collected in physiological saline, which will affect the accuracy of the data. Campbell's malignant samples are frozen and defrosted before the measurement, which may affect the accuracy of the data of this type.
2. In vivo vs in vitro. Joines' rat data is from in vivo measurements with uncorrected skin effects. Meaney's data comes from reconstruction of in vivo microwave imaging. Others are from excised samples. In vivo methods seem to have higher dielectric values.
3. Sample temperature differences. Lower sample temperature will make the dielectric value a little bit lower, when the frequency is below 2GHz.

• Intrinsic heterogeneity

1. Normal breast tissues are composed of breast fat, connective tissue and gland tissue, etc. In the literature, the composition of normal breast tissues from case to case may differ.
2. Different stages of tumor development will change the tumor's dielectric property and introduce variability [2,13]. Some samples of malignant tissues were actually composed of small parts of malignant cells infiltrating within a large part of normal cells, which may decrease the mean value of the malignant tissue samples.
3. Across patients. The breast tissue samples from patients with different water content or fat content and in different stage of menstruation, pregnancy or lactation will have obvious differences in dielectric values. Campbell's data came from a relatively larger patient group, which may introduce wider variability.

This inconsistency information indicates the importance of using proper sample storage method before experiments and suggests a standardization of the experiment conditions like the sample and environment temperatures, as well as the record of patients' information for later analysis.

Although there are so many conditions out of control, we still observe the data consistency from Fig. 11-14

- The mean conductivity of the normal tissue is less than 15mS/cm up to 3.2GHz.
- Malignant tissues have higher mean permittivity and conductivity values than those of normal breast tissues
- Fat tissues have the lowest mean permittivity and conductivity values

This data consistency information provides the basis for breast cancer diagnosis using the dielectric properties in the microwave frequency range.

2.4. Discussion of the diagnostic values

It is misleading to use only the contrast of the mean values to judge the diagnostic value of the dielectric properties. Since the intrinsic heterogeneity in malignant tissue is large, this will decrease the mean contrast. The mean values from samples across patients will decrease the contrast as compared to an individual patient. Therefore, the diagnostic value of the dielectric properties seems to be underestimated, as in case 8. A better concept might be to use the contrast of the maximum value of the malignant tissue with the mean of the neighborhood normal tissue samples [2,13]. Better criterion can be defined using the probability of detection and false alarm, in which the random model of the point dielectric values and the spatially distributed dielectric values are incorporated.

In summary, we observed the diagnostic value of the dielectric properties from the data, as

- The low conductivity values of the normal breast tissue enable penetration of microwave frequencies up to the low GHz range, which coincides with the simulation results in [22].
- At 100MHz-1GHz, dielectric properties can significantly help classify normal and malignant tissues.
- At frequency ranges of 1GHz-3GHz, dielectric properties can help classify normal and malignant tissues.
- At 10kHz-1MHz, dielectric property can help classify normal, benign and malignant tissues, yet mainly depends on the conductivity.

2.5. Areas in need of more experiments

- The dielectric properties of benign tissues compared with that of the malignant tissues and normal tissues in the frequency range of 100MHz-3GHz.
- The spatial distribution of the dielectric properties of normal, benign and malignant breast tissues.
- The dielectric properties of human breast cancer in different development stages.

3. MECHANISM: NORMAL VS MALIGNANT TISSUE

We first review the mechanism of the dielectric properties of biological tissues in general.

The frequency dependence of dielectric properties of biological tissues is related to the polarization of molecules and structural interfaces in response to the applied electric field [9]. Data from Schwan and Foster on high water content muscle tissue suggests the presence of three dispersion regions: alpha, beta, and gamma, with the relaxation frequencies to be kHz, hundreds of kHz, and GHz [17]. The delta dispersion, located in half way between beta and gamma regions, has also been identified [1,18,19].

For engineering applications, the alpha dispersion has little significance [1]. Beta dispersion occurs at radio frequencies, and arises principally from the charging of cellular membranes, with smaller contributions from the protein constituents and ionic diffusion along surfaces in the tissue [1,18,19].

Tissues typically exhibit a small dispersion between 0.1 and 3GHz, which have been termed the delta dispersion [1,19] or "UHF relaxation" [18]. A combination of mechanisms are suggested for this region: bipolar relaxation of the water of hydration "bound" to proteins, a Maxwell-Wager effect due to ions in the cytoplasm collection against relative nonconductive protein surface and rotation of polar side-chains on the protein surface [1,9,18]. The relaxation frequency is dominant mostly by bound water (f_r of 100-1000 MHz [1], Protein molecules (f_r of 40-300 MHz) and free water ($f_r=25$ GHz).

The gamma dispersion occurs with a center frequency near 25GHz at body temperature, due to the dipolar relaxation of the free and bound water and ionic conductivity. Campbell and Land [14] attribute higher than expected conductivity at 3.2 GHz to the "tail end" of β -dispersion effects.

In recent studies, a variety of factors have been explored, which lead to pronounced difference in dielectric properties in normal compared with malignant tissues, as listed below:

Necrosis. Inflammation and necrosis are commonly found in malignant breast tissues. Presence of a necrosis leads to breakdown of cell membranes and thus a larger fraction of the tissue that can carry current at low frequencies [20], which decreases the capacitance of the tumor [2].

Charging of the cell membrane. In breast carcinoma, there is a progressive replacement of fat lobules with fibroblastic proliferation and epithelial cells. Which also accompanied by a variety of alterations at the transformed cell surface [12(22)]. Cancer cells have reduced membrane potentials and tend to have altered ability to absorb positive ions [19(77)], they have a higher negative surface charge on their membranes [9(4,21),19(78)]. According to Joines et.al., conductivity of the malignant tissues is increased with this mobile charge being displaced and rotated by the microwave field [9].

Relaxation times. The relaxation times in malignant tissues are larger than those in normal tissue, indicating that a significant increase in the motional freedom of water has occurred [19(75)]. Surowiec et.al.[13] reported that cancerous breast tissues have average dielectric relaxation times between 0.6 μ s and 1.4 μ s and the surrounding normal tissues had shorter relaxation times of 0.3 μ s.

Sodium concentration and water content. The sodium concentration in tumor cells is higher than in normal cells [19(76)]. The excessive sodium concentrations not only affect the cell membrane potentials [10, (9-11)], but causes malignant tissue to retain more fluid. According to Joines et.al, the excess sodium fluid alone would yield greater conductivity and permittivity values in malignant tissue than in normal tissue. In addition, the fluid is retained in the form of bound water, which has larger values of σ and ϵ than free water [10].

Malignant tissues have significantly higher water contents than normal tissues [18,19 (76)]. The data from Campbell and Land [14] illustrates the dielectric properties related with the water content at 3.2GHz of the breast tissues, as shown in Fig. 15 and 16. The relationship between relative permittivity and water content is strikingly similar to the relationship between

conductivity and water content. This leads to the conclusion that the same mechanism is responsible for the change in both dielectric properties.

Malignant breast tissue has a higher ratio of water content compared with that of the normal tissue, which coincides its higher values of permittivity and conductivity than normal breast tissue at the same microwave frequency. However, in this data taken at 3.2 GHz, there is not a marked difference in the water content of benign breast tissue and malignant tumor.

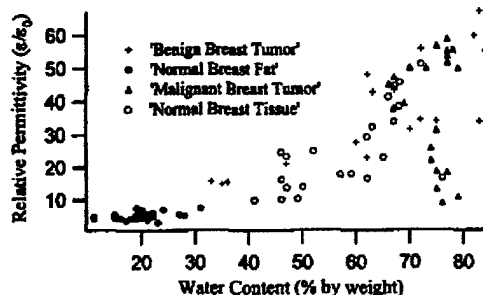


Figure 15 Relative permittivity of human breast tissue vs water content

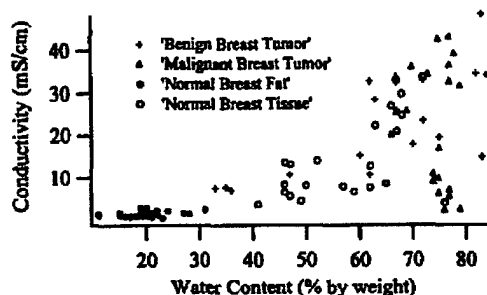


Figure 16 Conductivity of human breast tissue vs. water content

4. CONCLUSION

This paper presents an initial review and consolidation of the dielectric properties of normal, benign and malignant tissues in the range of 10kHz-20GHz. A brief explanation of the experiment methods is presented as well as the mechanisms that explain the difference in the dielectric properties of normal and malignant tissues. The consistency and inconsistency of the data are discussed as well as suggestions for the possible inconsistency. It is observed that the dielectric properties of breast tissue, even though containing uncertainty, have good diagnostic value in the range of 100MHz-3GHz.

ACKNOWLEDGEMENT

I appreciate Dr. Loren W. Nolte and Dr. William T. Joines's help of modifying this paper and I wish to thank Dr. Gary Ybarra and Dr. Qing H. Liu for their helpful discussions. This work was supported in part by NIH/NCI under grand 5PO1 CA42745-13.

REFERENCES

1. K.R. Foster and H.P. Schwan, Dielectric properties of tissues in CRC Handbook of Biological Effects of Electromagnetic Field, C. Polk and E. Postow Eds. Boca Raton, CRC Press, 1996
2. H. Fricke and S. Morse, "The Electric Capacity of Tumors of the Breast", *J. Cancer Res.*, vol. 16, pp. 310-376, 1926.
3. Morimoto, T., Kinouchi Y., Iritani T., "Measurement of the electrical bio-impedance of breast tumors". *Eur Surg Res.* 1990;22:86-92
4. Morimoto, T., Kimura, S. et al, "A study of the electrical bio-impedance of tumors", *J. Invest. Surg.* 1993;6:25-32
5. J. Jossinet, "Variability of impedivity in normal and pathological breast tissue", *Med. & Biol. Eng. & Computing* 1996;34:346-350
6. J. Jossinet, "The impedivity of freshly excised human breast tissue", *Physiol. Meas.* 1998;19:61-75
7. T.S. England and N.A. Sharples, "Dielectric Properties of the Human Body in the Microwave Region of the Spectrum Nature March 1949;163:487-488
8. T.S. England, "Dielectric Properties of the Human Body for Wavelengths in the 1-10 cm Range", *Nature Sep.* 1950;166:480-481
9. W. T. Joines, R. L. Jirtle, M. D. Rafal, D. J. Schaefer, "Microwave Power Absorption Differences Between Normal and Malignant Tissue", *Int. J. Radiation Oncology Biol. Phys.*, vol. 6, pp. 681-687, 1980.
10. W. T. Joines, "Frequency-Dependent Absorption of Electromagnetic Energy in Biological Tissue", *IEEE Transactions on Biomedical Engineering*, vol. BME-31, no. 1, pp. 17-20, January 1984.
11. E. Tanabe W.T. Joines, "A nondestructive method for measuring the complex permittivity of dielectric materials at microwave frequencies using an open transmission line resonator", *IEEE Trans. Instrumentation and Measurements* 1976;25:222-226
12. S. S. Chaudhary, R. K. Mishra, Arvind Swarup, Joy M. Thomas, "Dielectric Properties of Normal & Malignant Human Breast Tissues at Radiowave & Microwave Frequencies", *Indian Journal of Biochemistry & Biophysics*, vol. 21, pp. 76-79, February 1984.
13. A.J. Surowiec, S.S. Stuchly, J.R. Barr, A. Swarup, "Dielectric Properties of Breast Carcinoma and the Surrounding tissues", *IEEE Trans. Biomed. Eng.* 1988; Vol 35, No.4:257-263
14. A. M. Campbell, D. V. Land, "Dielectric properties of female human breast tissue measured *in vitro* at 3.2 GHz", *Phys. Med. Biol.*, vol. 37, no.1, pp. 193-210, 1992.
15. William T. Joines, Yang Zhang, Chenxing Li, and Randy L. Jirtle, "The measured electrical properties of normal and malignant human tissues from 50 to 900 MHz", *Medical Physics* April 1994;vol 21;4:547-550
16. Paul M. Meaney, Margaret W. Fanning, Dun Li, Steven P. Poplack, and Keith D. Paulsen, "A Clinical Prototype for Active Microwave Imaging of the Breast", *IEEE Transactions on Microwave Theory and Techniques*, vol. 48, no. 11, pp. 1841-1853, November 2000.
17. P. Debye *Polar Molecules*. New York, Dover. 1929, pp. 77-108.
18. K.R. Foster, J. L. Schepps, "Dielectric Properties of Tumor and Normal Tissues at Radio through Microwave Frequencies", *Journal of Microwave Power*, vol. 16, no. 2, pp. 107-119, 1981
19. R. Pethig "Dielectric Properties of Biological Materials: Biophysical and Medical applications", *IEEE trans. on Electrical Insulation* Oct. 1984;vol EI-19 No5:453-472S
20. R. Smith, K.R. Foster and J.L. Wolf, "Dielectric properties of VX-2 carcinoma vs. normal liver tissues", *IEEE trans Biomed. Eng.*, BME-33, 522, 1986
21. C. Gabriel, S. Gabriel, "Compilation of the Dielectric Properties of Body Tissues at RF and Microwave Frequencies", <http://www.brooks.af.mil/AFRL/HED/hedr/reports/dielectric/Title/Title.html>
22. J.R. Mallard, D.C. Lawn "Mammary tumor", *Nature* 1967;213:28-30
23. Constantine A. Balanis, *Advanced Engineering Electromagnetics*, John Wiley & Sons 1989, p146

PERFORMANCE ANALYSIS FOR BAYESIAN MICROWAVE IMAGING IN DECISION AIDED BREAST TUMOR DIAGNOSIS

Liewei Sha, Loren W. Nolte, Zhong Qing Zhang, and Qing H. Liu

Dept. of Electrical and Computer Engineering, Duke University
Durham, NC 27708-0291, lwn@ee.duke.edu

ABSTRACT

In this paper the Markov Random Field is used to model the breast permittivity cross section as a propagating medium, and incorporate it into the forward Electromagnetic (EM) propagation to predict the random field of the EM measurements at a received array of sensors. Given these EM field measurements, Bayesian approaches are then developed to compute the likelihood ratio for tumor-detection and the *a posteriori* probability display of tumor localization. Quantitative performance evaluations using simulations demonstrate the advantage of using the Bayesian approach to directly process the measurement data as compared to using the Bayesian or threshold approaches to detect and localize the tumor based on the reconstructed permittivity image.

1. INTRODUCTION

Microwave imaging is a promising new modality for breast cancer diagnosis, partly because it is non-invasive and the permittivity contrast between normal and malignant breast tissues is high [1]. In addition, the attenuation of EM propagation in normal breast tissues is low so that it can penetrate into the depth of the tissue [1]. Most of the research in this field has focused on the study of the dielectric properties [1, (1-22)], the design of the microwave imaging prototypes [2], and the improvement of the EM forward and inverse algorithms [3][4][5]. However, none of this research has incorporated signal detection theory directly into the microwave imaging at the measurement level. Markov Random Fields (MRF Hammersley and Clifford [6]) and detection theory have been applied in mammography for diagnosis, such as [7][8][9]. However, [7] and [8] only assumed a simple deterministic disk object model. [9] did not utilize the *a priori* knowledge of the projections. This paper presents Bayesian algorithms for Scattered Electromagnetic fields through an Uncertain Permittivity Image (BP_SEUPI), which incorporates the knowledge of the *a priori* permittivity image modeled by the MRF, the measurement noise, as well as the physical model of the forward scattered electric field. The Bayesian algorithms for the Uncertain Permittivity Image (BP_UPI) and the Threshold Image Proces-

sors (TIP) are also presented for comparisons. It should be noted that the forward EM scattering field is computed using the Extended Born Approximation (EBA) accelerated CGFFT method, which has been proposed by Zhang and Liu in [4][10]. The reconstructed permittivity image is obtained using the EBA as the initial solution followed by the Contrast Source Inversion (CSI [11]) method, which has been proposed by Zhang and Liu [4].

2. DIAGNOSIS MODEL

The binary hypotheses considered are:

H_0 : No tumor present

H_1 : Tumor (size $L \times L$) present, located at an unknown position S on the 2D lattice Ω of the permittivity cross section.

The decision as to whether the tumor is present or not, i.e. whether H_0 or H_1 is true, is the detection problem. Where the tumor is located if H_1 is true, is considered to be a localization problem.

The data for the BP_SEUPI are the microwave measurements r , shown in the middle of the Fig. 1. r is composed of concatenating pieces. Each piece is a complex $K \times 1$ vector representing the narrow-band frequency component of the scattered electric field sampled by K sensors, from a single transmitter, which is one of the K sensors. It assumes $r = s + n$, s is the signal, and n is the additive noise at the sensors, modeled by a multivariate complex Gaussian distribution, with zero mean and $\sigma_n^2 I_K$ covariance matrix. The signal to noise ratio (SNR) is given by $10 \log_{10}(\frac{\|s\|^2}{\sigma_n^2})$ (dB). The propagating medium of the EM field is the uncertain permittivity image modeled by the MRF, a sample of which is shown in the left of Fig. 1.

The data for BP_UPI and TIP is the reconstructed permittivity image $\epsilon_r = T^{-1}(r)$, as shown in the right of Fig. 1 where T^{-1} represents the reconstruction procedure.

The uncertainties in this problem are the tumor position, the noise at the sensors, as well as the spatial distribution of the breast permittivity which reflects statistically the tissue variance in individuals and the background structure variance across patients.

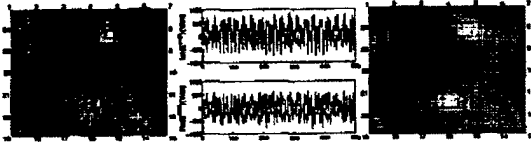


Fig. 1. Numbers 1-24 represent the sensors. Left: original tissue permittivity image; Middle: real and imaginary part of a sample measurement data; Right: reconstructed tissue permittivity image.

2.1. Model of Breast Permittivity Image

We utilize the MRF to model the breast permittivity image, because it implements the idea that spatially nearby tissue permittivities are similar. The Gaussian MRF (GMRF, Chellappa [6]) is selected because it provides a simple form to be incorporated in the Bayesian approaches. It is important to realize that this model is statistical, and is not intended to be a model of the detailed deterministic structure of permittivity of a particular individual. The GMRF is defined as

$$p(x_{ij} | x_{kl} \in \Omega \setminus \{(i, j)\}) = \frac{\exp(-\frac{1}{2\sigma_{ij}^2}(x_{ij} - (\mu_{ij} - \sum_{kl \in N_{ij}} \beta_{(ij),(kl)}(x_{kl} - \mu_{kl})))^2)}{\sqrt{2\pi\sigma_{ij}^2}} \quad (1)$$

where μ_{ij} and σ_{ij}^2 are the mean and variance at (i, j) . $\beta_{(ij),(kl)}$ are the interaction coefficients. The β 's provide two kinds of information: one is the neighborhood of (i, j) , i.e. N_{ij} which implies that the permittivity at (i, j) only depends on the permittivities in its neighborhood. Another is the influence of the neighbors on the point (i, j) , as represented by the sign and value of the interaction coefficients.

We assume the permittivity image size is $9.2\text{cm} \times 9.2\text{cm}$, 529 pixels. The tumor size is 25 pixels. The mean values of tumor and background are $\mu_t = 40$ and $\mu_b = 30$, whose values are similar to normal and malignant breast permittivity values from experiments [1]. The interaction coefficients of tumor and background are β_t with 3 pixel correlation length and β_b with 20 correlation length. An algorithm proposed by Rue [12] is used to fit the interaction coefficients to the Gaussian field. Applying Hammersley-Clifford theorem [6], given Eqn.1, we derive the mean vector μ and μ_S , covariance matrix Q and Q_S of the joint pdf of the permittivity image under the H_0 and H_1 conditions respectively. Subscript S denotes the tumor position.

2.2. Detection and Localization Approaches

According to signal detection theory, the optimal detector is the likelihood ratio of the data vector followed by a threshold whose value is determined by the optimum criterion

(T.G.Birdsall). The optimal localization processor calculates the *a posteriori* probability of the tumor position given the data vector. We derive the likelihood ratios (λ) for the Bayesian detector and threshold detector, as well as the *a posteriori* probability image for the Bayesian localization processors. We assume that the unknown tumor position has a uniform distribution *a priori* on the 2D lattice Ω .

2.2.1. Bayesian Processor for Scattered EM field propagated through the Uncertain Permittivity Image (BP-SEUPI)

detector $\lambda(r) \propto$

$$\frac{\sum_{S \in \Omega} \int_{\epsilon_r} \exp(-\frac{(r-T(\epsilon_r))^T(r-T(\epsilon_r))}{2\sigma_r^2}) p(\epsilon_r | H_1, S) d\epsilon_r}{\int_{\epsilon_r} \exp(-\frac{(r-T(\epsilon_r))^T(r-T(\epsilon_r))}{2\sigma_r^2}) p(\epsilon_r | H_0) d\epsilon_r} \quad (2)$$

localization processor

$$p(S|r) \propto \int_{\epsilon_r} \exp(-\frac{(r-T(\epsilon_r))^T(r-T(\epsilon_r))}{2\sigma_r^2}) p(\epsilon_r | H_1, S) d\epsilon_r. \quad (3)$$

Both the BP-SEUPI detector and the localization processor require a high dimensional integration, which is a tough problem. This paper tries to overcome this difficulty by using a multivariate complex Gaussian distribution to approximate the random field of the measurements data, which has been found to have good performance in the simulations.

2.2.2. Bayesian Processor for Uncertain Permittivity Image (BP-UPI)

detector $\lambda(\epsilon_r) \propto$

$$\sum_{S \in \Omega} |Q_S| \exp(-\frac{(\epsilon_r - \mu)^T Q (\epsilon_r - \mu) - (\epsilon_r - \mu_S)^T Q_S (\epsilon_r - \mu_S)}{2}) \quad (4)$$

localization processor

$$p(S|\epsilon_r) \propto |Q_S| \exp(-\frac{(\epsilon_r - \mu_S)^T Q_S (\epsilon_r - \mu_S)}{2}) \quad (5)$$

2.2.3. Threshold Image Processor (TIP)

detector $\lambda = \max_{\epsilon_r} \quad (7)$

localization processor $S = \max_{S \in \Omega} \epsilon_r(S) \quad (8)$

3. SIMULATION RESULTS

3.1. An example

Fig. 2a) shows an example of a stochastic background permittivity image of the tissue, along with a simulated tumor, modeled by the GMRF. Fig. 2b)-d) are the reconstructed permittivity images from the perfect measurement data as well as from 60dB and 50dB noisy measurement data. The

signal detection approach using the permittivity data computes the *a posteriori* probability of the tumor location given either the original permittivity image, or the reconstructed image as data. Fig. 2e gives an upper bound on tumor localization by plotting the *a posteriori* probability of tumor location using the tissue data of Fig. 2a. Fig. 2f-h shows the *a posteriori* plots of tumor location based on post processing the reconstructed tissue data shown in Fig. 2b-d. Fig. 2j-l shows the *a posteriori* plot of tumor location based on the same measurements used to get the reconstructions in Fig. 2b-d.

Plots 2g-h show that at the 60dB and 50dB SNR condition, the BP.UPI using the reconstructed data misses the correct location of the tumor, and Fig. 2k-l shows that the BP.SEUPI using the measurement data gets the correct tumor localization with high probability. This is a specific example where the BP.SEUPI works better. In the following sections, it is demonstrated statistically that the processors using the measurement data have better performance.

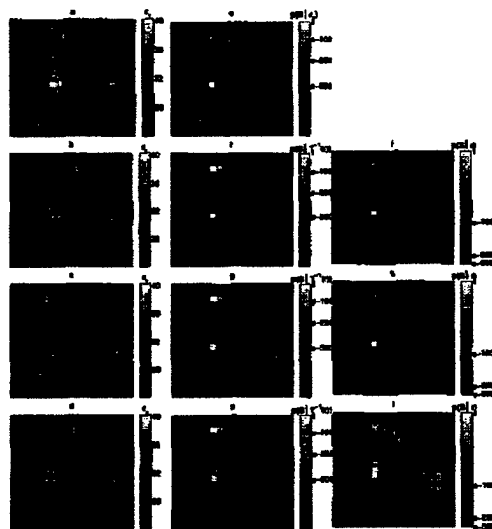


Fig. 2. a) Original tissue permittivity image; b)-d) Reconstructed permittivity from the measurement data b) without additive noise c)d) with additive noise, c) 60dB SNR d) 50dB SNR; e)-h) the *a posteriori* probability of the tumor position given the permittivity image data - $p(S | \epsilon_r)$, data ϵ_r comes from a)-d); j)-l) the *a posteriori* probability of the tumor position given the measurement data - $p(S | r)$

3.2. Detection performance

Fig. 3a) illustrates the detection performance comparisons assuming no additive noise. In 3a) the ROC of the thresh-

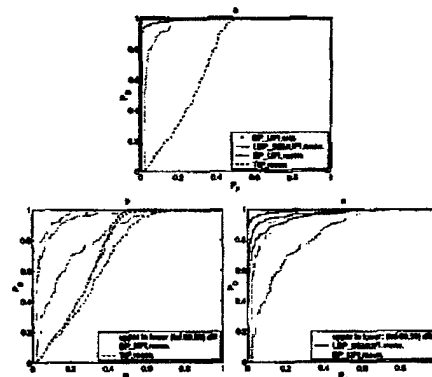


Fig. 3. The detection performance of the BP.UPI using original tissue data, BP.UPI using reconstructed permittivity image data, TIP using reconstructed permittivity image data and BP.SEUPI using measurement data. a) no additive noise presents at sensors; b)c) [Inf, 60, 50] dB noise at sensors b) BP.UPI & TIP c) BP.UPI & BP.SEUPI

old detector provides a performance lower bound. The TIP mimics the way a routine visual examination of the image might be done. Although it is not sophisticated, its ROC reflects the problem of high positive predictive Value (PPV) of conventional mammography. Using the reconstructed permittivity image data, the BP.UPI detector is much better than the TIP detector, especially when the probability of false alarm is low, because the BP.UPI utilizes the *a priori* knowledge of the tissue background across patients and the *a priori* knowledge of the different characteristics of the normal and malignant tissues to improve the detection performance.

Fig. 3a) also shows that the BP.SEUPI detector using the measurement data is better than BP.UPI detector using the reconstructed permittivity data, yet worse than BP.UPI detector using the original permittivity data. In reality, we do not have access to the original tissue permittivity image directly but to the EM measurements. However, this provides an upper bound for performance evaluations. The BP.UPI detector using the original permittivity data is better than the BP.SEUPI because the forward EM field maps the variables from the original permittivity domain to the measurement domain, which shrinks the random variable space and decreases the detectability.

Fig. 3b)c) compares the performance of the detectors when noise is present. It indicates that sensor noise degrades all the detection performances. It also demonstrates that for three SNR conditions, both Bayesian detectors are better than the threshold detector and the BP.SEUPI is better than the BP.UPI using the reconstructed permittivity data.

3.3. Localization performance

Fig. 4 shows the localization performance of the BP_SEUPI using the measurement data, and the BP_UPI and TIP using the reconstructed tissue permittivity data. The localization

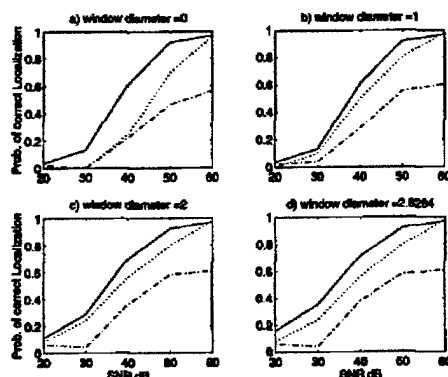


Fig. 4. Localization performances: solid line, BP_SEUPI using the measurement data; dotted line, BP_UPI using the reconstructed tissue permittivity data; dashed line, TIP using the reconstructed tissue permittivity data

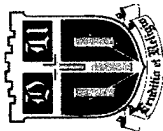
performance is shown using the probability of correct localization (PCL) curves. PCL is obtained by computing the ratio of the number of correct localizations over the total trials. The localization is correct if the located tumor position is within the test window. If it is required that the located position is exactly the same as the real position to be true, the window diameter is zero. For the other values of the window diameter: 1, 2, 2.8284, the window sizes are 9, 13, 25 pixels. Fig. 4 shows that at 50dB or 60dB SNR condition, both the BP_UPI and the BP_SEUPI have better performance than 0.9 PCL. They are much better than the threshold approach for all the tested SNR conditions. The BP_SEUPI localization using the measurement data is the best of the three.

4. CONCLUSION

The results of the detection and localization performances show that the decision-aided Bayesian microwave imaging approach proposed in this paper, BP_SEUPI, has the potential of providing additional and useful information for radiologists. It is an algorithm whose goal is at the heart of the ultimate decisions; i.e. is a tumor present, and if so where. It benefits from incorporating the *a priori* knowledge, although uncertain, of normal and malignant breast permittivity. It also gains a decision performance advantage by processing the measurements directly rather than as a post processor to a reconstructed image.

5. REFERENCES

- [1] Liewei Sha and Erika R. Ward etc., "A review of dielectric properties of normal and malignant breast tissue," *Accepted by IEEE SoutheastCon2002, April*.
- [2] P. M. Meaney and K. D. Paulsen etc., "A clinical prototype for active microwave imaging of the breast," *IEEE Transactions on Microwave Theory and Techniques*, vol. 48, no. 11, pp. 1841–1853, Nov. 2000.
- [3] Q. H. Liu Z. Q. Zhang T. Wang G. Ybarra L. W. Nolte J. A. Bryan W. T. Joines, "Active microwave imaging I: 2-D forward and inverse scattering methods," *IEEE Trans. Microwave Theory Tech.*, vol. 50, no. 1, pp. 123–133, Jan 2002.
- [4] Z. Q. Zhang and Q. H. Liu, "Two nonlinear inverse methods for electromagnetic induction measurements," *Geosci. Remote Sensing*, vol. 39, no. 6, pp. 1331–1339, June 2001.
- [5] S. C. Hagness A. Taflov et al., "Three-dimensional fdtd analysis of a pulsed microwave confocal system for breast cancer detection: Design of an antenna-array element," *IEEE Trans. Antennas and Propagation*, vol. 47, pp. 783–791, May 1999.
- [6] S. Z. Li, *Markov Random Field Modeling in Computer Vision*, Comp. Sci. Workbench. Springer, 1995.
- [7] D. J. Rossi and A. S. Willsky, "Reconstruction from projections based on detection and estimation of objects-part i and ii: Performance analysis and robustness analysis," *IEEE Trans. on ASSP*, vol. ASSP-32, no. 4, pp. 886–906, August 1984.
- [8] D. Jalilal and L. W. Nolte, "Signal detection theory and reconstruction algorithms - performance for images in noise," *IEEE trans. on Biomedical Engineering*, vol. 41, no. 5, pp. 501–504, May 1994.
- [9] H. D. Li M. Kallergi etc., "Markov random field for tumor detection in digital mammography," *IEEE trans. on Medical Imaging*, vol. 14, no. 3, pp. 565, Sep 1995.
- [10] Z. Q. Zhang and Q. H. Liu, "Reconstruction of axisymmetric media with an fft enhanced extended born approximation," *Inverse Problems, invited paper*, vol. 16, no. 5, pp. 1281–1296, 2000.
- [11] P. M. Berg and R. E. Kleinman, "A contrast source inversion method," *Inverse Problems*, vol. 13, pp. 1607–1620, 1997.
- [12] H. Rue and H. Tjelmeland, "Fitting gaussian markov random fields to gaussian fields," *Statistics, NO.16*, 1999.



Decision Aided Algorithms for Breast Tumor Diagnosis Using Microwave Diffraction Measurements

Liewei Sha, Loren W. Nolte, Zhong Qing Zhang and Qing Huo Liu
Department of Electrical and Computer Engineering, Duke University, Durham, NC

INTRODUCTION

Microwave energy has the advantages that at low power levels there are no radiation dangers, no contrast agents, and the examinations are comfortable. The proposed approach addresses directly the decision-theoretic task of detection and localization of breast tumor, using microwave diffraction measurements. Bayesian detection theory is used to improve the probability of correct detection and localization. This improvement in performance is possible because conventional imaging techniques, by themselves, usually emphasize resolution and contrast, and leave the incorporation of uncertainties and decisions primarily to algorithms or human observers that post process the reconstructed image. This approach augments conventional medical image processing and provides additional processing of the scattered microwave field to aid the radiologist in dealing with uncertainties that are an inherent part of the decisions.

Sha et al have compiled results from experiments in the literature that show that the microwave dielectric properties of malignant tissue are different from those of normal breast tissue. Signal detection theory, in its most fundamental form, provides a framework for incorporating this knowledge of breast tissue characteristics directly into the design of optimal task oriented information processing algorithms to aid in the detection of breast cancer. In addition, signal detection theory enables one to obtain upper limits of detection and localization performance as a function of uncertainties in the microwave properties of breast tissues, using quantitative measures such as the ROC (probability of detection vs. false alarm) and PCL (probability of correct localization). The proposed algorithm uses the direct microwave diffraction measurements and incorporates the fact that spatially adjacent tissues are similar in their permittivity values, but normal and malignant breast tissues have high contrast in the mean.

Using the ROC and PCL performance measures and simulations, the best tumor detection and localization performance for microwave imaging is shown as a function of tumor contrast, tumor size, and tumor local characteristics. Also, the performance of the proposed statistical decision based algorithm is compared to another one that post processes reconstructed images of breast permittivity¹. These results demonstrate the advantages of incorporating the microwave diffraction measurements directly into the computer-aided algorithm design.

¹ In the simulation, the microwave diffraction measurements are computed using the Extended Born Approximation (EBA) accelerated COFFT method (proposed by Zhang and Liu) with an ensemble of simulated breast permittivity images as the propagating media.
² The reconstructed permittivity images are obtained using back-propagation following by Contrast Source Inversion (CSI, Berg), which was proposed by Zhang and Liu.

2 QUANTITATIVE PERFORMANCE EVALUATION

Receiver Operating Characteristic (ROC)
Alarm (P_d) $P_d = \int_0^1 dP(\lambda/H_0) \quad P_d = \int_0^1 dP(\lambda/H_1)$
• ROC's are obtained in general through a simulation of λ under H_0 and H_1 conditions.

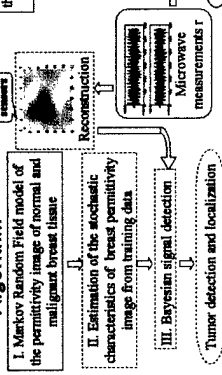
Detectability (or Detection Coefficient) d
 d characterizes the ROC curve for the detection problem exactly plus white Gaussian noise, where $P_d = 1 - \text{Ga}(2\pi\sigma^2/(2\pi\sigma^2(1-P_d)))$.
• Here, d is estimated from the ROC curve. Each point on the Detectability curve represents an approximation to one ROC curve.

Probability of Correct Localization (PCL)

PCL is the ratio of correct localization counts over total trials.
• PCL is estimated from the ROC curve. Each point on the Detectability curve represents an approximation to one ROC curve.
• The target window is a circle with fixed radius (circle).

1 APPROACH

Post-Reconstruction Algorithm



Proposed Algorithm

I. Markov Random Field model of the permittivity image of normal and malignant breast tissue

II. Estimation of the stochastic characteristics of the microwave diffraction measurements with the training breast permittivity images as the propagation media

III. Bayesian signal detection and localization

Tumor detection and localization

I Local characteristic of breast permittivity

Global characteristic of breast permittivity
Gaussian Markov Random Field (GMRF) (Chellappa, 1983)
 $p(\epsilon_i) = \frac{1}{(2\pi)^{N/2}} \exp(-\frac{1}{2}(\epsilon_i - \mu)^T \Sigma^{-1}(\epsilon_i - \mu))$

No tumor present
 $Q_1: N(\mu_0, \Sigma_0)$, composed of β_0 or 0
 $U_1: N(\mu_1, \Sigma_1)$, composed of β_1

Tumor present at location S
 $Q_2: N(\mu_0, \Sigma_0)$, composed of β_0 or 0
 $U_2: (U_1 - \beta_1) \otimes \text{tumor mean function} - \beta_1$

Some realizations of breast permittivity image
No tumor present
Tumor present at location S

Normal breast tissue: mean β_0 , interaction coefficient matrix β_1

Malignant breast tissue: mean β_1 , interaction coefficient matrix β_2

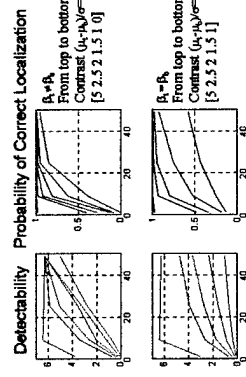
II Bayesian Processor for Scattered EM Field of Uncertain Permittivity Image

Binary Hypotheses: $H_0: \epsilon_i = T(\epsilon_0, \beta_0)$, $H_1: \epsilon_i = T(\epsilon_1, \beta_1)$
BP_SEUPI detector: BP_SEUPI localization processor
 $\lambda(\epsilon_i) = \frac{1}{\sum_{j=1}^2 p(\epsilon_j | \epsilon_i, \beta_j) T(\epsilon_j, \beta_j)} \cdot \frac{p(\epsilon_i | \epsilon_0, \beta_0) T(\epsilon_0, \beta_0)}{p(\epsilon_i | \epsilon_1, \beta_1) T(\epsilon_1, \beta_1)}$

• High dimensional integral is simplified by using multivariate complex Gaussian distribution as an approximation to $p(T(\epsilon_0, \beta_0) | \epsilon_i)$, which is called LBP_SEUPI (Low order BP_SEUPI)

LBP_SEUPI localization processor
 $\lambda(\epsilon_i) = \frac{1}{\sum_{j=1}^2 p(\epsilon_j | \epsilon_i, \beta_j) T(\epsilon_j, \beta_j)} \cdot \frac{p(\epsilon_i | \epsilon_0, \beta_0) T(\epsilon_0, \beta_0)}{p(\epsilon_i | \epsilon_1, \beta_1) T(\epsilon_1, \beta_1)}$
• $M_1 = C_1 \cdot (1/2\pi\sigma_1^2) \cdot C_2 \cdot (1/2\pi\sigma_2^2) \cdot C_3 \cdot (1/2\pi\sigma_3^2)$

2.1 PERFORMANCE UPPER BOUND



Incorporating statistical models of tissue permittivity into an optimal signal detection theory framework for the detection of breast cancer at microwave frequencies

Liewei Sha, Loren W. Nolte, Zhong Qing Zhang and Qing Huo Liu

Abstract— This paper addresses directly the decision-theoretic task of detection and localization of breast tumor using microwave measurements and optimal signal detection theory. Microwave energy has the advantages that at low power levels there are no radiation dangers, no contrast agents, and the examinations are comfortable. An optimal signal detection theory framework is used to improve the probability of tumor detection for a fixed probability of false alarm. 2D Markov Random field statistical models that characterize the spatial properties of both benign and malignant breast tissue permittivity are incorporated into the forward electromagnetic (EM) propagation to predict the random field of the EM measurements at a received array of sensors. This information in turn is incorporated into a likelihood ratio algorithm for tumor detection. Examples of Receiver operating characteristics (ROC) and probability of correct localization (PCL) curves are presented as a function of local uncertain tissue permittivity characteristics, and tumor contrast, size, and shape, and compared with algorithms that optimally post process a reconstructed image. Computationally simpler tumor detection and localization algorithms, simulations of their convergence, and approximations to the ROC using the detectability index are presented. Simulations also indicate the effect of the sensor array configuration on tumor detection performance.

Keywords— Bayesian, detection, localization, microwave imaging, breast tumor, permittivity

I. INTRODUCTION

Breast cancer is a significant public health problem for women in the world. The major traditional modality for breast cancer diagnosis is X-ray mammography. It is relatively cheap and fast, but it exposes the body to ionized radiation. In order to operate within safe limits, the contrast of the images tends to be low. Microwave imaging is a promising new modality for breast cancer diagnosis, because it is non-invasive and the normal and malignant tissues of the breast have high contrast in dielectric properties in certain ranges of the electromagnetic (EM) frequencies [1], [2], [3], [4], [5], [6]. In addition, the attenuation of EM propagation in normal breast tissues is low so that it can also penetrate into the depth of the tissue [7], [8], [9], [10]. At this time, breast microwave imaging is not intended to replace X-rays, but to provide additional information to the radiologist to improve the performance of breast cancer diagnosis.

Most of the research in this field has focused on the experimental and theoretical study of the dielectric properties of breast tissue at microwave frequencies [1-10], the design of microwave imaging prototypes [11] and the improvement of 2D and 3D EM reconstruction algorithms [12], [13], and [14]. However, none of this research has incorporated signal detection theory directly into microwave imaging. Bayesian theory has been applied in mammography for diagnosis, such as [15][16][17]. However, [15] and [16] did not incorporate a random model of the tissue being imaged, but assumed a simple deterministic disk object model. In [17] the reconstructed tissue image was post-processed, but the propagation model was not fully utilized. In [18], initial performance analysis was presented using a Bayesian microwave imaging approach. This paper includes the comparison of two Bayesian signal detection theory approaches for tumor detection and localization. In one approach the spatial uncertainty of the tissue permittivity is included in the forward EM propagation, and optimal signal detection theory is applied to the raw received sensor information, i.e. without prior reconstruction of an image. In the other approach, signal detection theory is applied as a postprocessor to the reconstructed image.

In this paper the physics-based statistical decision theory model is introduced first. Second, the Markov Random Field (MRF) [19] is presented which is used to represent the uncertainty in the permittivity of the breast tissue. Optimal physics-based signal detection theory is used to develop an image processing algorithm for both detection and tumor localization that incorporates the uncertainty of EM propagation through a tissue medium with uncertain permittivity. Optimal signal detection theory is also used to develop an image processing algorithm that incorporates uncertainty as a post processor to a reconstructed image. Algorithms are also developed for obtaining upper and lower bounds of detection performance, some of which greatly improve the speed with which performance bounds can be computed. Finally, simulation results are presented for: 1) the detection and localization performance as a function of tumor contrast, size, local uncertain tissue permittivity characteristics, and shape. 2) the convergence of the model covariance matrix estimation as support for the number of Monte Carlo trials for the Bayesian approaches 3) comparison of the optimal physics-based detection and localization approaches that incorporate uncertainty in the

EM propagation with reconstructed image post processing and 4) the effect of the sensor array configuration on the performances. The appendix includes a proof of the inequality of the signal detection theory deflection coefficients from original, measurement and reconstruction data.

II. PHYSICS-BASED STATISTICAL DECISION THEORY MODEL

In this paper the problem of malignant tissue detection is placed within the framework of physics-based driven signal detection theory. The decisions are first, the detection problem, is a tumor present or not somewhere in the tissue? Secondly, the localization problem, if present somewhere, where is its location? We are particularly interested in improving the early detection and localization performance for the more difficult, and less obvious, situations due to uncertainties in tissue characteristics. The detection problem can be expressed by the binary hypotheses

H_1 : Malignant tissue present, regardless of its particular location, shape, and microwave permittivity characteristics.

or

H_0 : No malignant tissue present

The basic objective is to make optimal decisions about whether H_1 or H_0 is true and if H_1 is true, what is the best estimate of the size, location, and permittivity characteristics of the tissue.

The GMRF model presented in section III is used to characterize the uncertainty in the permittivity of benign and malignant tissue. An example realization of a 2D cross section of tissue permittivity using this model, and a particular sensor array configuration, is illustrated in Figure 1a. In this case, 24 sensors are arranged in a rectangle surrounding the tissue. It is important to realize that our characterization is statistical so that the model does not convey detailed deterministic anatomical features. The conductivity data is assumed to be a known constant for simplicity. The numbers 1-24 show the positions of sensors of one of the sensor array configurations used in this paper. All 24 sensors can both transmit and receive microwave signals, as in a tomographic situation.

The microwave measurements at the sensors are represented by a $K^2 \times 1$ complex row vector $r = [r_1, r_2, \dots, r_K]$, where r_i is a $K \times 1$ complex row vector, representing the data relevant to the i th transmitter. K is the number of sensors. An illustration of one realization of the measurement vector r , real and imaginary components, is shown in figure 1b, with $K^2 = 576$. These measurements are result of the scattered electromagnetic field that has propagated through the uncertain permittivity media. This is an example of data used by the Bayesian approach which incorporates directly the uncertainty of the raw measurements. More specifically, under the H_1 hypothesis, the data vector

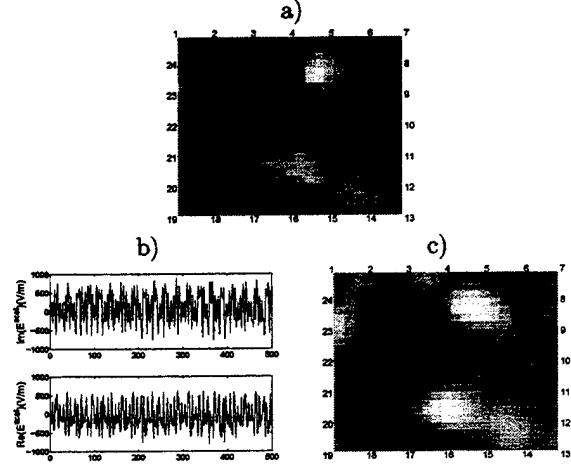


Fig. 1. a) original tissue permittivity image. b) measurements of scattered electric field (mV/m). c) reconstructed tissue permittivity image. Numbers 1-24 represent the array configuration.

r can be expressed as:

$$\begin{aligned} r &= s + n \\ s_i &= E_z^{scat}(p_R, q_T), R = 1 \dots K, T = 1 \dots K \\ SNR(dB) &= \frac{E_s}{\sigma_n^2} = \frac{\|s\|^2}{\sigma_n^2} \end{aligned} \quad (1)$$

where R represents the sensor as a receiver and T represents the sensor as a transmitter. By using each sensor as the transmitter in turn, and all sensors as receivers, we obtain the data vector r . s is the pure signal, a $K^2 \times 1$ complex vector. n represents the additive noise at the sensors. $n \sim \mathcal{N}(0, 2\sigma_n^2 I_{K^2})$. \mathcal{N} notifies a multivariate complex Gaussian distribution ([20]). I_{K^2} is an Identity covariance matrix with size $K^2 \times K^2$.

The other data representation that is used is that of the reconstructed permittivity image $\epsilon_r = T^{-1}(r)$, an example of which is shown in figure 1c, where T^{-1} represents the reconstruction procedure.

Many different types of uncertainties can be incorporated into the information processing. In this paper, the principal uncertainties considered are the spatial uncertainty of both benign and malignant breast tissue permittivity, tumor position, its size and shape, and the noise at the sensors.

A. Measurements

The pure measurement data is obtained by computing the scattered electric field through the uncertain tissue media, using the Extended Born Approximation (EBA) implemented with the improved CGFFT method, which is proposed by Zhang and Liu in [13][21]. The electric field can be expressed as

$$E_z = E_z^{inc} + E_z^{scat}, \quad (2)$$

where E_z^{inc} is the incident field from an infinite line current source J_z

$$E_z^{inc}(p) = -j\omega\mu_0 \int_D dq G(p, q) J_z(q). \quad (3)$$

E_z^{scat} is the scattered field

$$E_z^{scat}(p_R, q_T) = \int_D dq G(p_R, q) \Delta_k^2(q) E_z(q, q_T) \quad (4)$$

where q_T and p_R are the transmitter and receiver positions. $\Delta k^2(q) = k^2(q) - k_b^2$ and $k_b^2 = \omega^2 \mu_0 \epsilon_b - j\omega \mu_0 \sigma_b$. D is the inhomogeneous object domain. G is the Greens function for a homogeneous background medium

$$G(p, q) = \frac{1}{4j} H_0^{(2)}(k_b |p - q|). \quad (5)$$

The EBA method exploits the fact that $G(p, q)$ is close to $\delta(p - q)$ to approximate Eq. 4 as

$$E_z^{scat}(p_R, q_T) = E_z(p_R, q_T) \int_D dq G(p_R, q) \Delta_k^2(q). \quad (6)$$

Substituting Eq. 6 into Eq. 2, we obtain the solution of the electric field

$$E_z(p) = (1 - \int_D dq G(p, q) \Delta k^2(q))^{-1} E_z^{inc}. \quad (7)$$

The approximation of the scattered field is obtained by substituting Eq. 7 into Eq. 4. With the improved CGFFT method ([13][21]), the approximate scattered electric field can be computed using

$$\begin{aligned} E_z^{scat} &= \mathcal{F}^{-1} \{ \mathcal{F}[G] \mathcal{F}[J^{(EB)} E_z^{inc}] \} \\ J^{(EB)}(p) &= \Delta k^2 (1 - \mathcal{F}^{-1} \{ \mathcal{F}[G] \mathcal{F}[\Delta k^2] \}) \end{aligned} \quad (8)$$

B. Reconstruction

A reconstructed image example, shown in figure 1c, is obtained using the back-propagation as initial solution followed by the contrast source inversion(CSI Berg[22]) method, which is proposed by Zhang and Liu[13]. A summary of CSI is given below. First define the contrast source $\omega(p)$ as

$$\omega(p) = \chi(p) E_z(p), \quad \chi(p) = \Delta_k^2(p) / k_b^2. \quad (9)$$

The scattered field can be expressed as

$$E_z^{scat}(p) = k_b^2 \int_D dp G(p, q) \chi(q) E_z(q). \quad (10)$$

The scattered field is measured in the domain S (outside D) where χ vanishes. Assuming no measurement error, the measurement data r satisfies

$$r(p) = k_b^2 \int_D dp G(p, q) \chi(q) E_z(q), \quad p \in S \quad (11)$$

We have the state equation and the data equation

$$\begin{aligned} \omega(p) &= \chi E_z^{inc} + \chi G_D \omega, \quad p \in D, \\ r(p) &= G_{S\omega}, \quad p \in S, \end{aligned} \quad (12)$$

where $G_D \omega$ and $G_S \omega$ are defined as

$$G_{D,S\omega} = k_b^2 \int_D dp G(p, q) \chi(q) E_z(q), \quad p \in D \quad \text{or} \quad p \in S \quad (13)$$

The contrast source can be obtained by minimizing the cost function $F(\omega, \chi)$, which is the summation of the error in the data equation and state equation.

$$F(\omega, \chi) = (\sum_{j=1}^K \|r_j\|_S^2)^{-1} \sum_{j=1}^K \|r_j - G_{S\omega_j}\|^2 + (\sum_{j=1}^K \|\chi E_z^{inc} j\|_D^2)^{-1} \sum_{j=1}^K \|\chi E_z^{inc} - \omega_j + \chi G_D \omega_j\|_D^2, \quad (14)$$

The Polak - Ribière conjugate gradient procedure is used to update both ω and χ alternately.

III. MODEL OF UNCERTAIN PERMITTIVITY TISSUE IMAGE

In this section the uncertainties in the spatial distribution of the breast permittivity properties are modeled statistically. First, the random model for the tissue permittivity image in general is presented. Then the random model that designates both the normal tissue and the malignant tumor is presented.

A. Model of tissue permittivity image

We utilize the Markov Random Field(MRF [19]) to model the spatial uncertainties of the breast permittivity image. The MRF model implements the idea that the permittivity of spatially nearby tissue is similar. It does not model the detailed deterministic anatomical structure. The Markov property captures the local nature of the permittivity distribution and thereby reduces the uncertainty space. A Markov Random Field satisfies[23]

$$p(x_{ij}|x_{kl} \in \Omega \setminus \{(i, j)\}) = p(x_{ij}|x_{kl} \in \mathcal{N}_{ij}), \quad (15)$$

where \mathcal{N}_{ij} is the neighborhood system of (i, j) .

There are several MRF models, such as Auto-Models, Multi-Level Logistic Models. The Gaussian MRF (GMRF,[24][23], one of Auto-Models), is chosen because it can easily be incorporated into the Bayesian approaches. It can be defined as

$$p(x_{ij}|x_{kl} \in \Omega \setminus \{(i, j)\}) = \frac{e^{-\frac{1}{2\sigma_{ij}^2}(x_{ij} - (\mu_{ij} - \sum_{kl \in \mathcal{N}_{ij}} \beta_{(ij),(kl)}(x_{kl} - \mu_{kl})))^2}}{\sqrt{2\pi\sigma_{ij}^2}}, \quad (16)$$

where μ_{ij} and σ_{ij}^2 are the mean and variance at (i, j) . and $\beta_{(ij),(kl)}$ are the interaction coefficients, which reflect the local characteristics. The matrix form of $\beta_{(ij),(kl)}$ can be expressed as

$$\beta = \begin{bmatrix} \beta_{0,0} & \beta_{0,1} & \dots & \beta_{0,M} \\ \beta_{1,0} & \beta_{1,1} & \dots & \beta_{1,M} \\ \dots & \dots & \dots & \dots \\ \beta_{M,0} & \beta_{M,1} & \dots & \beta_{M,M} \end{bmatrix}, \quad (17)$$

where $\beta_{ij,kl}$ has been simplified to $\beta_{|k-i|,|l-j|}$, assuming a stationary and symmetric property. The β matrix provides two pieces of information: one is the neighborhood area of (i, j) , which is a $(2M + 1) \times (2M + 1)$ square. This implies that the permittivity at (i, j) only depends on the permittivity in this neighborhood area. Another piece of

information is the influence of the neighbors on the point (i, j) , as represented by the sign and value of the interaction coefficients. The β matrix is also an equivalence to the neighborhood system \mathcal{N} in the GMRF. Using conventional notation, \mathcal{N} in this model is composed of one-site and two-site cliques of M -th order. A clique is a set of points that are neighbors of one another.

Eq. 16 only defines the conditional distribution of tissue permittivity. According to the Hammersley-Clifford theorem, Eq. 16 is equivalent to the joint distribution of a Gaussian Field[25], expressed as

$$p(X) = \frac{|Q|^{1/2}}{(2\pi)^{N^2/2}} e^{-\frac{(x-\mu)^T Q (x-\mu)}{2}} \quad (18)$$

$$X(k) = \epsilon_r(i, j), k = (i-1) \times N + j, 1 \leq i, j \leq N,$$

where X is a $N^2 \times 1$ vector, an re-ordered mapping of permittivity image ϵ_r defined on an $N \times N$ lattice Ω . The sample space of ϵ_r is R^{N^2} . μ is the mean vector with size $N^2 \times 1$. Q is the inverse covariance matrix with size $N^2 \times N^2$. Q should be symmetric and positive definite.

To describe the equivalence, the relationship of the parameters in Eq. 16 and those in Eq. 18 are summarized.

Eq. 18	Eq. 16
$\mu(k)$	$\mu_{ij},$
	$k = (i-1) \times N + j$
$Q = \Pi B \Pi$	
$\Pi(k1, k2)$	$\begin{cases} \frac{1}{\sigma_{ij}}, & k1 = k2 = (i-1) \times N + j \\ 0, & k1 \neq k2 \end{cases}$
$B(k1, k2)$	$\begin{cases} \beta_{(ij),(kl)}, & (kl) \in \mathcal{N}_{ij} \\ 0, & (kl) \notin \mathcal{N}_{ij} \\ k1 = (i-1) \times N + j \\ k2 = (k-1) \times N + l. \end{cases}$

(19)

When the random field is assumed stationary and isotropic, Π is simplified to $\frac{1}{\sigma} I$, and B is a Toeplitz block circulant matrix.

B. Models of normal and malignant tissue permittivity image

Typically in many studies, malignant and normal tissues have been modeled as homogeneous. Here, we model inhomogeneous tissue characteristics by using means, variances and interaction coefficients to designate both the normal tissue and the malignant tumor. The mean values of tumor and background are μ_t and μ_b respectively, which are scalar variables. The interaction coefficients of tumor and background are matrix β_t and β_b respectively with assumed correlation length. An algorithm proposed by Rue[26] is used to fit the interaction coefficients to the Gaussian field with proposed correlation length.

Transferring the local characteristics to the global characteristics for our Bayesian signal detection approaches, we have a uniform mean vector $\mu^{H_0} = \{\mu_{b_i} : i \in \Omega\}$ for H_0 condition, and a non-uniform mean vector $\mu^{H_1} = (\mu_t - \mu_b) \times V + \mu^{H_0}$ for H_1 condition. V is the tumor mean

function used to describe the position S , the shape and the area A of the tumor. We consider both sharp and smooth tumor mean functions. The sharp tumor mean function is given by

$$\begin{aligned} V(r) &= 1, r \in A(S) \\ V(r) &= 0, r \notin A(S) \end{aligned} \quad (20)$$

The smooth tumor mean function is given by

$$\begin{aligned} V(r) &= \frac{4.0}{D^4}(r-S)^4 - \frac{4.2}{D^2}(r-S)^2 + 1, r \in A(S) \\ D &= n/0.6041, \\ V(r) &= 0, r \notin A(S) \end{aligned} \quad (21)$$

where S is the tumor position, at the center of A . n is a constant. Both the sharp and smooth function are assumptions since real data of tumor spatial distributions is not available yet. The data in [5] suggests a sharp mean function, i.e. permittivity at the tumor boundary that is higher than that at the tumor center.

From the local characteristics β_b and variance σ^2 , we derive the inverse covariance matrix Q^{H_0} under H_0 condition,

$$\begin{aligned} Q^{H_0}((ij), (kl)) &= \beta_{b(ij),(kl)}, (kl) \in \mathcal{N}_{ij} \\ &= 0, (kl) \notin \mathcal{N}_{ij} \end{aligned} \quad (22)$$

Under H_1 condition, the inverse covariance matrix Q^{H_1} , is derived from both β_b and β_t , as well as σ^2 , which is a function of tumor position S .

$$\begin{aligned} Q^{H_1}((ij), (kl)) &= \beta_{t(ij),(kl)}, ((ij) \in A) \& ((kl) \in \mathcal{N}_{ij}) \\ &= \beta_{b(ij),(kl)}, ((ij) \notin A) \& ((kl) \in \mathcal{N}_{ij}) \\ &= 0, (kl) \notin \mathcal{N}_{ij} \end{aligned} \quad (23)$$

In summary, for the benign tissue, the H_0 condition, the distribution of ϵ_r can be expressed as $\epsilon_r \sim N(\mu^{H_0}, Q^{H_0})$. For the malignant tissue, the H_1 condition, the distribution of ϵ_r can be expressed as $\epsilon_r \sim N(\mu^{H_1}, Q^{H_1})$. In the following section, we suppress the superscript H_1 and H_0 if it does not cause any ambiguity. N denotes a multivariate real Gaussian distribution.

The possible parameter space is limited in order to have a definite positive covariance matrix of the Gaussian Markov Random field[27]. However, we still have flexible choices for the β 's, σ 's and μ 's in order to capture the tissue variance in individuals as well as the background structure variance across patients. The model is simple so that computational costs are tractable. Since the Gaussian field is a class of Gibbs distribution (Gibbs [28][23]), it is possible to extend the GMRF to a wide range of Gibbs distributions to model more complex microwave tissue characteristics.

IV. OPTIMAL DETECTION AND LOCALIZATION FRAMEWORK

According to signal detection theory, the optimal detector for doubly composite hypotheses is the likelihood ratio (λ) of the data vector X followed by a threshold whose value is determined by the optimum criterion (T. G. Birdsall).

$$\lambda(X) = \frac{p(X | H_1)}{p(X | H_0)} \quad (24)$$

The optimal localization processor computes the *a posteriori* probability of the tumor location, given the data vector r given the condition H_1 . Frequently we use the maximum *a posteriori* probability of the tumor position in order to obtain quantitative localization performance in terms of the probability of correct localization (PCL).

$$S = \max_{S \in \Omega} p(S|X) \quad (25)$$

Based on signal detection theory, we obtain the optimal physics(tissue)-based Bayesian image processor using two kinds of data: the data of the defining tissue permittivity image as well as the data of the scattered EM field measurements. The Bayesian results are presented in the form of the likelihood ratio and *a posteriori* probability images. We also present non-Bayesian approaches for comparisons. For all these approaches, we assume in this paper that tumor position is a random variable with uniform distribution on the 2D lattice.

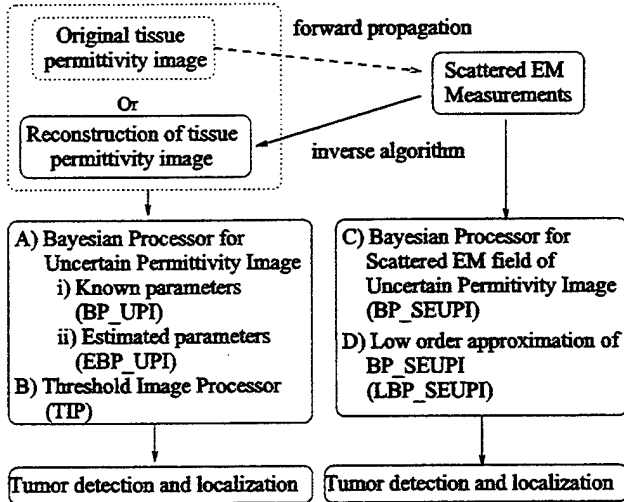


Fig. 2. Signal detection and localization using uncertain tissue permittivity models and EM scattered measurements

Figure 2 shows a flow graph of the various comparisons. The left part in figure 2 illustrates the first Bayesian approach for tumor detection and localization, in which the reconstructed image is optimally post-processed. The Bayesian Processor is derived using the mean, variance and interaction coefficients of the tissue permittivity image, and its output is called the Bayesian Processor for Uncertain Permittivity Image(BP_UPI). It is assumed that the reconstruction is a perfect inverse function of the forward propagation, i.e. we can use the GMRF model presented in section III for both original and reconstructed permittivity image.

The performance upper bounds are obtained based on the BP_UPI algorithm since this optimally process the original permittivity image data, with its prescribed uncertainties. If accurate *a priori* knowledge of the GMRF is not available, a suboptimal approach could use the estimated

parameters. We call the output for such a case the Estimated Bayesian Processor for Uncertain Permittivity Image, EBP_UPI. One of the performance lower bounds is obtained by defining the Threshold Image Processor(TIP) of the reconstructed tissue permittivity image, which is perhaps similar to what a human observer might do in looking at such an image.

A second approach is presented in the right part of Figure 2. Here, the likelihood ratio and *a posteriori* probabilities are formed directly from the measurement data, incorporating the *a priori* knowledge of the uncertainties of the original tissue characteristics as projected through the nonlinear propagation. The output of this processor is called the Bayesian Processor for Scattered EM field of Uncertain Permittivity Image(BP_SEUPI). The Monte Carlo Integration is used to make the computation of BP_SEUPI tractable. Since the scale of the uncertainty is very large, the Monte Carlo Integration, although useful, takes a long time to converge. To reduce the computational complexity, we propose a lower order approximation of the BP_SEUPI, called the LBP_SEUPI. It is based on projecting the uncertainties from the measurement domain onto a multivariate Gaussian field.

A. Bayesian Processor for Uncertain Permittivity Image

A.1 BP_UPI detector

In the problem of unknown tumor position S , the likelihood ratio is

$$\lambda(\epsilon_r) = \frac{\sum_{S \in \Omega} p(\epsilon_r | H_1, S) p(S)}{p(\epsilon_r | H_0)} \quad (26)$$

The *a priori* pdf of the permittivity image has been modeled

$$\begin{aligned} p(\epsilon_r | H_1, S) &\sim N(\mu_S, Q_S) \\ p(\epsilon_r | H_0) &\sim N(\mu, Q) \end{aligned} \quad (27)$$

The likelihood ratio for the BP_UPI

$$\lambda(\epsilon_r) \propto \sum_{S \in \Omega} |Q_S| e^{\frac{(\epsilon_r - \mu)^T Q(\epsilon_r - \mu) - (\epsilon_r - \mu_S)^T Q_S(\epsilon_r - \mu_S)}{2}} \quad (28)$$

A.2 BP_UPI localization processor

The *a posteriori* probability of the tissue permittivity, ϵ_r , given that the tumor is present is expressed as

$$p_{S|\epsilon_r}(S | \epsilon_r) = \frac{p(\epsilon_r | H_1, S) p(S)}{\sum_{S \in \Omega} p(\epsilon_r | H_1, S) p(S)} \quad (29)$$

Using $p(\epsilon_r | H_1, S) \sim N(\mu_S, Q_S)$ and substituting this information into Eq. 28 and simplifying, we obtain

$$p(S | \epsilon_r) \propto (\epsilon_r - \mu)^T Q(\epsilon_r - \mu) + \log(|Q_S|) - (\epsilon_r - \mu_S)^T Q_S(\epsilon_r - \mu_S) \quad (30)$$

With some careful simplifications, the computations will be proportional to the tumor area A .

B. Threshold Image Processor

The Threshold Image Processor (TIP) mimics a routine visual examination of the maximum brightness of the object image.

B.1 TIP detector

The threshold detector is defined by

$$\lambda = \max \epsilon_r \quad (31)$$

where ϵ_r is the permittivity image data.

B.2 TIP localization processor

The threshold localization processor is defined by

$$S = \max_{S \in \Omega} \epsilon_r(S), \quad (32)$$

where S is the tumor position.

C. Bayesian Processor for Scattered EM field of Uncertain Permittivity Image

C.1 BP_SEMUIPI detector

In the measurement domain, The likelihood ratio is defined by

$$\lambda(r) = \frac{\sum_{S \in \Omega} \int_{\epsilon_r} p(r|H_1, \epsilon_r, S) p(\epsilon_r|H_1, S) p(S) d\epsilon_r}{\int_{\epsilon_r} p(r|\epsilon_r, H_0) p(\epsilon_r|H_0) d\epsilon_r}, \quad (33)$$

where S is the unknown tumor position.

Incorporating the *a priori* knowledge of the additive noise, $n \sim \text{calN}(0, 2\sigma_n^2 I)$, the conditional probability density function of r given $T(\epsilon_r | C)$ is

$$p(r | T(\epsilon_r), C) = (2\pi\sigma_n^2)^{-K^2} e^{-\frac{(r-T(\epsilon_r|C))^H (r-T(\epsilon_r|C))}{2\sigma_n^2}} \quad (34)$$

where T is the mapping function from the permittivity image to the measurement data and $T(\epsilon_r)$ is the pure measurement signal.

The complete likelihood ratio is given by

$$\lambda(r) \propto \frac{\sum_{S \in \Omega} \int_{\epsilon_r} e^{-\frac{(r-T(\epsilon_r))^H (r-T(\epsilon_r))}{2\sigma_n^2}} p(\epsilon_r | H_1, S) d\epsilon_r}{\int_{\epsilon_r} e^{-\frac{(r-T(\epsilon_r))^H (r-T(\epsilon_r))}{2\sigma_n^2}} p(\epsilon_r | H_0) d\epsilon_r}. \quad (35)$$

Because $T(\epsilon_r)$ is a complex nonlinear function, we can not obtain a closed form for the likelihood ratio. However, Monte Carlo Integration can be used to compute $\lambda(r)$ in a computationally efficient manner. This can be expressed as

$$\lambda(r) \propto \frac{\sum_{j=1}^M \sum_{S_j \in \Omega} \sum_{i=1}^L \epsilon_{r,i,j} \sim p(\epsilon_r|S_j) e^{-\frac{(r-T(\epsilon_{r,i,j}|S_j))^H (r-T(\epsilon_{r,i,j}|S_j))}{2\sigma_n^2}}}{\sum_{\epsilon_{r,k} \sim p(\epsilon_r|H_0)} e^{-\frac{(r-T(\epsilon_{r,k}|H_0))^H (r-T(\epsilon_{r,k}|H_0))}{2\sigma_n^2}}} \quad (36)$$

where M is the number of all possible tumor positions and L is a number large enough to make the Monte Carlo Integration a good approximation to the likelihood ratio.

C.2 BP_SEMUIPI localization processor

In the measurement domain, we derive the *a posteriori* probability of the tumor position S given the received measurements r .

$$p(S|r) = \int_{\epsilon_r} p(r|\epsilon_r, S) p(\epsilon_r|S) d\epsilon_r \quad (37)$$

Substituting Eq. 34 into Eq. 37, we obtain

$$p(S|r) \propto \int_{\epsilon_r} e^{-\frac{(r-T(\epsilon_r))^H (r-T(\epsilon_r))}{2\sigma_n^2}} p(\epsilon_r|H_1, S) d\epsilon_r. \quad (38)$$

Monte Carlo integration can be used to make the computation tractable

$$p(S|r) \propto \sum_{k=1}^L e^{-\frac{(r-T(\epsilon_{r,k}))^H (r-T(\epsilon_{r,k}))}{2\sigma_n^2}}, \quad (39)$$

where $\epsilon_{r,k}(S)$ follows the distribution $N(\mu_S, Q_S)$, given S . L is a number large enough to make the Monte Carlo converge to a good approximation of the *a posteriori* probability.

D. Lower order approximation of BP_SEMUIPI

Considering the huge time cost for computing BP_SEMUIPI, a lower order distribution is considered to approximate the true distribution of the measurement data, and the resultant processor is called LBP_SEMUIPI. The multivariate Gaussian model is chosen which demonstrates good performance in the simulations. From a generated large database, we estimate the mean and covariance matrix of the measurement data under both H_0 and H_1 , which are M and D for H_0 and M_S and D_S for (H_1, S) . The size of the M_S and D_S matrices are the same as the size of the possible tumor positions. These estimates are then used in the LBP_SEMUIPI processors to make detection and localization decisions.

D.1 LBP_SEMUIPI detector

Using a multivariate complex Gaussian model, we have

$$p(T_{\epsilon_r} | C) = \frac{|D_C|}{(2\pi)^{K^2}} e^{-(T_{\epsilon_r} - M_C)^H D_C (T_{\epsilon_r} - M_C)}, \quad (40)$$

where subscript C represents (H_0) or (H_1, S) . K is the number of sensors.

Using the theorem of Multiplication,

$$p(r | C) = \int_{\epsilon_r \in} p(r | T_{\epsilon_r}|C) p(T_{\epsilon_r}|C) dT_{\epsilon_r}. \quad (41)$$

Substituting Eq. 40 and Eq. 34 into Eq. 41, we obtain

$$\begin{aligned} p(r | C) &= \frac{|D_C| |D_{C1}|^{-1}}{(2\pi\sigma_n^2)^{K^2}} e^{M_{C1}^H D_{C1} M_{C1} - \frac{r^H r}{2\sigma_n^2} - M_C^H D_C M_C}, \\ D_{C1} &= \frac{I}{2\sigma_n^2} + D_C, \\ M_{C1} &= D_{C1}^{-1} \left(\frac{r}{2\sigma_n^2} + D_C M_C \right). \end{aligned} \quad (42)$$

The likelihood ratio can be expressed as

$$\lambda(r) = \frac{\sum_{S \in \Omega} p(r | H_1, S) p(S)}{p(r | H_0)} \quad (43)$$

where M is the number of all possible tumor positions.

Substituting Eq. 42 into Eq. 43, with C replaced by (H_1, S) and (H_0) respectively, we obtain the simplified form of the LBP_SEMUIPI detector

$$\lambda(r) \propto \sum_{S \in \Omega} |D_S| |D_{S1}|^{-1} e^{M_{S1}^H D_{S1} M_{S1} - M_S^H D_S M_S - M_1^H D_1 M_1} \quad (44)$$

where, M_{S1} , D_{S1} , M_1 and D_1 follow Eq. 42.

When σ_n^2 approaches zero, i.e. there is no measurement error, the expressions are simplified to

$$p(r | C) = \frac{|D_C|}{(2\pi)^{K^2}} e^{-(r-M_C)^H D_C (r-M_C)},$$

$$\lambda(r) \propto \sum_{S \in \Omega} |D_S|^{-\frac{1}{2}} e^{(r-M)^H D (r-M) - (r-M_S)^H D_S (r-M_S)} \quad (45)$$

D.2 LBP_SEMUIPI localization processor

The localization problem has already been defined in Eq. 37. With the multivariate Gaussian model approximation, the conditional probability density function of r given H_1 and S is defined in Eq. 42, with C replaced by (H_1, S) . Then the *a posteriori* probability expression is given by

$$p(S | r) \propto \frac{|D_S| |D_{S1}|^{-1}}{(2\pi\sigma_n^2)^{K^2}} e^{M_{S1}^H D_{S1} M_{S1} - \frac{r^H r}{2\sigma_n^2} - M_S^H D_S M_S},$$

$$D_{S1} = \frac{I}{2\sigma_n^2} + D_S, \quad (46)$$

$$M_{S1} = D_{S1} \left(\frac{r}{2\sigma_n^2} + D_S M_S \right).$$

When there is no additive noise, the LBP_SEMUIPI localization processor is simplified to

$$p(S | r) \propto \log(|D_S|) - (r - M_S)^H D_S (r - M_S). \quad (47)$$

V. SIMULATION RESULTS

A. Basic parameters

In the simulations in this paper, the tissue permittivity image has size 9.2cm \times 9.2cm, 529 pixels and the unit area is 4mm \times 4mm. For the first three simulation scenarios, there are 24 sensors evenly spaced outside the object area, 7 at each side and 1.6cm between the neighborhood sensors. The frequency used for propagation and reconstruction is 1GHz. The last simulation scenario discusses the effect of different array configurations.

The mean value of normal background tissue was set to $\mu_b = 30$, which is within the range of values reported experimentally for real breast permittivity [6]. The mean value of malignant tumor μ_t is considered to be a variable in the first simulation in order to study the effect of the tumor contrast, and it takes constant value of 40 in the later simulations. The variance for both the background and the tumor is 1. The interaction coefficients of tumor

and background are β_t and β_b to fit the Gaussian field with 3 and 30 pixel correlation lengths.

$$\beta_b = \begin{bmatrix} 1.0000 & -0.1879 & 0.0191 \\ -0.1879 & -0.1724 & 0.0453 \\ 0.0191 & 0.0453 & 0.0007 \end{bmatrix} \quad \beta_t = \begin{bmatrix} 1 & 0.1 \\ 0.1 & 0.1 \end{bmatrix} \quad (48)$$

We also consider the situation where both tumor and normal tissue have the same interaction coefficient β_b in the first simulation scenario. Two tumor types, one with sharp boundaries and the other with smooth boundaries mean are used in the first scenario, as shown in figure 3a 4a.

B. Performance evaluation

To evaluate the detection performance, we use the Receiver Operating Characteristic (ROC), which is a plot of the Probability of Detection (P_D) as a function of Probability of False alarm (P_F). P_D and P_F are obtained from the probability density functions of the likelihood ratio λ under each hypothesis in that

$$P_D = \int_{\beta}^{\infty} p(\lambda | H_1) d\lambda \quad P_F = \int_{\beta}^{\infty} p(\lambda | H_0) d\lambda \quad (49)$$

We also use the detectability index, d , sometimes called the deflection coefficient, to evaluate the detection performance. The scalar variable d completely characterizes the ROC for the case where the underlying probability density functions are Gaussian. In other cases, d can be estimated from the ROC curve through Eq. 50 using a data fitting method and used as an approximation to the ROC's.

$$P_D = 1 - \text{Gau2cdf}(\text{Gau2inv}(1 - P_F) - d) \quad (50)$$

where Gau2cdf and Gau2inv are normalized Gaussian cumulative density function (CDF) and inverse CDF functions.

To evaluate the localization performance, we use Probability of Correct Localization (PCL). PCL is the ratio of the number of correct localization divided by the total number of trials.

A database of the original and reconstructed tissue permittivity image and measurement data is generated for the performance evaluation, including 400 realizations with a tumor at random positions and 400 realizations with no tumor. The test database is independent of a large database generated to study the statistics of the measurement data.

C. Performance upper bound and tumor characteristics

The detection performances of BP_UPI are shown in figures 3b 3c, 4b, and 4c. In those figures the detectability is plotted as a function of tumor area, tumor contrast $\frac{\mu_{H1} - \mu_{H0}}{\sigma}$, sharp or smooth tumor mean function, and whether or not the interaction coefficients for malignant and background tissue are the same or different. The computation follows Eq. 28.

The localization performances are shown by PCL curves in figures 3d, 3e, 4d, and 4e. That computation follows Eq. 30.

The simulation results demonstrate that

1. The tumor detection and localization performance increases with the tumor contrast $\frac{\mu^{H1} - \mu^{H0}}{\sigma}$, which is shown in all 8 plots.

2. By comparing figure 3 and figure 4, it can be seen that it is easier to detect and locate the tumor with a sharp weight function than that with a smooth weight function.

3. By comparing (b) and (c), (d) and (e) in both figures 3 and 4, one can see that capturing different interaction coefficients for the background and the tumor will help to improve the detection and localization performance.

4. The performance as a function of tumor area is not a simple scaling relationship as that of tumor contrast since it is influenced by the tumor mean function and the interaction coefficients together. When the tumor and the background have the same interaction coefficients and the tumor has a smooth shape function, the larger tumor area may cause stronger similarity between the tumor and the background such that the detection performance may decrease, as shown in 4c,e).

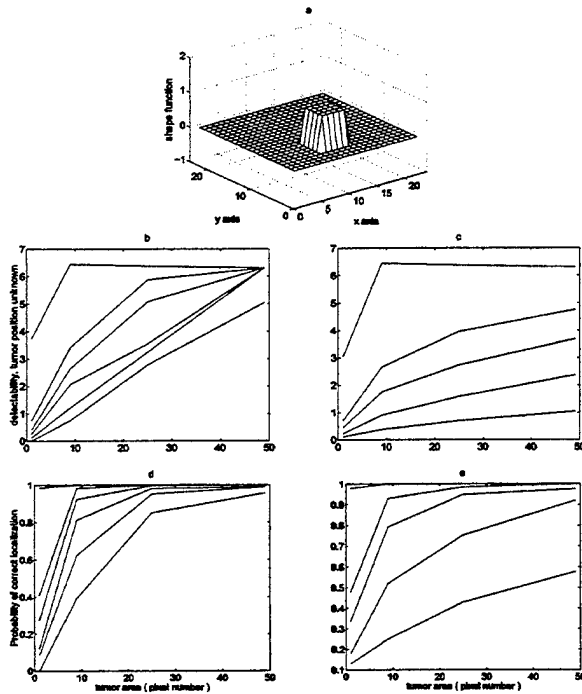


Fig. 3. Detection and localization performance of BP.UPI using original tissue permittivity image as a function of tumor contrast, size, local characteristics, with sharp tumor mean function. a) an example of sharp tumor mean function, tumor at (11,7), occupying 25 pixels. b)c)ROC, d)e)PCL curves. Interaction coefficients for background and tumor: left-differ, right-same. From top to bottom, contrast $\frac{\mu^{H1} - \mu^{H0}}{\sigma}$: Left-[5 2.5 2 1.5 1 0], Right-[5 2.5 2 1.5 1]

D. Convergence of the covariance matrix estimation

The estimation of the mean and covariance matrix is an important part for the performance of the computationally simpler EBP.UPI and LBP.SEMUPI. Since the uncertainty scale is large, we need a large number of samples for the estimates to converge.

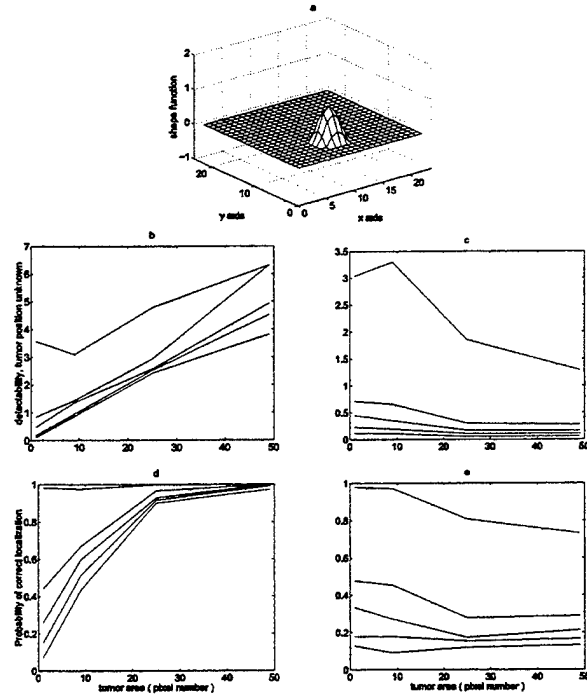


Fig. 4. Detection and localization performance of BP.UPI using original tissue permittivity image as a function of tumor contrast, size, local characteristics, with smooth tumor mean function. a) an example of smooth tumor mean function, tumor at (11,7), occupying 25 pixels. b)c)ROC, d)e)PCL curves. Interaction coefficients for background and tumor: left-differ, right-same. From top to bottom, contrast $\frac{\mu^{H1} - \mu^{H0}}{\sigma}$: Left-[5 2.5 2 1.5 1 0], Right-[5 2.5 2 1.5 1]

Two approaches are used to study the convergence of the estimates,

1. Determine the performance of the processor versus the number of samples used to form the estimates. The ROC curve should reach some stable state as the number of the samples increases.

2. Estimate the mean and covariance matrix of the original tissue permittivity image data from the database, and compare them with the true values. The difference should be within a small threshold. The number of unknowns is 529 for the tissue permittivity image and 600 for the measurement data. Since they are comparable, we can use the convergence of estimates using the image data to predict that using the measurement data.

Figure 5 illustrates the detection performance of the BP.UPI and LBP.SEMUPI detectors versus the number of samples used in the estimations of mean vector and covariance matrix. Figure 5a uses the original permittivity image data and it can be seen that the ROC curves become stable near the perfect upper left corner. The corresponding deflection coefficient converges to around 6.4 after 1400 samples. It should be noted that 6.4 is the upper limit of the deflection coefficient that we can estimate using the data fitting method. Figure 5b uses the scattered EM measurement data. The ROC curves converge with some degradation compared with those using the original permittivity image data. The corresponding deflection coefficient

converges to around 3.6 after 1400 samples. The performance degradation as sample size decreases also reflects the effect of non-accurate *a priori* knowledge of the mean and covariance matrix on the processor's performance.

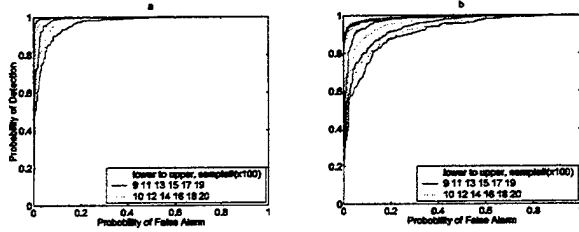


Fig. 5. The convergence of the detection performance as a function of the number of samples used to estimate the mean and covariance matrix. Assume the tumor position unknown. a) ROC curves of BP_UPI detector using the original tissue permittivity image data b) ROC curves of LBP_SEMUPI detector using the measurement data

Table I lists the value of the estimated coefficients from 2000 samples and the true values using the original tissue permittivity image data. There are 35%-50% increases in the absolute estimation values. However, the performance curves demonstrate that this level of accuracy in interaction coefficients is OK for a stable performance.

TABLE I
THE TRUE AND THE ESTIMATED INTERACTION COEFFICIENTS

	β_{b11}	β_{b12}	β_{b13}	β_{b22}
ture	1	-0.1879	0.0191	-0.1724
estimate	1.3557	-0.2547	0.0255	-0.2337
	β_{b23}	β_{b33}	β_{t11}	$\beta_{t12,22}$
ture	0.0453	0.00067	1	0.1
estimate	0.0607	0.0007	1.3613	0.1459

E. Performance of proposed Bayesian approaches

E.1 An example

Figure 6a is an example of a stochastic background permittivity image of the tissue, along with a simulated tumor, modeled by the GMRF. Figures 6b, c, and d are the reconstructed permittivity images from the perfect measurement data or from 60dB and 50dB noisy measurement data.

The signal detection approach using the permittivity data is to compute the *a posteriori* probability of the tumor location given either the original permittivity image, or the reconstructed image as data, with Eq. 30. Figure 6e gives an upper bound on tumor localization by plotting the *a posteriori* probability of tumor location using the tissue data of Figure 6a. Figure 6i gives a sub-optimal performance comparison for tumor localization by plotting the *a posteriori* probability of tumor location using the tissue data of Figure 6a and the estimation of the mean and covariance matrix. Figures 6f-h shows the *a posteriori* plot of tumor location based on post processing the reconstructed tissue data shown in Figures 6b-d.

Using the measurement data, the *a posteriori* probability of tumor location is computed with Eq. 46. Figure 6j-l shows the *a posteriori* plot of tumor location base on the same measurements to get the reconstruction in figures 6b-d.

Plots 6g-h show that at 60dB and 50dB additive noise condition, the BP_UPI using the reconstruction tissue data misses the correct tumor localization, and figures 6k-l show that the BP_SEMUPI using the measurement data gets the correct location of the tumor with high probability. This is a specific example where the BP_SEMUPI works better. In the following sections, it is demonstrated statistically that the processors based directly on the likelihood ratio and *a posteriori* probabilities of the measurement data have better performance.

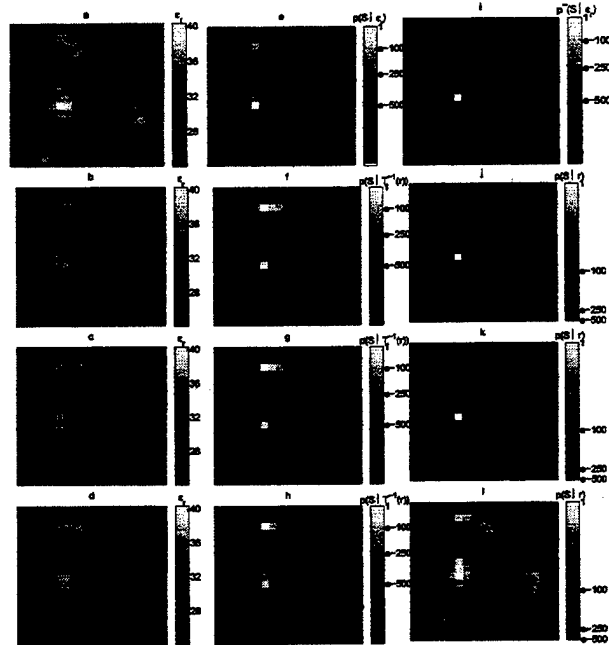


Fig. 6. a) Original tissue permittivity image; b)-d) Reconstructed permittivity from the measurement data b) without additive noise c) with additive noise, SNR=60dB d) with additive noise, SNR=50dB; e)-h) the *a posteriori* probability of the tumor position given the permittivity image data and H1 condition- $p(S | \epsilon_r, H1)$, data ϵ_r comes from a)-d); i) the $p(S | \epsilon_r, H1)$ computed using the estimation of the mean and covariance matrix and the data from a); j)-l) the *a posteriori* probability of the tumor position given the measurement data and H1 condition- $p(S | r, H1)$

E.2 Detection performance

Figure 7 illustrates detection performance comparisons assuming no additive noise. In figure 7 the ROC of the threshold detector provides a performance lower bound. TIP mimics the way a routine visual examination of the image might be done. Although it is not sophisticated, it's ROC reflects the problem of high positive predictive Value (PPV) of conventional mammography. Using the reconstructed permittivity image data, the BP_UPI detector is much better than the TIP detector, especially when the probability of false alarm is low, because the BP_UPI uti-

lizes the *a priori* knowledge of the tissue background across patients and the *a priori* knowledge of the different characteristics of the normal and malignant tissues to improve the detection performance. With a shared large database, accurate *a priori* knowledge will be available. Even with uncertain *a priori* knowledge, as shown in figure 5, the performance is still satisfactory compared with that of the threshold method.

Figure 7 also shows that the BP_SEMUIPI detector using the measurement data is better than BP_UIPI detector using the reconstructed permittivity data, yet worse than BP_UIPI detector using the original permittivity data. It should be noted that in reality, we can not get the original tissue permittivity image directly but the scattered EM measurements. However, it provides an upper bound for performance evaluations. It is better than the BP_SEMUIPI because the forward EM field maps the variables from the original permittivity domain to the measurement domain, which reduces the random variable space and decreases the detectability. Proofs in the Appendix support this explanation. In addition, it is because of the multivariate Gaussian approximation used to compute Eq. 37. The LBP_SEMUIPI is better than the BP_UIPI using reconstructed permittivity data because of the inherent algorithm limitations in the reconstruction procedure.

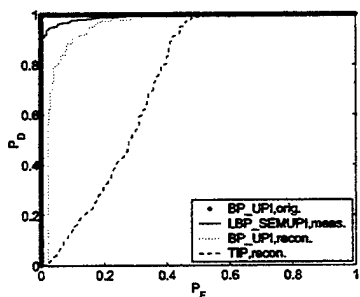


Fig. 7. Detection performance of BP_UIPI using original tissue data, BP_UIPI using reconstructed permittivity image data, TIP using reconstructed permittivity image data and BP_SEMUIPI using measurement data. No additive noise presents at sensors, tumor position unknown

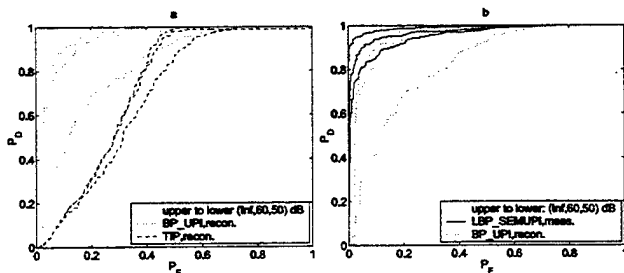


Fig. 8. Detection performance comparisons. Tumor position unknown. SNR=[inf, 60, 50]dB a) BP_UIPI and TIP detectors using the reconstructed tissue permittivity image b) BP_UIPI detector using the reconstructed tissue permittivity image and LBP_SEMUIPI detector using the measurement data

Figure 8 displays the performance of the detectors when

noise is present. Additive noise degrades the performance of all three detectors. Figure 8a shows that for the three SNR conditions, the BP_UIPI detector is better than the TIP detector. The ROC curve at 60dB SNR condition is so close to the ROC curve for a very large SNR that we consider 60dB as a threshold for the BP_UIPI detector using reconstruction data. Figure 8b) shows that for the three SNR conditions, the LBP_SEMUIPI detector using the measurement data is better than the BP_UIPI detector using the reconstructed tissue permittivity image data.

E.3 Localization performance

Figure 9 displays the localization performance of the LBP_SEMUIPI using the measurement data, and the BP_UIPI and the TIP using the reconstructed tissue permittivity data. The localization performance is shown by

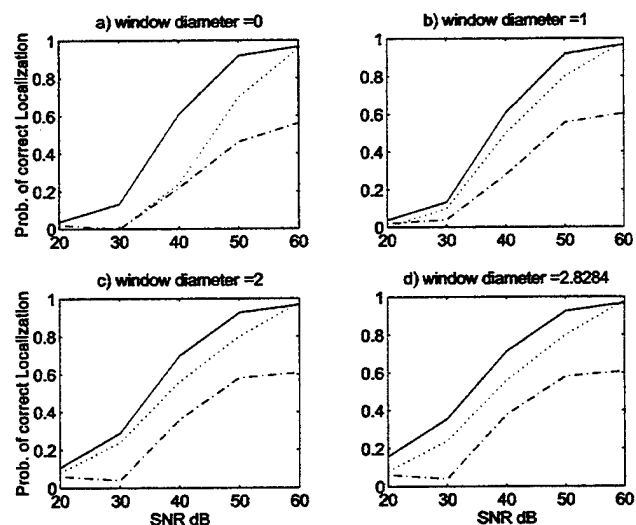


Fig. 9. Localization performance: solid line, LBP_SEMUIPI using the measurement data; dotted line, BP_UIPI using the reconstructed tissue permittivity data; dashed line, TIP using the reconstructed tissue permittivity data

the probability of correct localization (PCL) curves. The localization is correct if the picked position is located within the test window. If it is required that the picked position is exactly the same as the real position to be true, the window diameter is zero. For the other values of the window diameter: 1, 2, 2.8284, the window sizes are 9, 13, 25. Figure 9 demonstrates that at 50dB or 60dB SNR, both the BP_UIPI and the LBP_SEMUIPI have performance better than 0.9 PCL. They are much better than the threshold method for all the tested SNR conditions. The LBP_SEMUIPI localization using the measurement data is the best of the three. The results of the detection and localization performances show that the LBP_SEMUIPI, which processes the measurement data directly, provides a potential way to help a doctor make a better diagnosis.

F. Performance and Array configurations

This simulation scenario studies the detection performance as a function of the sensor array configuration. Fig-

ure 10 displays the deflection coefficient indexed by 2D source positions, given the possible tumor position is known to the detectors.

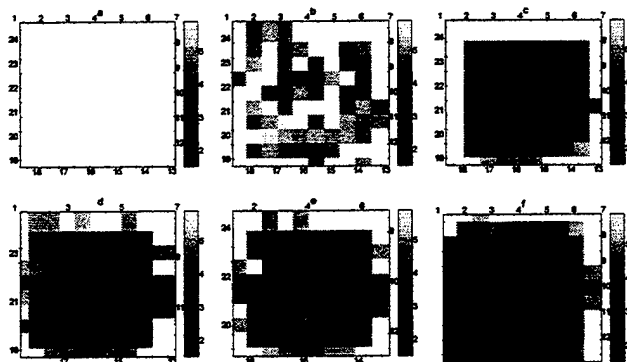


Fig. 10. Deflection coefficients as a function of the tumor positions, assume tumor position known for the detector. a) BP_UPI using original permittivity data b) EBP_UPI using original permittivity data c-f) LBP_SEMUI using measurement data. c) Configuration 1:1:24, 24 sensors work d) Configuration 1:2:24, 12 sensors work e) Configuration 2:2:24, 12 sensor work f) Configuration 1:1:12, 12 sensors work

Figure 10a provides the upper bound by computing the deflection coefficient of the BP_UPI using the original permittivity data. Figure 10b is a sub-optimal comparison by computing the deflection coefficient of EBP_UPI using the original permittivity data. The degradation in figure 10b compared with that in figure 10a reflects the effect of the estimation procedure, which is independent of the tumor positions. Figures 10c- 10f is the performance of the LBP_SEMUI detector for four different array configurations. The four plots show a strong relationship between the detection performance and the distance of the tumor to the sensors. The deeper the tumor is located, the more difficult it is to detect.

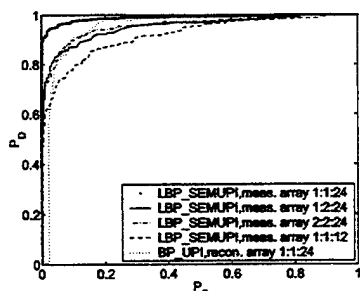


Fig. 11. Detection performance using the measurement data and the reconstructed permittivity image data. Assume tumor position unknown. Comparison of different array configurations.

Figure 11 displays the ROC detection performance when the possible tumor position is unknown. By comparing the ROC curves of the first configurations with the three other configurations in figure 11, one sees that the performance degrades due to the limited number of sensors. The ratio of the data length to the uncertainty variable number is 600:529 for the first configuration and 156:529 for three other configurations. On the other hand, if we lower the

requirement on the processor's performance, we can reduce the necessary number of sensors. The plots also show how the configuration of sensors will influence the processor's performance. For the case where the tumor position follows a uniform *a priori* distribution, it appears that the more evenly spaced the sensors, the better the performance. But if the *a priori* tumor position is not a uniform distribution, we could improve the performance by having more sensors close to the possible tumor positions.

VI. CONCLUSION

This paper considers two Bayesian approaches for breast tumor diagnosis, one post processes the reconstructed tissue permittivity image data. The other incorporates the scattered EM measurement data into an optimal likelihood ratio detector. The breast permittivity cross section propagation medium is modeled by a Gaussian Markov Random Field. The simulations compare these two approaches. The simulation results also provide an upper bound on early detection performance and localization of malignant tissue, as a function of uncertain and variable tissue permittivity characteristics, tumor contrast, tumor size, and local characteristics and shape. The effectiveness of using the multivariate Gaussian distribution approximation for the measurement data to reduce the computational complexity was also illustrated. Finally, the effect of array configurations on detection performance was illustrated.

ACKNOWLEDGMENTS

This work was supported by the U. S. Army Medical Research Center under contract number DAMD17-01-1-0513.

REFERENCES

- [1] S. S. Chaudhary R. K. Mishra Arvind Swarup and Joy M. Thomas, "Dielectric properties of normal & malignant human breast tissue at radiowave & microwave frequencies," *Indian J. Biochem. Biophys.*, vol. 21, pp. 76-79, Feb. 1984.
- [2] H. Fricke and S. Morse, "The electric capacity of tumors of the breast," *J. Cancer Res.*, vol. 16, pp. 310-376, 1926.
- [3] W. T. Joines and R. L. Jirtle etc, "Microwave power absorption differences between normal and malignant tissue," *Int. J. Radiation Oncology Biol. Phys.*, vol. 6, pp. 681-687, 1980.
- [4] W. T. Joines etc, "The measured electrical properties of normal and malignant human tissues from 50 to 900 mhz," *Medical Physics*, vol. 21, no. 4, pp. 547-550, April 1994.
- [5] A. J. Surowiec and etc S. S. Stuchly, "Dielectric properties of breast carcinoma and the surrounding tissues," *IEEE Trans. Biomed. Eng.*, vol. 35, no. 4, pp. 257-263, 1988.
- [6] Liewei Sha, Erika R. Ward and Brandon Story, "A review of dielectric properties of normal and malignant breast tissue," *IEEE SoutheastCon 2002*, pp. 457-462, Columbia, South Carolina, April 5-7, 2002.
- [7] T. S. England and N. A. Sharples, "Dielectric properties of the human body in the microwave region of the spectrum," *Nature*, vol. 163, pp. 487-488, March 1949.
- [8] T. S. England, "Dielectric properties of the human body for wave-lengths in the 1-10 cm range," *Nature*, vol. 166, pp. 480-481, Sep. 1950.
- [9] J. R. Mallard and D. C. Lawn, "Mammary tumor," *Nature*, vol. 213, pp. 28-30, 1967.
- [10] A. M. Campell and D. V. Land, "Dielectric properties of female human breast tissue measured in vitro at 3.2 ghz," *Phys. Med. Biol.*, vol. 37, no. 1, pp. 193-210, 1992.
- [11] P. M. Meaney and K. D. Paulsen etc, "A clinical prototype for active microwave imaging of the breast," *IEEE Transactions on Microwave Theory and Techniques*, vol. 48, no. 11, pp. 1841-1853, Nov. 2000.

- [12] Q. H. Liu, Z. Q. Zhang, T. Wang, G. Ybarra, L. W. Nolte, J. A. Bryan, W. T. Joines, "Active microwave imaging I: 2-D forward and inverse scattering methods," *IEEE Trans. Microwave Theory Tech.*, vol. 50, no. 1, pp. 123-133, Jan 2002.
- [13] Z. Q. Zhang and Q. H. Liu, "Two nonlinear inverse methods for electromagnetic induction measurements," *Geosci. Remote Sensing*, vol. 39, no. 6, pp. 1331-1339, June 2001.
- [14] S. C. Hagness, A. Taflov, et al., "Three-dimensional fdtd analysis of a pulsed microwave confocal system for breast cancer detection: Design of an antenna-array element," *IEEE Trans. Antennas and Propagation*, vol. 47, pp. 783-791, May 1999.
- [15] D. J. Rossi and A. S. Willsky, "Reconstruction from projections based on detection and estimation of objects-part i and ii: Performance analysis and robustness analysis," *IEEE Trans. on ASSP*, vol. ASSP-32, no. 4, pp. 886-906, August 1984.
- [16] D. Jalilhal and L. W. Nolte, "Signal detection theory and reconstruction algorithms - performance for images in noise," *IEEE Trans. on Biomedical Engineering*, vol. 41, no. 5, pp. 501-504, May 1994.
- [17] H. D. Li, M. Kallergi, et al., "Markov random field for tumor detection in digital mammography," *IEEE Trans. on Medical Imaging*, vol. 14, no. 3, pp. 565, Sep 1995.
- [18] Liewei Sha, Loren W. Nolte, Zhong Qing Zhang, and Qing H. Liu, "Performance analysis for Bayesian microwave imaging in decision aided breast tumor diagnosis," *Proceedings of the 2002 IEEE International Symposium on Biomedical Imaging*, pp. 1039-1042, Washington, DC, July 7-10, 2002.
- [19] Hammersley and Clifford, "Markov field on finite graphs and lattices," *unpublished*, 1974.
- [20] Don H. Johnson and Dan E. Dudgeon, *Array Signal Processing concepts and techniques*, P T R Prentice Hall, Inc., 1993, P478 A.3.
- [21] Z. Q. Zhang and Q. H. Liu, "Reconstruction of axisymmetric media with an fft enhanced extended born approximation," *Inverse Problems*, invited paper, vol. 16, no. 5, pp. 1281-1296, 2000.
- [22] P. M. Berg and R. E. Kleinman, "A contrast source inversion method," *Inverse Problems*, vol. 13, pp. 1607-1620, 1997.
- [23] S. Z. Li, *Markov Random Field Modeling in Computer Vision*, Comp. Sci. Workbench. Springer, 1995.
- [24] R. Chellappa, "Two-dimensional discrete gaussian markov random field models for image processing," *Progress in Pattern Recog.*, vol. 2, pp. 79-112, 1985.
- [25] J. Besag, "Spatial interaction and the statistical analysis of lattice systems," *J. Royal Statistical Society*, vol. B, no. 36, pp. 179, 1974.
- [26] H. Rue and H. Tjelmeland, "Fitting gaussian markov random fields to gaussian fields," *Statistics*, NO.16, 1999.
- [27] S. Lakshmanan and H. Derin, "Valid parameter space for 2-d gaussian markov random field," *IEEE Trans. on Information Theory*, vol. 39, no. 2, pp. 703-709, March 1993.
- [28] S. Geman and D. Geman, "Stochastic relaxation, gibbs distributions and the bayesian restoration of images," *IEEE Trans. on Pattern Analysis and Machine Intelligence*, vol. PAMI-6, no. 6, pp. 721-741, Nov. 1984.
- [29] J.S. Chipman, "On least squares with insufficient observations," *J. Amer. Statist. Assoc.*, vol. 59, pp. 1078-1111, 1964.

APPENDIX: DEFLECTION COEFFICIENT INEQUALITIES

For linear projection and reconstruction medical system, the performance of the optimal detectors to distinguish the tumor of some fixed position from the normal tissue background can be precisely represented by the deflection coefficient if multivariate normal distributions are used to model the object image and the measurement error. In this part, we derive the deflection coefficient based on these assumptions using the original, measurement and reconstruction data, and prove relationships with a matrix inequality theorem. Furthermore, the effects of the forward propagation, the reconstruction procedure and the measurement error on the detection performance are clarified.

Theorem 1: $u^T C^{-1} u \geq u^T B^T (BCB^T)^{-1} B u$, if C is a

$N \times N$ real symmetric positive definite matrix, u is a $N \times 1$ vector, B is a $M \times N$ matrix and BCB^T is non singular.

Proof: We have the matrix version of the well-known Cauchy-Schwarz inequality[29]

$$X^T X \geq_L X^T Y (Y^T Y)^{-1} Y^T X, \quad (51)$$

where, X is a $n \times m$ matrix, Y is a $n \times q$ matrix, and $Y^T Y$ is nonsingular. \geq_L is the Loewner ordering relationship.

As C is a real symmetric positive definite matrix, we have $C = LL^T$ and $C^{-1} = L^{-T} L^{-1}$, where L is a $N \times N$ simple matrix. Substitute $X = L^{-T}$ and $Y = L^T B^T$ into Eq. 51, we get $C^{-1} \geq_L B^T (BCB^T)^{-1} B$, i.e. $u^T C^{-1} u \geq u^T B^T (BCB^T)^{-1} B u$. ■

Deflection Coefficient after linear transformation

Any linear transformation can be represented by a matrix A . Assume x is a $N \times 1$ vector of multivariate Gaussian distribution, y is a $M \times 1$ vector transformed from x by $M \times N$ matrix A

$$y = Ax. \quad (52)$$

Assume the binary hypotheses for x are

$$\begin{aligned} H1: & x \sim N(\theta_1, C) \\ H0: & x \sim N(\theta_0, C), \end{aligned} \quad (53)$$

where θ_i is the $N \times 1$ mean vector; C is the $N \times N$ covariance matrix, which is real, symmetric and positive definite.

From Eq. 52 and Eq. 53, we have

$$\begin{aligned} E\{y | H1\} &= A\theta_1 \\ E\{y | H0\} &= A\theta_0 \\ COV\{y\} &= ACA^T. \end{aligned} \quad (54)$$

We derive the deflection coefficient no matter whether the $COV(y)$ be singular or non-singular. Let $R_A = rank(A)$. There are R_A independent rows in A . We assume A_1 is composed of R_A independent rows of A , and A_2 is composed of the rest of the rows of A . A_2 can be represent by a linear combination of rows in A_1 , i.e. $A_2 = GA_1$. Then, we have

$$\begin{aligned} y &= \begin{bmatrix} y_1 \\ y_2 \end{bmatrix} = \begin{bmatrix} A_1 \\ A_2 \end{bmatrix} x \\ y_1 &= A_1 x \\ y_2 &= A_2 x = GA_1 x = Gy_1. \end{aligned} \quad (55)$$

From Eq. 55, we get $p_y(y) = \delta(y_2 - Gy_1)p_{y_1}(y_1)$. Since y_2 is determined by y_1 , which is independent of the hypotheses, we find that the likelihood ratio of y is the same as the likelihood of y_1 , and so is the deflection coefficient. It can be proved that $COV(y_1) = A_1 C A_1^T$ is a real symmetric positive definite matrix. Then the post-transformation deflection coefficient becomes

$$d^2 = \Delta \theta^T A_1^T (A_1 C A_1^T)^{-1} A_1 \Delta \theta. \quad (56)$$

Deflection coefficients using three kinds of data

1. Original image data

The binary hypotheses have been defined in Eq. 53, where $H1$ represents the normal tissue background with a tumor

present, H_0 represents the normal tissue background only, and x in this problem is the permittivity data ϵ_r used for detection. The deflection coefficient with the original object data becomes

$$\begin{aligned} d_o^2 &= \Delta\theta^T C^{-1} \Delta\theta \\ \Delta\theta^T &= \theta_1 - \theta_0. \end{aligned} \quad (57)$$

2. Measurement data

If we consider the measurement error, and use the additive independent Gaussian vector to represent it, the measurement data r can be represented by

$$\begin{aligned} r &= A\epsilon_r + n = \begin{bmatrix} A & I_M \end{bmatrix} \begin{bmatrix} \epsilon_r \\ n \end{bmatrix} \\ n &\sim N(0, I_M \sigma_n^2), \end{aligned} \quad (58)$$

where A is a $M \times N$ matrix, I_M is a $M \times M$ Identity matrix, ϵ_r is an $N \times 1$ vector, n is a $M \times 1$ vector. Using Eq. 55, 56, with A replaced by $[A \ I_M]$, x replaced by $\begin{bmatrix} \epsilon_r \\ n \end{bmatrix}$, and y replaced by r , we obtain the deflection coefficient using the measurement data

$$d_m^2 = \Delta\theta^T A_1^T (A_1 C A_1^T + I_{M_1} \sigma_n^2)^{-1} A_1 \Delta\theta, \quad (59)$$

where, $[A_1 \ I_{M_1}]$ are composed of R_A independent rows of matrix $[A \ I_M]$, $R_A = \text{rank}([A \ I_M])$.

3. Reconstructed image data

After reconstruction, the estimated object data $\hat{\epsilon}_r$ can be represented by

$$\hat{\epsilon}_r = B r = B \begin{bmatrix} r_1 \\ r_2 \end{bmatrix} = D r_1, \quad D = \begin{bmatrix} B \\ BG \end{bmatrix} \quad (60)$$

where, r_1, r_2 correspond to y_1, y_2 in Eq. 55. G is a matrix that satisfies $r_2 = G r_1$. Using Eq. [55, 56] again, with A replaced by D , x replaced by r_1 and y replaced by $\hat{\epsilon}_r$, we obtain the deflection coefficient of the optimal detector using reconstruction data

$$d_r^2 = \Delta\theta^T (B_1 A_1)^T (B_1 A_1 C (B_1 A_1)^T + B_1 B_1^T \sigma_n^2)^{-1} B_1 A_1 \Delta\theta, \quad (61)$$

where B_1 is composed of R_B independent rows of D , $R_B = \text{rank}(D)$.

Inequality relationships of deflection coefficients

We have $d_o^2 = \Delta\theta^T C^{-1} \Delta\theta$. Assume $\sigma_n^2 = 0$, we have $d_{m_0}^2 = \Delta\theta^T A_1^T (A_1 C A_1^T)^{-1} A_1 \Delta\theta$. Apply theorem 1, we get $d_o^2 \geq d_{m_0}^2$. It can be proved that d_m^2 is inversely proportional to σ_n^2 , or $d_m^2 \leq d_{m_0}^2$, so we get

$$d_o^2 \geq d_m^2. \quad (62)$$

Let $\Delta\Theta = A_1 \Delta\theta$ and $E = A_1 C A_1^T + I_{M_1} \sigma_n^2$, and substitute them into Eq. 59 and Eq. 61, we have

$$\begin{aligned} d_m^2 &= \Delta\Theta^T E^{-1} \Delta\Theta \\ d_r^2 &= \Delta\Theta^T (B_1)^T (B_1 E B_1^T)^{-1} B_1 \Delta\Theta. \end{aligned} \quad (63)$$

Since E is real symmetric positive definite, $B E B^T$ is non singular, apply theorem 1, we get

$$d_m^2 \geq d_r^2. \quad (64)$$

Two special cases

1. Case 1: Assume the measurement error is not present, and the only uncertainties are the normal and malignant tissue properties.

Let $\sigma_n^2 = 0$, from Eq. 59 and Eq. 61, we have

$$\begin{aligned} d_m^2 &= \Delta\theta^T A_1^T (A_1 C A_1^T)^{-1} A_1 \Delta\theta \\ d_r^2 &= \Delta\theta^T (B_1 A_1)^T (B_1 A_1 C (B_1 A_1)^T)^{-1} B_1 A_1 \Delta\theta. \end{aligned} \quad (65)$$

The inequality relationships can be inherited from Eq. 64 and Eq. 62. We have

$$d_o^2 \geq d_m^2 \geq d_r^2. \quad (66)$$

2. Case 2: Assume signal ϵ_r under binary hypotheses are determined, in stead of random. The uncertainty in this problem is the additive measurement noise only.

Let C be Zero matrix and let A replace A_1 , from Eq. 59 and Eq. 61, we have

$$\begin{aligned} d_m^2 &= \Delta\Theta^T \Delta\Theta / \sigma_n^2 \\ d_r^2 &= \Delta\Theta^T B_1^T (B_1 B_1^T)^{-1} B_1 \Delta\Theta / \sigma_n^2 \\ \Delta\Theta &= A \Delta\theta. \end{aligned} \quad (67)$$

The inequality relationship can be inherited from Eq. 64, and we have

$$d_m^2 \geq d_r^2. \quad (68)$$

The forms of the deflection coefficients and their inequality relationships for the two special cases can also be derived directly from the corresponding special binary hypotheses.

Discussion

The form of the deflection coefficients for special case 1, and their inequality relationships demonstrate that it is the reduction of the random variable space during the forward and reconstruction procedures that causes the decrease of the detection performance. The detection performance of the optimal detector using the reconstruction data can not be better than that using the measurement data, even without any measurement noise.

The form of the deflection coefficients for special case 2 demonstrates that d_m and d_r are inversely proportional to σ_n^2 , which reflects the direct effect of the measurement noise on the detection performance. In addition, the forms and their inequality relationships also demonstrate that the inadequate rank of the reconstruction matrix B , which is less than the length the measurement data, will reduce the random variable space in dealing with the uncertainty of the measurement noise, and cause the decrease of the detection performance at the reconstruction domain. The effect of the measurement error on the detection performance has been negatively strengthened by the reconstruction procedure. This conclusion agrees well with the simulation result in [16].

The more general form of d_m and d_r in Eq. 59 and Eq. 61 clarify the effects of the combination of the projection and reconstruction procedures as well as the measurement noise. The inequalities in Equations 64 and 62 illustrate

the degradation of the detection performance during the processing procedures. This general conclusion is consistent with our simulation results for the performance of the microwave imaging system.

Clarifying the aspects that causes the degradation of the detection performance could help us design a better system. It suggests that good sampling of the measurement data, which maximizes the random variable space in dealing with the uncertainties (i.e. increase the rank of A), will improve the detection performance. If the measurement error cannot be ignored, the length of the measurement data should be limited (i.e. decrease the difference in rank of B and I_M) to reduce the degradation of post-processing the reconstructed image. It also suggests that making optimal decisions before reconstruction will improve the detection performance.

ADDENDUM to Final Report for Award Number DAMD17-01-1-0513

Principal Investigator: Loren W. Nolte, PhD

Contract Organization: Duke University, Durham, North Carolina 27708-0291

Date: December 17, 2003

1.(a). In the final report the following items should be added to the “**Reportable Outcomes**”.

Liewei Sha, Loren W. Nolte, Zhong Qing Zhang, and Qing Huo Liu, “Incorporating statistical models of tissue permittivity into an optimal signal detection theory framework for the detection of breast cancer at microwave frequencies,” submitted to the IEEE Transactions on Medical Imaging, December, 2003. (Copy of submitted full paper attached. Note: Funding provided by the USAMRMC contract has been acknowledged in this full paper.)

This paper should also be added to the “**Bibliography of all publications**” of the final report as item 5.

(b). Liewei Sha, a PhD student supported in part by this award, expects to receive her PhD in Spring, 2004.

(c). Liewei Sha received an offer of employment from GE Medical Systems in Milwaukee, Wisconsin, during the second year of this award, based on experience supported by this award.

2. Research highlights completed in the second year.

During the second year a more in depth treatment of the signal detection theory approach was developed, a broader class of possible tumor boundaries were considered, lower order approximations were developed for the receiver operating characteristic (ROC) and the probability of correct localization (PCL) to decrease computational complexity, convergence issues of Monte Carlo approaches were quantified, deflection coefficient (delectability index) inequalities were developed to gain insight into tumor detection performance tradeoffs, and the impact of sensor configuration on tumor detection performance was determined using the ROC.

More specific results regarding these topics are contained in the recently submitted full paper given above, referred to in this paragraph as Ref. 5, i.e. Liewei Sha, Loren W. Nolte, Zhong Qing Zhang, and Qing Huo Liu, "Incorporating statistical models of tissue permittivity into an optimal signal detection theory framework for the detection of breast cancer at microwave frequencies," submitted to the IEEE Transactions on Medical Imaging, December, 2003. A more in depth development of the signal detection theory approach and how the measurements and models of breast tissue uncertainty are incorporated is presented in Ref. 5, section II A, B and section III. Incorporating tumors with different possible boundaries was incorporated into the algorithms. In particular, the ROC and the PCL performance measures were compared for tumors with sharp boundaries versus smooth (Ref. 5, section V). Lower order approximations were developed for the Bayesian processors that incorporate the uncertain permittivity for both detection and localization. Quantitative tumor detection and localization performance measures, the ROC and the PCL, were obtained for these lower order approximations, the EPB_UPI and LPB_SEUPI. That work enables one to greatly reduce the computational time for the ROC's and PCL performance curves for both tumor detection and localization (Ref. 5, section IV). Since Monte Carlo integration is necessary in both the Bayesian algorithms as well as in the lower order approximations, the convergence of these algorithms was investigated in order that no more iterations than are necessary are used to get good approximate results of tumor detection performance (Ref. 5, section V). Since most of the quantitative detection performance results are obtained using Monte Carlo methods, deflection coefficient (delectability index) inequalities were developed to gain analytical insight into tumor detection performance tradeoffs (Ref. 5, Appendix). The impact of the sensor array configuration on tumor detection performance as a function of relative location of a tumor to the array sensors was quantified (Ref 5, section F).

3. Please add the following references to the final report. (A more comprehensive list of references is contained in Reference 5 of the modified final report "Bibliography of all publications")

References (add)

W. T. Joines, Y Zhang, C Li, and R. I. Jirtle, "The measured electrical properties of normal and malignant human tissues from 50 to 900 MHz, Med. Phys. J., Vol. 21, No. 4, 547-550, April 1994.

D. J. Jaliha and L. W. Nolte, "Signal detection theory and reconstruction algorithms - performance for images in noise", IEEE Transactions on Biomedical Engineering, vol. 41, No. 5, pp. 501-504, May, 1994.

J. A. Shorey and L. W. Nolte, "Wideband optimal a posteriori probability source localization in an uncertain shallow ocean environment", Journal of the Acoustical Society of America, Vol. 103, No.1, pp. 355-361, January, 1998.

Rasimas, Tantum, and Nolte, "Bayesian signal detection for multiple aspect angles with an uncertain look angle, Proc.of SPIE: Detection and Remediation Technologies for Mines and Minelike Targets, Orlando, FL, April 1999.

A. M. Richardson and L. W. Nolte, "A posteriori probability source localization in an uncertain sound speed, deep ocean environment", Journal of the Acoustical Society of America, Vol. 89, No. 5, pp. 2280-2284, May, 1991.

4. Note: Although the first annual report period covered the period August 1, 2001 – July 31, 2002, the following item presented during the second year, August 1, 2002 – August 30, 2003 of the no-cost project extension was listed under the reportable outcomes, references and appendices sections in the first annual report.

Liewei Sha and Loren W. Nolte, "Computer-aided algorithms for breast tumor diagnosis using microwave diffraction measurements", Era of Hope 2002 Department of Defense Breast Cancer Research Meeting, Orlando, Florida, September 25-28, 2002."

In the first annual report, this should have been listed as "a poster to be presented" and the "Copy of the paper by Liewei Sha and Loren Nolte", item 3 in the appendix of the first year report should have read "Copy of the poster ...".